
Non-equilibrium dynamics and feedback control of strongly confined colloidal suspensions in a planar shear flow

vorgelegt von

Master of Science
Tarlan Azad Vezirov
geb. in Baku

Von der Fakultät II - Mathematik und Naturwissenschaften
der Technischen Universität Berlin
zur Erlangung des akademischen Grades
Doktor der Naturwissenschaften
Dr. rer. nat.

genehmigte Dissertation

Promotionsausschuss:

Vorsitzender: Prof. Dr. Michael Lehmann

1. Gutachterin: Prof. Dr. Sabine H. L. Klapp

2. Gutachter: PD Dr. Michael A. Zaks

Tag der wissenschaftlichen Aussprache: 13.07.2015

Berlin 2015

Declaration of Authorship

I, Tarlan Azad VEZIROV, declare that this thesis titled, 'Non-equilibrium dynamics and feedback control of strongly confined colloidal suspensions in a planar shear flow' and the work presented in it are my own. I confirm that:

- This work was done wholly or mainly while in candidature for a research degree at this University.
- Where any part of this thesis has previously been submitted for a degree or any other qualification at this University or any other institution, this has been clearly stated.
- Where I have consulted the published work of others, this is always clearly attributed.
- Where I have quoted from the work of others, the source is always given. With the exception of such quotations, this thesis is entirely my own work.
- I have acknowledged all main sources of help.
- Where the thesis is based on work done by myself jointly with others, I have made clear exactly what was done by others and what I have contributed myself.

Signed:

Date:

Publications

Parts of the results presented in this thesis have been published in the following peer-reviewed journals:

Tarlan A. Vezirov and Sabine H. L. Klapp

Nonequilibrium dynamics of a confined colloidal bilayer in a planar shear flow

Phys. Rev. E **88** 052307 (2013)

Tarlan A. Vezirov, Sascha Gerloff and Sabine H. L. Klapp

Manipulating shear-induced non-equilibrium transitions in colloidal films by feedback control

Soft Matter **11** 406 (2015)

Tarlan A. Vezirov, Sascha Gerloff and Sabine H. L. Klapp

Shear induced laning in confined colloidal trilayer

in preparation (2015)

Zusammenfassung

Im Rahmen der vorgelegten Arbeit untersuchen wir den Einfluss einer externen treibenden Kraft, der Scherung $\dot{\gamma}$, auf das Verhalten geladener (mit einer Valenz von $Z \approx 35$) kolloidaler Teilchen in einer Schlitzpore. Die Präsenz der begrenzenden Wände führt zu einem Symmetriebruch, was wiederum eine Schichtenbildung parallel zu den Porenwänden zur Folge hat. Um das untersuchte System zu vereinfachen werden die Gegenionen, welche von der Oberfläche der Kolloide dissoziieren, als eine Art abschirmende Wolke behandelt. Diese ionisierte Hülle ermöglicht es, die explizite Coulombwechselwirkung zwischen den Kolloiden durch eine effektive Abschirmung des elektrostatischen Potentials zu ersetzen, welche durch sogenannte Derjaguin-Landau-Verwey-Overbeek-Theorie beschrieben wird. Bei der Beschreibung des Verhaltens von Kolloiden verwenden wir die Methode der überdämpften Brownischen Dynamik.

Zunächst wird ein Zweischichtensystem betrachtet. Dabei werden scherinduzierte Übergänge zwischen der quadratischen, geschmolzenen und hexagonalen Ordnung innerhalb der Schichten beobachtet, sowie die Dynamik dieser Zustände untersucht. Hierbei präsentieren wir unter anderem ein semi-analytisches Modell, welches zur Beschreibung des Diffusionsverhaltens im geschmolzenen Zustand verwendet werden kann. Im hexagonalen Zustand liegt unser Fokus auf den räumlich-zeitlichen Oszillationen der Teilchen, der sogenannten Zig-Zag-Bewegung.

Um die für das Zweischichtensystem gemachten Beobachtungen zu verallgemeinern wird die Breite der Schlitzpore erhöht. Dies führt zu einer Erhöhung der Schichtanzahl von zwei auf drei. Bei den Untersuchungen des Dreischichtensystems können wir nicht nur die Ergebnisse des Zweischichtensystems bestätigen, sondern auch einen neuen Zustand erkennen. In diesem Zustand spaltet sich die mittlere Schicht in zwei, in Bahnen ("lanes") geordnete, Subschichten auf, was wiederum die Dynamik des Systems maßgeblich beeinflusst.

Im dritten Abschnitt werden wir feststellen, dass die scherinduzierten Strukturübergänge ein nichtmonotones Verhalten des Scherstress auslösen können. Dies wird genutzt, um die vormals statische Scherrate $\dot{\gamma}$, durch die Einführung einer Feedback-Kontrolle zu dynamisieren und den stationären Zustand des Systems auszuwählen. Wir können auch zeigen, dass der Endzustand des Systems nicht nur von der Anfangskonfiguration der Kolloide und der anfänglichen Scherrate, sondern auch von dem Verhältnis zwischen der Zeitskala der Feedback-Kontrolle und der intrinsischen Zeitskala abhängt.

Abstract

In this study, we investigate the behavior of a strongly confined colloidal suspension under the influence of an external driving force, the shear $\dot{\gamma}$. The colloids are assumed to be charged with a valency of $Z \approx 35$. The presence of the limiting walls leads to a symmetry breaking, which in turn induces a layer formation parallel to the walls. In order to simplify the system description the counter-ions which dissociate from the surface of colloids, are treated as a kind of shielding cloud. These ionized shell makes it possible to replace the explicit Coulomb interaction between the colloids through an effective level via Derjaguin-Landau-Verwey-Overbeek theory. In describing the behavior of colloids, we use the method of overdamped Brownian dynamics.

First, we consider a two-layer system. We observe shear induced order transitions between the square, molten and hexagonal states as well as study their dynamical properties. Furthermore, we present a semi-analytical model which can be used to describe the diffusion behavior in the molten state. In hexagonal state, we focus on the spatio-temporal oscillations of the particles, the so-called zig-zag motion.

In order to generalize the observations made for the bilayer system the width between the confining walls is increased. This leads to an increase of the layer number from two to three. Investigating the trilayer system, we can not only confirm the results observed in the bilayer system, but also recognize a new state. In this state, the middle layer splits into two laned sublayers. This separation in sublayers significantly affects the dynamics of the system.

In the third section, we note that the shear-induced structural transitions lead to non-monotonic behavior of the shear stress. The introduction of a feedback control by which the formerly static shear rate $\dot{\gamma}$ is transformed into dynamical variable enables to select stationary state of the system. We can also show that the steady state of the system depends not only on the initial configuration and the initial shear rate, but also on the relation between the time scale of the feedback control and the intrinsic time scale.

Contents

Declaration of Authorship	II
Publications	III
Zusammenfassung	IV
Abstract	V
Contents	VI
List of Figures	XI
List of Tables	XV
Abbreviations	XVII
Symbols	XIX
1 Introduction	1
1.1 Introduction to colloidal science	1
1.2 Confinement between two parallel plates	2
1.3 Shear driven colloidal suspensions	4
1.4 The foundation on which we build	8
1.5 An overview of the thesis structure	10
2 Theoretical principles	13
2.1 Introduction of the confining walls	13
2.2 Charged particles at surfaces	14
2.2.1 Charge screening at surfaces	15
2.2.2 Derjaguin-Landau-Verwey-Overbeek theory	18
2.3 Soft-sphere potential	29
2.4 Structural observables	29
2.4.1 Density	30
2.4.2 Radial pair distribution function	30
2.4.3 Bond angle order parameter	32
2.4.4 Pressure tensor	33

2.5	Shear flow	38
2.6	Brownian motion	40
3	Simulation methods	43
3.1	Reduced units	43
3.2	Truncated and shifted potential	44
3.3	Periodic boundary conditions	45
3.4	Cell lists algorithm	48
4	Model	51
4.1	General setup	51
4.2	Truncation of interparticle potentials	53
4.3	Model parameters	54
5	Confined colloidal bilayer in a planar shear flow	57
5.1	Shear-induced structural changes	58
5.2	Translational dynamics	61
5.3	Diffusion in the shear-molten state	64
5.4	Zig-zag motion at high shear rates	66
6	Shear induced laning in confined colloidal trilayer	73
6.1	Density distribution and translational order in a shear driven trilayer system	74
6.2	Semi-laning	76
6.3	Shear induced dynamics	79
7	Feedback control of non-equilibrium transitions	85
7.1	Rheology of shear-induced transitions	86
7.2	Stress tensor of shear-driven colloidal trilayer	88
7.3	Intrinsic time scales	91
7.4	Impact of feedback control	94
7.5	Transition line	99
7.6	Strain-stress relation under constant shear rate	101
8	Conclusion and Outlook	103
8.1	Conclusion	103
8.2	Outlook	106
A	Theoretical details	111
A.1	Calculation of the bond angle order parameter	111
A.2	Mechanical stability analysis	112
A.3	Stability of the feedback controlled system	113
B	Preliminary results	115

B.1 Time-delayed feedback control	115
B.2 Oscillatory shear	116
B.3 Density excitations	117
Bibliography	121
Danksagung	XXI

List of Figures

1.1	Sketch of two possible experimental assemblies for investigations on shear driven systems [1].	4
1.2	Transmission electron microscopy images of colloidal particles: a) SM 30 ($\tilde{\sigma} = 9 \pm 2$ nm), b) HS 40 ($\tilde{\sigma} = 16 \pm 2$ nm), c) TMA 34 ($\tilde{\sigma} = 25 \pm 2$ nm) [2].	8
1.3	Example of position correlation diagrams obtained from colloidal suspension (PS301) a) bcc structure at rest, b) under shear $\dot{\gamma} = 0.35$ Hz, c) under shear $\dot{\gamma} = 7.90$ Hz, d) Example image of a nucleation of the square phase of PS301 within hexagonal lattice after cessation of shear. [3]	10
2.1	Helmholtz and Gouy-Chapman model of the electric double layer.	16
2.2	Schematic representation of a shear cell. Two parallel walls are separated by a sample of thickness L_z . The examples visualize setups without shear (a) as well as with shear induced by the motion of one (b) and two layers (c).	37
3.1	Types of periodic boundary conditions.	46
3.2	The cell list: the simulation cell is divided into cells of size $r_c \times r_c$. Each particle can interact only with particles in the same cell or neighboring cells.	48
4.1	Definition of the coordinate system and schematic illustration of the shear cell. The dashed line indicates the zero-velocity plane, which is positioned at $z=0$	53
4.2	Sketch of equilibrium configurations for the bi- and trilayer film.	55
5.1	Simulation snapshots at $\rho^*=0.85$ and $L_z=2.2\tilde{\sigma}$ for different shear rates. The yellow (red) circles represent particles of the upper (lower) layer.	58
5.2	Density profiles in the shear gradient (and confinement) direction for different shear rates.	59
5.3	In-plane order parameter for square (Ψ_4) and hexagonal (Ψ_6) symmetry as a function of the shear rate $\dot{\gamma}$	60
5.4	Intralayer distribution function $g(r)$ at different shear rates.	61
5.5	The position of the center of mass (PCM) in flow direction (a) and the velocity profile of the system (b) at different shear rates.	62

5.6	Effective shear rate (as determined from the velocity profile) as a function of the shear rate $\dot{\gamma}$	63
5.7	The mean squared displacements within the layer in flow (MSD_x) and vorticity (MSD_y) directions at different shear rates.	67
5.8	Fit of the mean squared displacements of one sheared particle in harmonic potential with the simulated system at $\dot{\gamma}\tilde{\tau} = 230$ in flow direction (a) and vorticity direction (b). From the fit resulting harmonic potential was compared with the density profile in (c). The parameters used in the fit are $D_x^* = 3.37$, $D_y^* = 0.0024$, $D_z^* = 3.16 \times 10^{-5}$ and $\omega^* = 6521$	67
5.9	Time evolution of the number density $N(y, t)$ at $\dot{\gamma}\tilde{\tau} = 500$	68
5.10	Rescaled oscillation frequencies of the zig-zag motion at different shear rates.	69
5.11	The distinct part of the van Hove function in vorticity direction at $\dot{\gamma}\tilde{\tau} = 400$	71
5.12	Rescaled oscillation of the structure factor in the vorticity direction.	71
6.1	Density profiles along the shear gradient (and confinement) direction for different shear rates.	74
6.2	In-plane order parameter for square (Ψ_4) and hexagonal (Ψ_6) symmetry as a function of the shear rate $\dot{\gamma}$. The order parameter was calculated separately for the middle and the side layer.	74
6.3	Simulation snapshot of the xy -plane at $\rho^* = 0.85$ and $L_z = 3.2\tilde{\sigma}$ for different shear rates. The green (yellow, red) circles represent particles of the upper (middle, lower) layer.	76
6.4	Simulation snapshot of the middle layer calculated along the xy -plane at $\rho^* = 0.85$ and $L_z = 3.2\tilde{\sigma}$ for different shear rates. The yellow (red) circles represent particles of the upper (lower) sublayer separated at $\langle z \rangle = 0$	77
6.5	Density profiles of the sublayers of the middle layer in the vorticity direction. The sublayers were separated at $\langle z \rangle = 0$	78
6.6	Sketch of the definition of the laning order parameter ϕ_i	78
6.7	Laning order parameter calculated within the middle layer as a function of the shear rate $\dot{\gamma}$	79
6.8	Velocity of the position of the center of mass of all three layers as well as the sublayers of the middle layer.	79
6.9	Trajectories of arbitrarily chosen particles at different shear rates.	81
6.10	Mean squared displacement relative to the center of mass of the particles in the middle layer at different shear rates.	81
6.11	MSD_x of one single system at $\dot{\gamma}\tilde{\tau} = 28$. For the calculation only the particles from the middle layer were considered.	83
6.12	Particle transition from the middle layer to the side layers as a function of time. The number of particles was related to its initial value in the middle layer. For the calculation only the particles were considered which stayed in the middle layer during the time period $[0, t)$	83

7.1	Steady state shear stress and shear viscosity (insets) for bi- and trilayer systems as function of the applied shear rate. Regions indicated as I, II, III are discussed in the main text.	87
7.2	Components of the stress tensor as a function of the applied shear rate.	90
7.3	Sketch of the two possible regimes by which the pitchfork-like behavior of σ_{xy} in Fig. (7.2) can be explained.	91
7.4	Response of $\sigma_{xz}(t)$ to a sudden switch-on (at time τ_{on}) of shear with different rates $\dot{\gamma}_{\text{new}}\tilde{\tau}$. The simulations were started from the equilibrium (square) state in a bilayer system. The inset shows the fit of the relaxation times τ_1 according to Eq. (7.4).	92
7.5	Response of $\sigma_{xz}(t)$ to a sudden change (at time τ_{on}) of shear. The new shear rates $\dot{\gamma}_{\text{new}}\tilde{\tau}$ result in a relaxation in the square state. The simulations were started from the hexagonal steady state at $\dot{\gamma}\tilde{\tau} = 400$ in a bilayer system. The inset shows the fit of the relaxation times τ_3 according to Eq. (7.4).	93
7.6	Time dependence of the instantaneous shear rate and shear stress for a bilayer- (a,b) and a trilayer system (c,d) in presence of feedback control within region I. The imposed stress was set to $\sigma_0\tilde{\sigma}\tilde{\tau}^2 = 6(2)$ for the bilayer (trilayer) system. Various values of $\tau_c/\tilde{\tau}$ are considered. The initial configuration is hexagonal.	95
7.7	Same as Fig. (7.6), but for $\sigma_0\tilde{\sigma}\tilde{\tau}^2 = 8(2.7)$ for the bilayer (trilayer) system (region II). The initial configuration is square.	96
7.8	State diagram indicating long-time lattice structures. All simulations were started from a square ordered bilayer and the imposed shear stress was set to $\sigma_0\tilde{\sigma}\tilde{\tau}^2 = 8$. The line shows the result from Eq. (7.8).	97
7.9	State diagram indicating long-time lattice structures. All simulations were started from the hexagonal ordered bilayer and the imposed shear stress was set to $\sigma_0\tilde{\sigma}\tilde{\tau}^2 = 8$	97
7.10	Same as Fig. (7.7), but for $\sigma_0\tilde{\sigma}\tilde{\tau}^2 = 16(5)$ for the bilayer (trilayer) system (region III). The initial configuration is square.	98
7.11	Stress-strain relations for bi- and trilayer.	101
8.1	Sketch of an experimental setup for an application of the time-delayed feedback control.	106
B.1	Fluctuations of the shear stress (a) and the shear rate (b) for the time-delay feedback-controlled colloidal bilayer at $\sigma_0^* = 8$, $\eta_0^* = 0.086$, $\tau_c^* = 0.01$ and $\tau_D^* = 500$. The simulation was started from a square-ordered configuration.	116
B.2	Lissajous figures illustrating the non-linear character of the stress response at large amplitude oscillatory shear.	117
B.3	Sketch of the strongly confined mixture. The model system was used by Sascha Gerloff to investigate the appearance of density excitations. The sketch was provided by Sascha Gerloff.	118

B.4 Velocity of kinks and antikinks compared to the velocity of the center of mass of the reference (upper) layer. The model system was used by Sascha Gerloff to investigate the appearance of density excitations. The graphic was provided by Sascha Gerloff. 119

List of Tables

1.1	Different types of colloidal dispersions with examples [4].	2
-----	---	---

Abbreviations

bcc	body centered cubic
fcc	face centered cubic
MD	Molecular Dynamics
BD	Brownian Dynamics
oBD	overdamped Brownian Dynamics
MC	Monte Carlo
MSD	Mean Squared Displacement

Symbols

L	width of the simulation box
L_z	distance between confining walls
N	particle number
r_c	cutoff radius
D_0	short time diffusion coefficient
δt	time step
ρ	number density
$\tilde{\sigma}$	particle diameter, unit of length
$\tilde{\epsilon}$	unit of energy
$\tilde{\tau}$	Brownian time, unit of time
$\dot{\gamma}$	shear rate
τ_c	control time scale
σ_{xz}	shear stress
σ_0	imposed shear stress
η	viscosity
κ	screening length

Chapter 1

Introduction

1.1 Introduction to colloidal science

Most of us are not aware of just how much our daily lives are impacted by colloids. Different kinds of colloidal particles are not solely versatile ingredients of our environment (e.g., porous rocks, clays, mists, smoke and dust), but even our bodies offer a great diversity of colloids, such as blood and bone components. Moreover, milk, the first meal everyone consumes is nothing else than a colloidal suspension. In addition to the existence of a huge amount of *natural* colloids, the creation of new and more demanding *artificial* colloidal materials and their studies is an ongoing investigation process [5]. The reward for this effort is the discovery of new substances and optimized processing which for their part lead to an improvement in various technical, chemical as well as medical and biological applications [6–14]. In this context, feedback-control techniques of non-equilibrium systems are naturally of especial interest and will be the main topic in the current thesis.

Generally a colloidal dispersion can be considered as a heterogeneous, in most cases two-component system, in which the size of the particles of at least one component ranges from molecular size ($\approx 10nm$) to the size of small sand grains ($\approx 1\mu m$) [4]. The interplay of different materials and phases leads to emergence of colloidal substances with a wide range of completely different properties. An

Disperse phase	Dispersion medium	Name	Examples
Liquid	Gas	Liquid aerosol	Fog, Hair sprays, Clouds
Solid	Gas	Solid aerosol	Smoke
Gas	Liquid	Foam	Shaving cream, Whipped cream
Liquid	Liquid	Emulsion	Milk, Mayonnaise, Hand lotion
Solid	Liquid	Sol, <u>Colloidal suspension</u>	Paint, Toothpaste, Blood
Gas	Solid	Solid foam	Styrofoam, Pumice
Liquid	Solid	Solid emulsion	Ice cream, Gelatin
Solid	Solid	Solid suspension	Opal, Pearl, Pigmented plastic

Table 1.1: Different types of colloidal dispersions with examples [4].

overview of phase combinations and examples of resulting materials are presented in Tab. (1.1). The lower limit of the colloidal size, which is $\approx 10nm$, ensures that the mass of colloids is much larger than that of the surrounding solvent particles. From this it follows that at time and length scales of colloidal particles the solvent and consequently all its properties (e.g., viscosity, dielectric constant, refractive index etc.) can be considered as continuum. The definition of the lower limit has also one further implication. It means that due to the relatively large size of colloids quantum effects are of secondary importance and can be neglected. Therefore, for the description of colloidal systems the principles of classical statistical mechanics become sufficient [15, 16].

One of the main research topics in the framework of colloidal suspensions is structure formation which for example can be significantly affected by the introduction of confinement or other external forces.

1.2 Confinement between two parallel plates

The introduction of confining walls occupies a special niche among the possibilities to influence the structure of colloidal suspensions by an external field. As the physics of confined matter is of great importance for lubrication, adhesion and

nanotechnology the use of complex biological (e.g., cell walls or veins) as well as technological systems (e.g., microfluidic devices [17] and walls in porous materials [18]) requires a deep understanding of underlying fundamental processes.

It is already well known that the introduction of confinement, which can be experimentally realized in setups such as, e.g., the colloidal-probe atomic-force microscope (CP-AFM) [19] or the surface force apparatus (SFA) [20], leads to a symmetry-breaking within the system. The result of this symmetry-breaking is that the homogeneous (bulk) system transforms into an inhomogeneous one [21]. Such an inhomogeneous behavior usually manifests itself by an oscillating local density along the confinement axis and can be interpreted as layering of e.g., colloidal particles [22, 23] or liquid crystals [24] oriented parallel to confining walls. An important consequence arising from this effect, is the oscillatory, exponentially decaying structural (solvation) force [25]. Moreover, depending on the interplay between the particle size and the wall distance the system can become commensurable or incommensurable which also strongly affects the final state. In the first studies addressing the influence of the slit-pore geometry on the enclosed sample it was observed that the number of colloidal layers within the sample as well as their translational order is strongly connected to the distance between the confining walls [26–28]. As a matter of fact, in the latter studies it could be shown that an increase of the distance between confining walls leads to a sequence of states given by

$$\text{fluid} \rightarrow 1\triangle \rightarrow 2\square \rightarrow 2\triangle \rightarrow 3\square \rightarrow \dots . \quad (1.1)$$

In Eq. (1.1) the symbols $n\triangle$ and $n\square$ denote n -layer crystals with hexagonal and square structure, respectively. Further theoretical and experimental studies have enhanced the understanding of such effects as layering and ordering and culminated in the discovery of novel states e.g., buckled, rhombic or prismatic phases [29–31].

Besides translational order of sphere-shaped colloids, confinement can also affect the orientational order in anisotropic systems [23, 32, 33].

In addition to equilibrium systems there is a strong interest in the behavior of

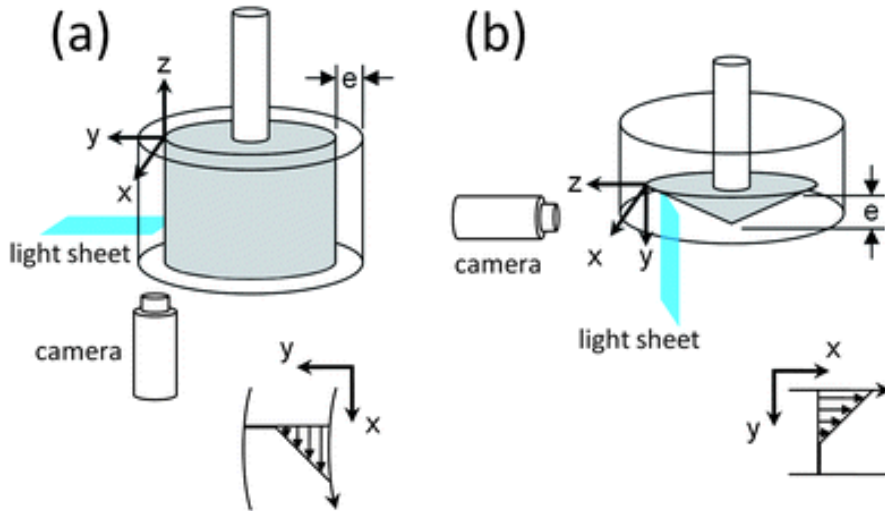


Figure 1.1: Sketch of two possible experimental assemblies for investigations on shear driven systems [1].

confined samples driven by external forces such as shear [34–36]. This interest can be explained by the fact that the double symmetry-breaking induced by confinement and external force in connection with the non-equilibrium state of the whole system significantly increases the complexity and diversity of the considered system.

1.3 Shear driven colloidal suspensions

Among a broad variety of studies concerning the influence of driving mechanisms in soft matter, the present thesis is devoted to the impact of shear. The term *shear* implies the existence of a velocity gradient within the system. And although in general the functional dependency of this gradient can vary, usually linear velocity profile, the so-called *planar Couette flow*, is meant.

Shear driven colloidal systems have a variety of applications in lubrication science [37, 38], in medical contexts (i.e., synovial fluid lubrication, tissue shearing) [39–43] but also in macroscopic contexts such as traffic jams [44, 45]. Another important reason which makes the studies on sheared system so popular can be explained by the fact that such systems can display rich non-linear behavior involving transitions between different dynamical states [46, 47], spontaneous spatial

symmetry-breaking [48], shear-banding [49–52] (for recent reviews, see Refs. [53–57]), rheochaos [58–60] and heterogeneous local dynamics [61, 62]. These intriguing phenomena strongly affect the rheological properties of the system. Understanding shear-induced effects in, e.g., complex surfactant solutions [63] or liquid crystals [46, 47], colloids [64–66], soft glasses [61, 62, 67], and active fluids [68], is thus a current topic of high interest which connects non-equilibrium physics with soft material science. A quantity of particular importance is the flow (or constitutive) curve [52, 57], that is, the shear stress σ [see Sec. 2.4.4] as function of the shear rate $\dot{\gamma}$ [see Sec. 2.5], both of which can serve as experimental control parameters. In many examples, the curve $\sigma(\dot{\gamma})$ behaves not only non-linear (indicating shear-thinning [69, 70], shear-thickening [70, 71], sometimes connected irregular (chaotic) rheological response [60, 72]), but becomes also multivalued, i.e. different shear rates lead to the same stress. In complex fluids of wormlike micelles, this multivalued property is in fact a universal indicator of a shear-banding instability, specifically, gradient banding, where the (formerly homogeneous) system separates in gradient direction into coexisting bands characterized by a smaller and a larger local shear rate [57] (note that this is different from the more exotic vorticity banding, i.e., the formation of bands along the vorticity direction as discussed e.g., in Refs. [56, 57, 73]). In soft (colloidal) glasses, multivalued functions $\sigma(\dot{\gamma})$ occur as transient phenomena after a sudden switch-on of shear stress (Bauschinger effect) [74], or in the vicinity of the so-called yield stress [75]; in these systems one observes strong dynamical heterogeneities [62]. A further intriguing feature is that close to such non-monotonicities, the system's behavior strongly depends on whether one uses the shear stress or the shear rate as a control parameter [59, 76]. In fact, both choices are common in rheological experiments [67, 77, 78].

The importance of studies aiming at the understanding of mechanisms which can be applied to control the (order) configuration and consequently also the rheology of the system cannot be overestimated. Insights gained in such investigations are of great importance not only for fundamental research but also for the production processes which for instance lead to efficiency improvement of nanostructured

photonic materials [79–81] or increase the quality of pharmaceutical products [82] and treatment methods [83–85].

In experiments moving one surface with respect to the other one it is possible to induce a linear shear profile in the intermediate sample [see Fig. (1.1)]. Such experiments are able to provide diverse information not only about the real (\mathbf{r} -) but also the reciprocal (\mathbf{k} -) space of the system. Performing real space experiments with light microscopy it is possible to track every single particle within the considered sample. This enables the measurement of dynamical (e.g., trajectories of the particles [86]) as well as static (e.g., pair distribution function $g(\mathbf{r})$ [87]) system characteristics. In \mathbf{k} -space studies one is mainly interested in the sample structure. Performing scattering experiments this property can be evaluated via the structure factor $S(\mathbf{q})$, which is related to the Fourier transform of the pair distribution function $g(\mathbf{r})$ [see Sec. 2.4.2].

A big advantage of experiments with colloidal suspensions [88–90] compared to that of molecular studies [91] is that dealing with colloids it is possible to perform real and reciprocal studies with the same sample which allows a more versatile understanding of physical processes taking place. Furthermore, driven colloidal suspensions can generally serve as well controllable and (compared to atomic systems) accessible model systems to study the behavior of condensed matter in restricted geometries. Two recent examples in the context of transport phenomena are the observation of excitons (kinks and antikinks) in driven colloidal monolayers [92], and the crossover from single-file to conventional Fick diffusion in colloidal nanochannels [93].

The first attempts to investigate the shear influence in colloidal suspensions numerically were based on the Molecular dynamics (MD) simulations [94, 95]. However, it very soon became apparent, that the usage of usual velocity profile biased thermostats (e.g., thermostats based on the Gauss’s principle of least constraint [96–98]) in shear driven systems has to be seen highly critically. The reason for unsuitability of the temperature control methods widely used in equilibrium MD in presence of shear, is that within the shear driven suspensions the actual streaming velocity tends to deviate from the applied (assumed) one. This discrepancy

becomes more significant with increasing shear rate [99]. The deviation between the actual and the assumed streaming velocity is then interpreted as an elevated temperature. As a consequence aiming to reconcile both shear rates and streaming velocities the profile biased thermostat cools the sample down [99]. The result of this cooling is the emergence of numerical artifacts e.g., string phase [94, 100–102]. A novel access to the definition of temperature proposed by Rugh [103] enabled the development of velocity profile unbiased thermostats [102, 104–107] which aimed at overcoming the latter problem. The idea behind these so-called configurational thermostats is that the temperature calculation is carried out via the function based on the configuration of the particles rather than the streaming velocity within the system. An additional weakness of MD simulations in non-equilibrium systems is the fact that the interaction with the surrounding solvent is completely neglected.

Alternatively a calculation of shear driven colloidal suspensions can be carried out via the Brownian dynamics (BD) simulation [34, 35, 64, 108, 109]. There are two major reasons making BD more appropriate for non-equilibrium computations than MD. First, for the temperature control no assumptions about the streaming velocity are needed. Second, in the BD framework the surrounding solvent is implicitly modeled. Note that this method was also used in the present thesis and therefore will be discussed in more detail in Sec. 2.6.

Nevertheless, at large streaming velocities it is necessary to keep in mind that the hydrodynamical effects can become more significant. In such situations the solvent must be considered explicitly. This can be done by coarse-graining techniques such as lattice Boltzmann methods [110–112], dissipative particle dynamics [113] or Stokesian dynamics simulations [114].

From the theoretical side, many properties of colloids in and out of equilibrium can be described by established *effective* interaction models. This enables one to employ a broad variety of semi-analytical methods such as density functional theory [115] and its dynamical extensions [116], mode-coupling theory (MCT) [108, 117–122], as well as phenomenological models which are based on the Landau description of equilibrium phase transitions [123].

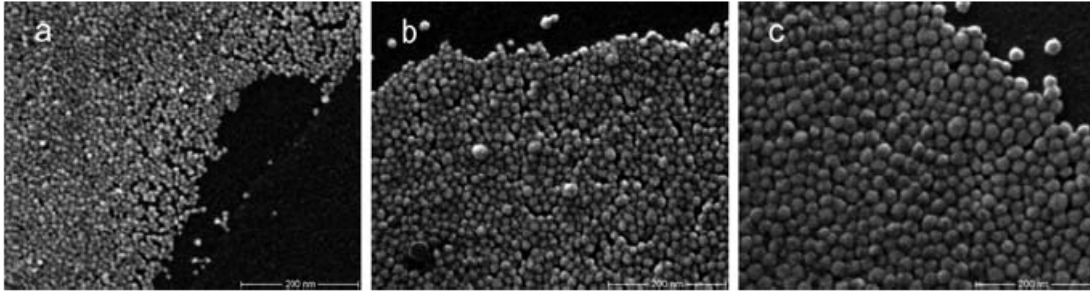


Figure 1.2: Transmission electron microscopy images of colloidal particles: a) SM 30 ($\tilde{\sigma} = 9 \pm 2$ nm), b) HS 40 ($\tilde{\sigma} = 16 \pm 2$ nm), c) TMA 34 ($\tilde{\sigma} = 25 \pm 2$ nm) [2].

1.4 The foundation on which we build

The major basis for the model system used in this thesis can be attributed to investigations performed on strongly confined systems of silica colloids [see Fig. (1.2)] [2, 124–127]. The reason for the choice of this model is that comparison between the findings gained from Monte-Carlo (MC) simulations with those of experimental studies have shown that the numerical model used in Refs. [2, 125, 127] yields results which are in a very good agreement with observations made in experimental measurements. What makes the proposed model even more attractive is the fact that in the framework of numerical simulations carried out in the latter studies the interactions between different particle types (in particular macroions surrounded by counterions, salt ions and solvent molecules) were coarse-grained such that only the repulsive part of the Derjaguin-Landau-Verwey-Overbeek (DLVO) potential [see Sec. 2.2.2] as well as the steric repulsion [see Sec. 2.3] have been proved to be sufficient. In fact the substitution of the long-range Coulomb potential by the DLVO potential is justified since the former one is screened by counterions and salt ions, such that the Coulomb interaction exponentially decreases. Among a large number of questions which were addressed in Refs. [2, 124–127] the most important point for our purpose is given in Ref. [124]. It could be shown that a change of the wall distance in the considered slit-pore geometry results in transitions between hexagonal and square order. Although this observation is not the key result of the latter study, as similar behavior was already observed in various other confined systems [26–28], this particular result is of great importance for

our purpose. The reason for its importance is the fact that the agreement between numerical and experimental results in combination with a well defined set of parameters can be directly related to a real colloidal suspension and provides a realistic initial configuration for our simulations. All of this gives us the hope that the observations reported in this thesis can be straightforwardly proven in experimental studies.

Addressing the investigations of shear induced phenomena we use as a starting point findings gained from experiments by Stipp *et al.* [3]. Carrying out their experiments with a confined system consisting of charged, spherical colloidal particles in low salt or deionized water solution, the system parameters were chosen such that the initial configuration of colloids is body centered cubic (bcc) with 110-plane being oriented parallel to the confining walls [see Fig. (1.3a)]. As the shear was applied, initially pinned layers started to move with respect to each other. Moreover, the layers changed their order by rearrangement from square into the hexagonal configuration [see Fig. (1.3b-c)]. Stipp *et al.* observed the emergence of the so-called zig-zag motion, which was also reported by other groups [65, 128]. It could be shown that this kind of motion measured at relatively low shear rates [see Fig. (1.3b)] continuously vanished with increasing shear [see Fig. (1.3c)]. The transition from the square into the hexagonal state revealed to be kinetically stabilized against relaxation into the equilibrium bcc structure. Therefore, at the cessation of shear hexagonal ordered layers recrystallized into the square configuration. As shown in Fig. (1.3d) this transition was not instantaneous but occurred after the passing of the so-called molten state. In numerical studies performed by Messina *et al.* [34] the verification for the shear induced order transitions as well as the existence of the intermediate, molten, state was given. Furthermore, it was also shown that the molten phase can be observed not only by the transition from the hexagonal order into the square state but also vice versa.

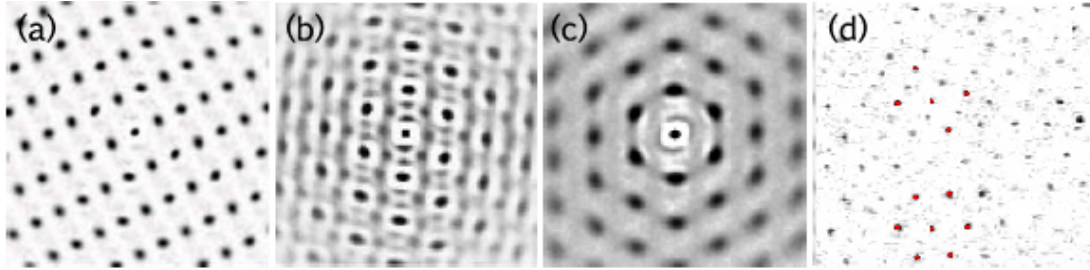


Figure 1.3: Example of position correlation diagrams obtained from colloidal suspension (PS301) a) bcc structure at rest, b) under shear $\dot{\gamma} = 0.35$ Hz, c) under shear $\dot{\gamma} = 7.90$ Hz, d) Example image of a nucleation of the square phase of PS301 within hexagonal lattice after cessation of shear. [3]

1.5 An overview of the thesis structure

This thesis is organized as follows. In Chap. 2, the most important theoretical background is discussed. Therefore, starting with a brief overview of statistical ensembles used in this thesis we subsequently commit ourselves to the introduction of interactions taken into account in this study. First, we motivate the description of the confining walls which are of great importance for our work. Second, the detailed derivation of the DLVO theory is presented. Since in the following investigations a DLVO potential is supplemented by the (short-ranged) soft-sphere potential also the justification for the latter interaction is given. Then we introduce frequently used system observables. In the last two sections of the second chapter we take a close look at the definition of the shear rate (our key parameter) as well as the Brownian dynamics method.

The discussion in Chap. 3 is started with the introduction of reduced units and the justification of their usage. In the following section the techniques of truncation (of short-range potentials) is discussed. The truncation and shift of the potentials enables convenient application of periodic boundary conditions as well as acceleration of the simulation by the *Cell lists* algorithm, which were discussed in Sec. 3.3 and Sec. 3.4, respectively.

In Chap. 4 we introduce our model system as well as discuss the techniques parameters used in this study.

In Chap. 5 we start with a discussion of shear-induced structural changes in

strongly confined colloidal bilayer, followed by a numerical analysis of the translational single-particle dynamics. Then a semi-analytical model for the description of the mean square displacement at intermediate shear rates, for the so-called molten state, is suggested. At the end of the chapter we report our findings concerning the development of zig-zag motion in the hexagonal regime.

In Chap. 6 we focus on the identification and the discussion of the semi-laned state that we discovered for the shear driven, confined colloidal trilayer system. In the subsequent parts of the chapter we characterize the dynamical (transport) properties of the system focusing on the semi-laned state.

The main focus of Chap. 7 lies on the rheological properties of the confined bi- and trilayer systems. Therefore, we are mainly interested in the response of shear stress and of the shear viscosity to the applied shear rate. In addition we propose a feedback control scheme by which the translational order of the system can be controlled. Finalizing the chapter we compare the control time scales and intrinsic time scales of the system and suggest a semi-analytical description for the feedback induced order transitions.

The thesis is concluded with a summary of the main aspects of our studies as well as with an outlook concerning proposals for future investigations.

At this point, it should be noted that the results presented in Chap. 6 and Chap. 7 were derived in cooperation with the student assistant Sascha Gerloff who was working with me in the same project funded by SFB910. He was mainly responsible for the simulations. For this purpose, he used the source code previously developed and already successfully used [see Chap. 5]. For my part I gave and explained him the source code which I developed, supervised his work, performed selective simulations in order to check the correctness of his results and to clarify the details and uncertainties. Moreover, I (in close contact with Sascha Gerloff) selected the data and used them for final interpretation and explanation.

Chapter 2

Theoretical principles

2.1 Introduction of the confining walls

One of the focal points of this study is to understand the behaviour of shear driven colloidal suspensions under conditions of strong symmetry-breaking due to confinement. The simplest example of a confining wall is given by uncharged and unstructured surface, which can be mimicked by the short range soft-wall interaction.

To derive the corresponding potential one usually assumes, that the confining walls are composed of particles interacting via the Lennard-Jones potential which reads

$$u_{LJ}(r) = 4\tilde{\epsilon} \left(\left[\frac{\tilde{\sigma}}{r_{ij}} \right]^{12} - \left[\frac{\tilde{\sigma}}{r_{ij}} \right]^6 \right). \quad (2.1)$$

In Eq. (2.1) $\tilde{\sigma}$ is the particle diameter, $r_{ij} = |\mathbf{r}_i - \mathbf{r}_j|$ with $\mathbf{r} = (x, y, z)^T$ the interparticle distance and $\tilde{\epsilon}$ the coupling parameter with units of energy. Since the confining walls are purely repulsive the attractive part of Eq. (2.1) can be skipped. Furthermore, it can be assumed that the wall is a face-centered cubic (fcc) lattice which is aligned such that the (100)-plane is oriented parallel to the wall-fluid interface [16]. Due to the relatively large size of the confining walls (in directions perpendicular to the confinement axis) compared to the length scale of

the components of the investigated sample (colloids) the wall surface in x - and y -direction can be expanded to infinity. This means that the overall potential of the confining (100)-monolayer can be calculated by the integration of Eq. (2.1). Using the mean surface density n_A we yield

$$u_{FS}^{mono}(z) = \int_{-\infty}^{\infty} \int_{-\infty}^{\infty} n_A u_{LJ}^{repulsive}(|\mathbf{r} - \mathbf{r}'|) dx dy \quad (2.2a)$$

$$= \frac{4}{5} \pi \tilde{\epsilon} n_A \tilde{\sigma}^2 \left(\frac{\tilde{\sigma}}{z - z'} \right)^{10}. \quad (2.2b)$$

In Eq. (2.2b) the index FS denotes the interaction between the confined fluid and the solid walls. The ratio between the system thickness along the confinement direction (z -axis) and the width of confining walls is usually very small. Therefore, we can assume that the latter is composed of infinite number of (100)-planes stacked atop each other [16]. Consequently considering infinitely thick confining walls, which interfaces with the fluid are positioned at $z = \pm L_z/2$, Eq. (2.2b) can be integrated along the confinement direction. The result reads

$$u_{SW} = \int_{\pm L_z/2}^{\infty} n_L u_{FS}^{mono}(z - z') dz' \quad (2.3a)$$

$$= \frac{4}{45} \pi \tilde{\epsilon} n_A n_L \tilde{\sigma}^3 \left(\frac{\tilde{\sigma}}{z \pm L_z/2} \right)^9. \quad (2.3b)$$

Note that we set the density along the z -axis to n_L . In the remainder of our study using the soft-wall (SW) potential from Eq. (2.3b) we set $n_A n_L \tilde{\sigma}^3 = 9$ as well as $\tilde{\epsilon}/(k_B T) = 1$.

2.2 Charged particles at surfaces

Aiming to characterize the charge induced forces acting between colloids it is necessary to take the influence of counterions dissolved in the solvent into account. Charged colloids attract counterions which results in a formation of an *ionic atmosphere* around them. In combination with large colloidal surfaces this ionic clouds tend to form a kind of charged double layers which screen the colloidal charge.

Thus, an appropriate description of the mutual interaction between charged colloids makes the detailed consideration of screening necessary. For this purpose in the next section we want to discuss the effects occurring in the vicinity of charged surfaces. Then, the derivation of the DLVO potential will be presented.

2.2.1 Charge screening at surfaces

Before the description of the interaction between spherical particles in suspensions can be started it is necessary to consider the processes at the interface between the solid surfaces and polar fluids. Surfaces in contact with dipolar liquids tend to become charged [129]. This kind of influence is observed for instance in water. Its relatively large dielectric constant induces the dissociation of ions from the material surface. In the dissociation process molecules as well as ionic compounds split into smaller particles such as atoms, ions or radicals. The separation occurs usually in a reversible manner. For instance oxides in contact with water usually loose protons of the hydroxyl group, and remain with a negative surface charge ($\sim \text{OH} \rightarrow \sim \text{O}^- + \text{H}^+$). The dissociation therefore can induce a significant charge difference between the negatively charged surface and positive protons which induces an electric field. This attractive field for its part also influences the distribution of counterions in the solution. As a consequence the Coulomb interaction of the charged surface is effectively screened by the cloaking ionic film. The combination of the resulting ionic layer with the charged surface can be viewed as an *electric double layer*. In the first description of this process it was assumed that in equilibrium protons are directly located on the surface and, thereby, neutralize it. Due to the great similarities between the proposed model and the plate capacitor the model was called *Helmholtz layer* [see Fig. (2.1a)]. While this model could explain some basic phenomena of the double layer, it failed during measurements of the capacitance of the electric double layer. An improved description of the behavior at the planar surface was proposed in 1910-1917 by Gouy and Chapman [130, 131]. They not only considered the Coulomb interaction but also a second

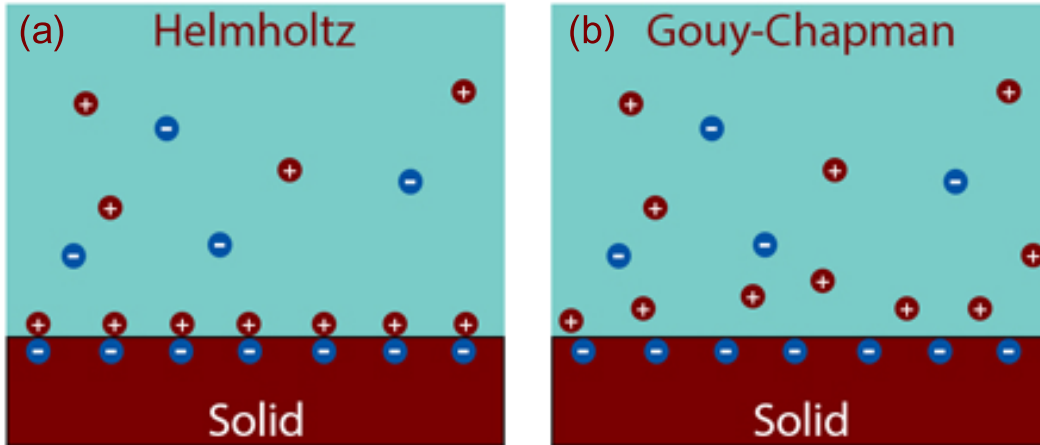


Figure 2.1: Helmholtz and Gouy-Chapman model of the electric double layer.

crucial effect: thermal fluctuations caused by the solvent. While thermal fluctuations drive the diffusion of ions, Coulomb interaction attracts oppositely charged ions towards the surface. These contradicting forces find a compromise in the stabilization of a thin film of fluctuating ions in the vicinity of the charged surface [see Fig. (2.1b)].

To access the system analytically the processes occurring in the solvent can be coarse grained by the introduction of the mean field (also extending the system by addition of co- and counter ions, e.g., salt) and described via the Poisson-Boltzmann theory. Therefore, using Poisson equation for the effective potential $\phi(\mathbf{r})$ we can write

$$\nabla^2 \phi(\mathbf{r}) = -\frac{\rho_z(\mathbf{r})}{\epsilon_r \epsilon_0}, \quad (2.4)$$

where ϵ_0 and ϵ_r stand for the vacuum and the relative permittivity, respectively and the function $\rho_z(\mathbf{r})$ in Eq. (2.4) describes the overall local charge density. Then we can assume that the charge density of co- and counterions of species ν is given by the Boltzmann distribution

$$\rho_{z,\nu}(\mathbf{r}) = z_\nu e_0 c_0 \exp(-W_\nu(\mathbf{r})/k_B T). \quad (2.5)$$

In Eq. (2.5) the parameter W_ν describes the work which is necessary to move an ion of species ν , with the valency z_ν , from infinity towards the surface. Furthermore, c_0 denotes the bulk ion concentration and e_0 is the elementary charge. As this description is based on the mean field approach and correlations are neglected, it is restricted to monovalent charged ions, for which no strong correlations exist [132–134]. Moreover, we assume that the salt concentration is much larger than that of the dissolved ions. Otherwise the number of anions and cations would be unequal, breaking the electroneutrality condition. The framework of the Poisson-Boltzmann theory also neglects the mutual ion-ion interaction reducing it to the effective potential $\phi(\mathbf{r})$. For the monovalent anions and cations discussed here, with $z_\pm = \pm 1$, the work is given by $W_\pm(\mathbf{r}) = z_\pm e_0 \phi(\mathbf{r})$. Now defining the overall local charge density as $\rho_z(\mathbf{r}) = \sum_\nu \rho_{z,\nu}(\mathbf{r})$ the results from Eq. (2.5) can be plugged into Eq. (2.4) which yields the Poisson-Boltzmann equation

$$\nabla^2 \phi(\mathbf{r}) = -\frac{e_0 c_0}{\epsilon_r \epsilon_0} \sum_\nu z_\nu \exp\left(-\frac{z_\nu e_0 \phi(\mathbf{r})}{k_B T}\right). \quad (2.6)$$

This equation can be solved analytically for simple geometries, e.g. a planar surface. We have to keep in mind that the Poisson-Boltzmann theory is restricted to the low density case. The considered mean field theory neglects possible local correlations and structure dependencies. As a consequence the ansatz discussed here becomes inappropriate for large densities, where the particles approach each other and the real structure of molecules becomes more and more important.

Linearizing the Eq. (2.6) up to the second order of $\phi(\mathbf{r})$ under the assumption of small $\phi(\mathbf{r})$ we get

$$\nabla^2 \phi(\mathbf{r}) = -\frac{e_0 c_0}{\epsilon_r \epsilon_0} \sum_\nu z_\nu \left(1 - \frac{z_\nu e_0 \phi(\mathbf{r})}{k_B T}\right). \quad (2.7)$$

It is obvious that taking into account the electroneutrality condition the first term vanishes. For a flat plain oriented perpendicular to the x -axis and positioned at $x = 0$ the solution of Eq. (2.7) reads

$$\phi(z) = \psi_S \exp(-\kappa x), \quad (2.8)$$

when $\phi(z \rightarrow 0) = \psi_S$ as well as $\phi(x \rightarrow \infty) = 0$ hold [135]. The parameter ψ_S can be considered as a surface potential.

The discussion performed here is all the more important as the proposed approach was applied by Debye and Hückel [136] to derive the effective interaction potential of steric charge-stabilized spherical particles, which will be discussed in more detail in Sec. 2.2.2.

2.2.2 Derjaguin-Landau-Verwey-Overbeek theory

The simulation of charged colloidal suspensions which is based on the explicit calculation (so called primitive model [132]) of all macro-, co- and counterions interacting via the Coulomb potential is very elaborate due to the significant differences in the number and size of interacting particles as well as their characteristic time scales. To be more precise small solvent particles and dissolved ions are much faster than the considerably larger macroions (colloids). Moreover, in numerical simulations of colloidal suspensions in which a sufficient large number of macroions must be taken into account the calculation of a far greater numbers of co- and counterions is necessary. In addition to all these difficulties the direct evaluation of the long-range Coulomb interaction is also very time consuming.

In the current section we want to present the theoretical background of the method which enables to reduce the calculation effort significantly. In this approach the reduction of the long-range potential into the short-range interaction was favored. The solution was to generalize the exact interaction between co- and counterions through the introduction of the mean field description. For this purpose it is essential to understand the behaviour of the coarse-grained particles in detail. Of especial interest in this context are small ions in the surrounding of large macroions. On one hand for reasons of entropy the particles tend to distribute homogeneously in the solvent. On the other hand assuming that particles interact via radial Coulomb interaction and neglecting polarization effects, the counterions are attracted by the oppositely charged macroions. This disrupts the uniform

distribution within the system [see Sec. 2.2.1]. The balance of both counteracting effects is reached when the chemical potential of ions near the macroions is equal to the chemical potential far from wall or colloidal surface (bulk). Under this condition the counterions are observed to wrap the macroions and form an effective double layer, as discussed in Sec. 2.2.1. This leads to the sterical charge-stabilization of macroions. Although the complete DLVO theory consists of the repulsive and attractive parts, in the following we will neglect the short-range Van-der-Waals interaction [4]. This is justified since assume that in the considered system the distance between particles is always larger than the interaction radius of the Van-der-Waals force. Therefore, the attractive contribution to the DLVO potential which is crucial for the description of precipitation and coagulation can be disregarded. However, in contrast to the attractive short-range interaction the long-range component of the DLVO potential is the basis for the current work. Therefore the detailed derivation of this contribution which is very well described in [135] will be presented below.

To obtain the desired mean field potential we must start from the definition of the potential energy which reads

$$V(\{\mathbf{R}_i\}, \{\mathbf{r}_j\}) = V_{MM}(\{\mathbf{R}_i\}) + V_{Mm}(\{\mathbf{R}_i\}, \{\mathbf{r}_j\}) + V_{mm}(\{\mathbf{r}_j\}). \quad (2.9)$$

In this equation M stands for macro- and m for microions. Furthermore, we assume the ensemble to be a semi-grand canonical in the sense that the number of macroions, N_M , is held constant whereas the number of microions N_m is allowed to vary. The canonical partition function for the microions is then given by

$$Q_{N_M} = \frac{1}{N_M! \Lambda_M^{3N_M}} \int \exp(-\beta V_{MM}) \Xi_m(\mu_+, \mu_-, V, T; \{\mathbf{R}_i\}) d\mathbf{R}^{N_M}. \quad (2.10)$$

In the latter equation the function Ξ_m stands for the grand-canonical partition function of microions

$$\Xi_m = \sum_{N_+=0}^{\infty} \sum_{N_-=0}^{\infty} \frac{\xi_+^{N_+} \xi_-^{N_-}}{N_+! N_-!} \int \int \exp[-\beta(V_{Mm} + V_{mm})] d\mathbf{r}^{N_+} d\mathbf{r}^{N_-}. \quad (2.11)$$

In Eq. (2.11) the activity of microions ξ is defined by $\xi_\nu = \exp(\beta\mu_\nu)/\Lambda_\nu^3$ with the thermal wavelength Λ_M and the chemical potential μ . Now we introduce the effective potential acting on each macroion which reads

$$V_{eff}(\{\mathbf{R}_i\}) = V_{MM}(\{\mathbf{R}_i\}) + \Omega_m(\mu_+, \mu_-, V, T; \{\mathbf{R}_i\}), \quad (2.12)$$

where the grand potential Ω_m is connected to the grand partition function of microions in Eq. (2.11) via the relation

$$\Omega_m = -k_B T \ln \Xi_m. \quad (2.13)$$

This definition allows us to rewrite Eq. (2.10) in

$$Q_{N_M} = \frac{1}{N_M! \Lambda^{3N_M}} \int \exp[-\beta V_{eff}(\{\mathbf{R}_i\})] d\mathbf{R}^{N_M}. \quad (2.14)$$

Note that the function V_{eff} is not pairwise additive since it is made up of the volume dependent non-additive microion component Ω_m as well as the pairwise additive interaction between macroions V_{MM} . Next we define the total external potential acting on the microions of species ν

$$\phi_\nu(\mathbf{r}) = \sum_{i=1}^{N_M} u_{M\nu}(|\mathbf{r} - \mathbf{R}_i|) \quad (2.15)$$

due to the macroion-microion interaction $u_{M\nu}$.

At this point it is necessary to rewrite the grand potential Ω_m in more accessible way. For this purpose we change from single particle to density (ρ_ν) representation.

As a consequence Eq. (2.13) reads

$$\Omega[\rho_\nu] = F[\rho_\nu] - \sum_\nu \int [\mu_\nu - \phi_\nu(\mathbf{r})] \rho_\nu(\mathbf{r}) d\mathbf{r}. \quad (2.16)$$

The functional of the free energy $F[\rho_\nu]$ can be separated in several contributions by writing

$$F[\rho_\nu] = \sum_{\nu} F_{\nu}^{id} + F^c + F^{corr}. \quad (2.17)$$

Restricting our attention to the mean-field description of microions it can be assumed that the fluid behaves like an ideal gas. This implies that correlation effects can be neglected and the particles feel only the average electrostatic potential of the system [16]. For this reason we can set $F^{corr} = 0$. The remaining terms in the latter equation stand for the free energy of the ideal gas of the species ν

$$F_{\nu}^{id} = k_B T \int \rho_{\nu}(\mathbf{r}) (\ln[\Lambda_{\nu}^3 \rho_{\nu}(\mathbf{r})] - 1) d\mathbf{r} \quad (2.18)$$

and the free energy contribution resulting from the Coulomb interaction of all microions which can be expressed by the mean-field approach

$$F^c = \frac{1}{2} e_0 \int \Phi^c(\mathbf{r}) \rho_z(\mathbf{r}) d\mathbf{r}, \quad (2.19)$$

with the local charge density of the fluid, which reads

$$\rho_z(\mathbf{r}) = \sum_{\nu} z_{\nu} \rho_{\nu}(\mathbf{r}). \quad (2.20)$$

The electrostatic potential $\Phi^c(\mathbf{r})$ used in Eq. (2.19) satisfies the Poisson's equation

$$\nabla^2 \Phi^c(\mathbf{r}) = -\frac{e_0 \rho_z(\mathbf{r})}{\epsilon_r \epsilon_0}. \quad (2.21)$$

As a consequence it can be accessed via the Green's function $G(\mathbf{r}, \mathbf{r}')$

$$\Phi^c(\mathbf{r}) = e_0 \int G(\mathbf{r}, \mathbf{r}') \rho_z(\mathbf{r}') d\mathbf{r}'. \quad (2.22)$$

Writing $G(\mathbf{r}, \mathbf{r}')$ in Coulombic form

$$G(\mathbf{r}, \mathbf{r}') = \frac{1}{4\pi \epsilon_r \epsilon_0 |\mathbf{r} - \mathbf{r}'|} \quad (2.23)$$

we can insert Eq. (2.23) in Eq. (2.22). Then it follows that the mean field approximation of the Coulomb interaction of the free energy defined in Eq. (2.19) can be expressed by

$$F^c = \frac{e_0^2}{2} \int \int \frac{\rho_z(\mathbf{r})\rho_z(\mathbf{r}')}{4\pi\epsilon_r\epsilon_0|\mathbf{r} - \mathbf{r}'|} d\mathbf{r}d\mathbf{r}'. \quad (2.24)$$

At this point it is already possible to apply the variation principle in Eq. (2.16) and solve the resulting set of coupled differential equations via MD [137]. However, since we are interested in the analytical derivation of the DLVO potential which was used in our investigations it is necessary to continue analytical considerations. For this purpose we additionally assume that the macroions induce only small inhomogeneities in the density distribution such that the free energy in Eq. (2.17) can be expanded in terms of deviation of the local density $\rho_\nu(\mathbf{r})$ from the bulk value n_ν

$$\Delta\rho_\nu(\mathbf{r}) = \rho_\nu(\mathbf{r}) - n_\nu. \quad (2.25)$$

With Eq. (2.25) the integrand of the free energy in Eq. (2.18) can be expanded to

$$\begin{aligned} \rho_\nu(\mathbf{r}) (\ln[\Lambda_\nu^3\rho_\nu(\mathbf{r})] - 1) &\approx n_\nu (\ln[\Lambda_\nu^3n_\nu] - 1) \\ &+ \ln[\Lambda_\nu^3n_\nu]\Delta\rho_\nu(\mathbf{r}) + \frac{1}{2n_\nu} (\Delta\rho_\nu(\mathbf{r}))^2. \end{aligned} \quad (2.26)$$

Now plugging Eq. (2.26) in Eq. (2.18), Eq. (2.18) and Eq. (2.24) in Eq. (2.17) as well as Eq. (2.17) in Eq. (2.16) results in

$$\begin{aligned} \Omega[\Delta\rho_\nu] &= \sum_\nu \left(k_B T \ln[\Lambda_\nu^3n_\nu] \int \Delta\rho_\nu(\mathbf{r}') d\mathbf{r}' + \frac{k_B T}{2n_\nu} \int (\Delta\rho_\nu(\mathbf{r}'))^2 d\mathbf{r}' \right) \\ &+ \frac{e_0^2}{2} \int \int \frac{\rho_z(\mathbf{r}')\rho_z(\mathbf{r}'')}{4\pi\epsilon_r\epsilon_0|\mathbf{r}' - \mathbf{r}''|} d\mathbf{r}'d\mathbf{r}'' - \sum_\nu \int (\mu_\nu - \phi_\nu(\mathbf{r}'))\rho_\nu(\mathbf{r}') d\mathbf{r}' \\ &+ \sum_\nu k_B T \int n_\nu (\ln[\Lambda_\nu^3n_\nu] - 1) d\mathbf{r}'. \end{aligned} \quad (2.27)$$

Aiming to find the density distribution with the minimal free energy we replace the chemical potential μ_ν by its ideal value

$$\mu_\nu^{id} = k_B T \ln[\Lambda^3 n_\nu], \quad (2.28)$$

and use the variation principle minimizing the grand potential in Eq. (2.27) with respect to $\Delta\rho_\nu(\mathbf{r})$. The result is given by

$$0 = \frac{\delta\Omega[\Delta\rho_\nu]}{\delta\Delta\rho_\nu(\mathbf{r})} \quad (2.29a)$$

$$\begin{aligned} &= \sum_\nu \left(k_B T \ln[\Lambda_\nu^3 n_\nu] \int \delta(\mathbf{r} - \mathbf{r}') d\mathbf{r}' + \frac{k_B T}{n_\nu} \int \Delta\rho_\nu(\mathbf{r}') \delta(\mathbf{r} - \mathbf{r}') d\mathbf{r}' \right) \\ &+ \frac{e_0^2}{2} \sum_\nu \int \int \frac{z_\nu \delta(\mathbf{r} - \mathbf{r}') \rho_z(\mathbf{r}'') + z_\nu \delta(\mathbf{r} - \mathbf{r}'') \rho_z(\mathbf{r}')}{4\pi\epsilon_r\epsilon_0 |\mathbf{r}' - \mathbf{r}''|} d\mathbf{r}' d\mathbf{r}'' \\ &- \sum_\nu \int \mu_\nu^{id} \delta(\mathbf{r} - \mathbf{r}') d\mathbf{r}' + \sum_\nu \int \phi_\nu(\mathbf{r}') \delta(\mathbf{r} - \mathbf{r}') d\mathbf{r}'. \end{aligned} \quad (2.29b)$$

From Eq. (2.29b) we yield two equations for co- and counterions ($\nu = +$ and $\nu = -$)

$$-\phi_\nu(\mathbf{r}) = \frac{\Delta\rho_\nu(\mathbf{r}) k_B T}{n_\nu} + z_\nu e_0 \Phi^c(\mathbf{r}), \quad (2.30)$$

which are coupled through the electrostatic potential Φ_c . Although the radius of macroions R , is finite, to continue the analytical description we have to consider the macroions as point-like particles. Later this assumption will be corrected by renormalization of their charges (via the introduction of the finite diameter of macroions). With this assumption the Coulomb contribution to the external potential of macroions $\phi_\nu(\mathbf{r})$ can be expressed by

$$\phi_\nu(\mathbf{r}) = z_\nu e_0 \Phi^{ext}(\mathbf{r}) \quad (2.31a)$$

$$= z_\nu \sum_i^{N_M} \frac{Z e_0^2}{4\pi\epsilon_r\epsilon_0} \frac{1}{|\mathbf{r} - \mathbf{R}_i|}. \quad (2.31b)$$

In the latter equation the quantity Φ^{ext} describes the external electrostatic potential of point-like macroions. All these considerations enable us to write the total

electrostatic potential for macro- and microions which reads

$$\Phi(\mathbf{r}) = \Phi^c(\mathbf{r}) + \Phi^{ext}(\mathbf{r}) = e_0 \int \frac{\rho_z(\mathbf{r}') + Z\rho_{ext}(\mathbf{r}')}{4\pi\epsilon_r\epsilon_0|\mathbf{r} - \mathbf{r}'|} d\mathbf{r}', \quad (2.32)$$

where the microscopic density of macroions is given by

$$\rho_{ext}(\mathbf{r}) = \sum_i^{N_M} \delta(\mathbf{r} - \mathbf{R}_i). \quad (2.33)$$

Combining the results from Eq. (2.31b), Eq. (2.32) and Eq. (2.33) we derive the deviation from the microion density in Eq. (2.32) which reads

$$\Delta\rho_\nu(\mathbf{r}) = -\frac{n_\nu z_\nu e_0^2}{k_B T} \int \frac{\rho_z(\mathbf{r}') + Z\rho_{ext}(\mathbf{r}')}{4\pi\epsilon_r\epsilon_0|\mathbf{r} - \mathbf{r}'|} d\mathbf{r}'. \quad (2.34)$$

Focusing on the salt-free case (assuming that the microions consist only of the species of counterions) we can drop the subscript ν setting $\rho_z(\mathbf{r}) = z\rho(\mathbf{r})$. Then we analytically solve the integral in Eq. (2.34) via the Fourier transform denoted by $\mathcal{F}[\dots]$. Applying the Fourier transform to both sides of Eq. (2.34), it can be expressed as

$$\mathcal{F}[\Delta\rho_\nu(\mathbf{r})] = -\frac{nz e_0^2}{k_B T} \int \frac{z\rho(\mathbf{r}') + Z \sum_i^{N_M} \delta(\mathbf{r}' - \mathbf{R}_i)}{4\pi\epsilon_r\epsilon_0} \mathcal{F}\left[\frac{1}{|\mathbf{r} - \mathbf{r}'|}\right] d\mathbf{r}'. \quad (2.35)$$

Now we use Eq. (2.25) on the left hand side of Eq. (2.35) and demand that the equations $\mathcal{F}[\rho(\mathbf{r})] = \hat{\rho}(\mathbf{k})$ and $\mathcal{F}[n] = n\delta(\mathbf{k})$ hold. Furthermore, we know that the Fourier transform of the Coulomb potential is given by $\mathcal{F}\left[\frac{1}{|\mathbf{r} - \mathbf{r}'|}\right] = \frac{4\pi}{k^2} e^{-i\mathbf{k}\mathbf{r}'}$. Summarizing all these information and making use of the convolution theorem it is possible to transform Eq. (2.35) into

$$\hat{\rho}(\mathbf{k}) - n\delta(\mathbf{k}) = -\frac{nze_0^2}{k_B T k^2} \left[\frac{z}{\epsilon_r\epsilon_0} \hat{\rho}(\mathbf{k}) + \frac{Z}{\epsilon_r\epsilon_0} \sum_{i=1}^{N_M} e^{-i\mathbf{k}\mathbf{R}_i} \right]. \quad (2.36)$$

In the following we can neglect the Delta function in Eq. (2.36) since this term contributes only for $\mathbf{k}=0$ ($r \rightarrow \infty$). Introducing the square of the inverse Debye

length

$$\kappa^2 = \frac{nz^2e_0^2}{\epsilon_r\epsilon_0k_B T} \quad (2.37)$$

the Eq. (2.36) can be rewritten to

$$\hat{\rho}(\mathbf{k}) = -\frac{Z\kappa^2}{z(k^2 + \kappa^2)} \sum_{i=1}^{N_M} e^{-i\mathbf{k}\mathbf{R}_i}. \quad (2.38)$$

To derive the analytical expression for the density distribution of microions $\rho(\mathbf{r})$ (for a given macroion configuration) the Eq. (2.38) must be transformed back into the r -space. The corresponding inverse Fourier transform of Eq. (2.38) reads

$$\mathcal{F}^{-1}[\hat{\rho}(\mathbf{k})] = \rho(\mathbf{r}) \quad (2.39a)$$

$$= -\frac{Z\kappa^2}{z(2\pi)^3} \sum_{i=1}^{N_M} \int_0^\infty dk \int_0^{2\pi} d\phi \int_{-1}^1 d\cos\theta k^2 \times \frac{1}{k^2 + \kappa^2} \exp(ik|\mathbf{r} - \mathbf{R}_i| \cos\theta). \quad (2.39b)$$

The integration over ϕ and θ the Eq. (2.39b) yields

$$\rho(\mathbf{r}) = -\frac{Z\kappa^2}{z(2\pi)^2} \sum_{i=1}^{N_M} \frac{1}{i|\mathbf{r} - \mathbf{R}_i|} \times \left[\int_0^\infty dk \frac{k}{k^2 + \kappa^2} \exp(ik|\mathbf{r} - \mathbf{R}_i|) - \int_0^\infty dk \frac{k}{k^2 + \kappa^2} \exp(-ik|\mathbf{r} - \mathbf{R}_i|) \right]. \quad (2.40)$$

Transforming $k \rightarrow -k$ in the second integrand of Eq. (2.40) we can see that the both integrands in Eq. (2.40) become equal such that the integrals differ only in the definition of their boundaries. However, the $[0 : \infty]$ boundary of the first integral and the $[-\infty : 0]$ boundary of the second one can be combined in one single integral with $[-\infty : \infty]$ which enables us to rewrite Eq. (2.40) as

$$\rho(\mathbf{r}) = -\frac{Z\kappa^2}{z(2\pi)^2} \sum_{i=1}^{N_M} \frac{1}{i|\mathbf{r} - \mathbf{R}_i|} \int_{-\infty}^\infty dk \frac{k}{k^2 + \kappa^2} \exp(ik|\mathbf{r} - \mathbf{R}_i|). \quad (2.41)$$

This integral can be solved via the Cauchy's integral equation. Furthermore, if we demand that counterions are monovalent ($z = -1$) the resulting microion density reads

$$\rho(\mathbf{r}) = \frac{Z\kappa^2}{4\pi} \sum_{i=1}^{N_M} \frac{\exp(-\kappa|\mathbf{r} - \mathbf{R}_i|)}{|\mathbf{r} - \mathbf{R}_i|} \quad (2.42a)$$

$$= \sum_{i=1}^{N_M} \rho_i(\mathbf{r}). \quad (2.42b)$$

Eq. (2.42b) defines the density distribution of microions which can be associated with the superposition of single macroion profiles. As mentioned before for the derivation of Eq. (2.42a) the point-like behavior of macroions was assumed. Next we reintroduce the finite diameter of macroions. This can be done by the constraint $\rho(\mathbf{r}) = 0$ for $|\mathbf{r} - \mathbf{R}_i| < R$, which implies that macroions cannot overlap with microions. The combination of this constraint together with the charge neutrality condition can be summarized by

$$\int_{|\mathbf{r} - \mathbf{R}_i| > R} \rho(\mathbf{r}) d\mathbf{r} = |Z|. \quad (2.43)$$

Note that this assumption holds only for a very small overlap of electric double layers of macroions (small particle density which is related to the Debye-Hückel approximation [136]). Inserting Eq. (2.42a) in Eq. (2.43) and solving Eq. (2.43) via the spherical coordinates the macroion charge Z in Eq. (2.42a) can be replaced by the renormalized charge

$$Z' = |Z| \frac{\exp(\kappa R)}{1 + \kappa R}, \quad (2.44)$$

such that the final microion density distribution for the particle i is given by

$$\rho_i(\mathbf{r}) = \frac{Z'\kappa^2}{4\pi} \frac{\exp(-\kappa|\mathbf{r} - \mathbf{R}_i|)}{|\mathbf{r} - \mathbf{R}_i|}. \quad (2.45)$$

The corresponding electrostatic potential $\Phi_i(\mathbf{r})$ is described by the Poisson's equation

$$\nabla^2 \Phi_i(\mathbf{r}) = -\frac{e_0 \rho(\mathbf{r})}{\epsilon_r \epsilon_0} \quad (2.46)$$

from which it follows that

$$\Phi(\mathbf{r}) = \sum_{i=1}^{N_M} \frac{Z' e_0}{4\pi \epsilon_r \epsilon_0} \frac{\exp(-\kappa |\mathbf{r} - \mathbf{R}_i|)}{|\mathbf{r} - \mathbf{R}_i|} \quad (2.47a)$$

$$= \sum_{i=1}^{N_M} \Phi_i(\mathbf{r}) \quad (2.47b)$$

holds. Now it is time to return to the structure of the effective potential of the whole system inserting Eq. (2.27) into Eq. (2.12) as well as to make use of Eq. (2.31a). Furthermore, the assumption that the considered model contains only one sort of microions (counterions) justifies the definition $\rho_z(\mathbf{r}) = \rho(\mathbf{r})$. The resulting equation reads

$$V_{eff}(\{\mathbf{R}_i\}) = V_{MM}(\{\mathbf{R}_i\}) + V_M + \int z e_0 \Phi^{ext}(\mathbf{r}) \rho(\mathbf{r}) d\mathbf{r} \quad (2.48a)$$

$$= V_{MM}(\{\mathbf{R}_i\}) + V_M + \sum_{i=1}^{N_M} \sum_{j=i+1}^{N_M} u_{eff}(|\mathbf{R}_i - \mathbf{R}_j|). \quad (2.48b)$$

i In the equation above the value V_M is structure-independent and thus does not influence the force between the macroions. The effective interaction potential in Eq. (2.48b) which can be derived inserting the external potential of macroions into Eq. (2.31b) as well as the microion density in Eq. (2.45) into Eq. (2.48a) is given by

$$u_{eff}(|\mathbf{R}_j - \mathbf{R}_i|) = -\frac{Z'^2 e_0^2 \kappa^2}{16\pi^2 \epsilon_r \epsilon_0} \int \frac{\exp(-\kappa |\mathbf{r} - \mathbf{R}_i|)}{|\mathbf{r} - \mathbf{R}_i|} \frac{1}{|\mathbf{r} - \mathbf{R}_j|} d\mathbf{r}. \quad (2.49)$$

To solve the integral in the above equation we can repeatedly make use of the Fourier transform. It is also important to pay attention to the fact, that due to the Coulomb potential with finite particle size the charge Z in Eq. (2.31b) must be replaced by the effective charge Z' [see Eq. (2.44)]. The result of the Fourier

transform of Eq. (2.49) is the effective potential of macroions in the k -space

$$u_{eff}(\mathbf{k}) = -\frac{Z'^2 e_0^2}{\epsilon_r \epsilon_0} \frac{\kappa^2}{k^2(k^2 + \kappa^2)}. \quad (2.50)$$

The back transformation of Eq. (2.50) with respect to $\mathbf{R}_j - \mathbf{R}_i$ results in an integral which can be solved in spherical coordinates. Then applying the residue theorem we derive the effective potential between two macroions located at \mathbf{R}_i and \mathbf{R}_j and surrounded by microions. The resulting effective potential reads

$$u_{eff}(|\mathbf{R}_j - \mathbf{R}_i|) = W \frac{\exp(-\kappa|\mathbf{R}_j - \mathbf{R}_i|)}{|\mathbf{R}_j - \mathbf{R}_i|}, \quad (2.51)$$

with coupling constant

$$W = \frac{Z'^2 e_0^2}{4\pi \epsilon_r \epsilon_0}. \quad (2.52)$$

As up to now only one species of counterions was allowed, in the last step it is necessary to generalize the definition for the inverse Debye length κ defined in Eq. (2.37) allowing the fluid to contain different species of counterions (salt). Therefore, removing the restriction to one species Eq. (2.37) transforms to

$$\kappa^2 = \frac{1}{\epsilon_r \epsilon_0 k_B T} \left(n(z e_0)^2 + \sum_{\nu} n_{\nu} (z_{\nu} e_0)^2 \right), \quad (2.53)$$

where ν describes different species of salt ions. Furthermore, still demanding the monovalency ($|z| = 1$) the charge neutrality between macro- and microions is satisfied if $n = |Z|\rho$, where ρ denotes the density of macroions. Finally defining the ionic strength by $IN_A = (1/2) \sum_{\nu} n_{\nu} z_{\nu}^2$ we obtain the generalized inverse Debye length

$$\kappa = \sqrt{\frac{e_0^2}{\epsilon_r \epsilon_0 k_B T} (Z\rho + 2IN_A)}. \quad (2.54)$$

2.3 Soft-sphere potential

The requirement to understand, explain and in the ideal case to predict experimental results via theoretical models or numerical simulations makes it necessary to describe the real system in the best possible way. One of such points dealing with colloids is the steric interaction, which takes into account a finite diameter and prevents the particles from overlapping. Although, in systems where DLVO potential is considered the calculation of this interaction is of secondary importance, it is usually still considered for the sake of completeness [138]. As a consequence, the precise form of the steric potential leads only to small quantitative differences and is therefore not decisive.

There are two common ways which are used to mimic the core of the particle. The first one is the hard core interaction which is characterized by the infinite potential at interparticle distances smaller than the particle diameter $\tilde{\sigma}$ [139, 140]. The second approach is the soft-core interaction [138, 141] described by the repulsive part of the Lennard-Jones potential in Eq. (2.1), which can be expressed as

$$u_{SS} = 4\tilde{\epsilon} \left(\frac{\tilde{\sigma}}{r} \right)^{12}. \quad (2.55)$$

For the simulation of the steric repulsion in our study the soft-sphere interaction presented in Eq. (2.55) was chosen.

2.4 Structural observables

In the following sections we will introduce a selection of observables frequently used in this thesis.

2.4.1 Density

The properties of the most physical systems containing large number of interacting particles are strongly connected to the common particle number density given by

$$\rho = \frac{N}{V}. \quad (2.56)$$

In experimental studies, this physical quantity can be accessed via the volume fraction which reads

$$\phi = \frac{\pi\rho\tilde{\sigma}^3}{6}. \quad (2.57)$$

By confining a system between two plane parallel walls, we break the translational symmetry of the system. This results in the appearance of inhomogeneities in the density profile, e.g., layering perpendicular to the confinement axis. Therefore, the homogeneous particle number density in Eq. (2.56) does not provide sufficient information about the particle distribution. Thus, in cases where the information concerning the density distribution was decisive the calculation of the one dimensional normalized local density along the symmetry breaking axis (in our study z -axis)

$$\rho(z + \Delta z) = \left\langle \frac{N(z + \Delta z)}{N\Delta z} \right\rangle, \quad (2.58)$$

was performed.

2.4.2 Radial pair distribution function

In the current section we introduce the radial distribution function $g(r)$ which plays a key role in the description of monoatomic liquids [16]. It indicates the extent to which the system structure deviates from complete randomness. To obtain $g(r)$ it is necessary to start from the two particle distribution function

which reads

$$g_N(\mathbf{r}, \mathbf{r}') = \frac{\rho^{(2)}(\mathbf{r}, \mathbf{r}')}{\rho(\mathbf{r})\rho(\mathbf{r}')}, \quad (2.59)$$

with the single particle density

$$\rho(\mathbf{r}) = \left\langle \sum_{i=1}^N \delta(\mathbf{r} - \mathbf{r}_i) \right\rangle, \quad (2.60)$$

and the pair particle density

$$\rho^{(2)}(\mathbf{r}, \mathbf{r}') = \left\langle \sum_{i=1}^N \sum_{i \neq j}^N \delta(\mathbf{r} - \mathbf{r}_i) \delta(\mathbf{r}' - \mathbf{r}_j) \right\rangle. \quad (2.61)$$

Note that for a homogeneous system the single particle density in Eq. (2.60) is equivalent to Eq. (2.56). From Eq. (2.61) follows that considering the relative distance between the particles instead of the absolute coordinates the pair particle density in Eq. (2.61) can also be expressed by

$$\rho^{(2)}(\mathbf{r}', \mathbf{r}' + \mathbf{r}) = \left\langle \sum_{i=1}^N \sum_{i \neq j}^N \delta(\mathbf{r}' - \mathbf{r}_i) \delta(\mathbf{r}' + \mathbf{r} - \mathbf{r}_j) \right\rangle. \quad (2.62)$$

Being only interested in the relative distance between the particles we can reduce Eq. (2.62) integrating it over the absolute coordinate of the reference particle \mathbf{r}' which yields

$$\int_{\mathbb{R}^3} \rho^{(2)}(\mathbf{r}', \mathbf{r}' + \mathbf{r}) d\mathbf{r}' = \left\langle \sum_{i=1}^N \sum_{i \neq j}^N \delta(\mathbf{r} + \mathbf{r}_i - \mathbf{r}_j) \right\rangle. \quad (2.63)$$

Summarizing all these results and assuming that the system is homogeneous and isotropic we get the definition of the radial distribution function which reads

$$g(r) = \frac{1}{V} \int_{\mathbb{R}^3} g_N^{(2)}(\mathbf{r}', \mathbf{r}' + \mathbf{r}) d\mathbf{r}' \quad (2.64a)$$

$$= \frac{1}{\rho N} \left\langle \sum_{i=1}^N \sum_{i \neq j}^N \delta(\mathbf{r} + \mathbf{r}_i - \mathbf{r}_j) \right\rangle \quad (2.64b)$$

The importance of this function can be explained by the fact that the value of $g(r)$ can be directly measured in light-scattering experiments and thus provides a direct connection between theoretical studies and direct experimental measurements. From Eq. (2.64b) follows that the function $g(r)$ within a two dimensional layer can be expressed as

$$g(r) = \frac{\langle N^{layer}(r_1, r_2) \rangle}{N^{layer} \rho^{layer} \pi(r_2^2 - r_1^2)}. \quad (2.65)$$

In Eq. (2.65) N^{layer} denotes the number of particles and ρ^{layer} the 2D density of the considered layer. Furthermore, $\langle N^{layer}(r_1, r_2) \rangle$ is an ensemble average over the particles positioned in a shell between the radii r_1 and r_2 . Since the form of $g(r)$ gives an insight into the structure of the investigated system it will be used for measurements of the mean distance between neighboring particles. This quantity will be of crucial importance for the calculation of the bond angle order presented in the next section.

2.4.3 Bond angle order parameter

Aiming to understand the processes connected to the shear induced order transitions it is of exceptional importance to find an order parameter which is able to identify and quantify these changes. As it was shown in [124] and also will be confirmed in this thesis later on, under applied conditions (e.g., confinement and high density) the investigated system arranges itself into layers oriented normal to the confinement axis. As a consequence the knowledge about the two dimensional inplane order is sufficient for the characterization of the whole system. The function which meets our requirements providing the desired information about structural changes within the layers is the two dimensional local bond angle order parameter (translational order parameter)

$$\psi_n = \left\langle \frac{1}{N^{layer}} \sum_{i=1}^{N^{layer}} \frac{1}{N_i^b} \left| \sum_{j=1}^{N_i^b} \exp(in\theta_j) \right| \right\rangle. \quad (2.66)$$

In Eq. (2.66) N_i^b denotes the number of neighboring particles of the particle i within the considered layer. This value can be calculated since it is possible to extract the distance to the nearest neighbors from the first peak in the radial distribution function $g(r)$ discussed in the previous section [see Sec. 2.64b]. Furthermore, the value N^{layer} in Eq. (2.66) denotes the total number of particles within the layer and θ_j is the bond angle between the arbitrary in-plane axis (in our case x -axis) and the two dimensional vector \mathbf{r}_{ij} . The parameter n adjusts the bond angle order ψ_n to the symmetry of interest. In the current study we will restrict our attention to $n = 4$ and $n = 6$ which correspond to square and hexagonal symmetry, respectively. From the definition of the local bond angle order parameter follows that the perfect square lattice is determined by $\psi_4 = 1$ and $\psi_6 = 0$ whereas for the perfect hexagonal state $\psi_4 = 0$ and $\psi_6 = 1$ holds. For more details concerning the calculation of ψ_n the Sec. A.1 can be inspected. In the following we will define a state as square or hexagonal if the corresponding order parameter will exceed the threshold value of $\psi_n = 0.7$.

2.4.4 Pressure tensor

To derive the definition of the pressure tensor it is advisable to start with the momentum balance. The rate of change of the total momentum within the arbitrary volume V reads

$$\frac{d\mathbf{G}}{dt} = \int_V d\mathbf{r} \frac{\partial[\rho(\mathbf{r}, t)\mathbf{u}(\mathbf{r}, t)]}{\partial t}, \quad (2.67)$$

where $\mathbf{G}(t)$ denotes the total momentum within the volume V . Furthermore, the total momentum change in V can be described via the combination of three different contributions given by

$$\frac{d\mathbf{G}}{dt} = - \int_S d\mathbf{S} \rho(\mathbf{r}, t)\mathbf{u}(\mathbf{r}, t)\mathbf{u}(\mathbf{r}, t) - \int_S d\mathbf{S} \mathbf{P} + \int_V d\mathbf{r} n(\mathbf{r}, t)\mathbf{F}_e. \quad (2.68)$$

Then applying the divergence theorem to Eq. (2.68) and equating the right hand sides of Eq. (2.67) and Eq. (2.68) results in

$$\int_V d\mathbf{r} \frac{\partial[\rho(\mathbf{r}, t)\mathbf{u}(\mathbf{r}, t)]}{\partial t} = - \int_V d\mathbf{r} \left(\frac{\partial}{\partial \mathbf{r}} [\rho(\mathbf{r}, t)\mathbf{u}(\mathbf{r}, t)\mathbf{u}(\mathbf{r}, t) + \mathbf{P}] - n(\mathbf{r}, t)\mathbf{F}_e \right). \quad (2.69)$$

Since we expect Eq. (2.69) to be satisfied for an arbitrary V it can be followed that

$$\frac{\partial[\rho(\mathbf{r}, t)\mathbf{u}(\mathbf{r}, t)]}{\partial t} = - \frac{\partial}{\partial \mathbf{r}} [\rho(\mathbf{r}, t)\mathbf{u}(\mathbf{r}, t)\mathbf{u}(\mathbf{r}, t) + \mathbf{P}] + n(\mathbf{r}, t)\mathbf{F}_e \quad (2.70)$$

holds.

Now after the preparatory part of this section was finished it is time to reintroduce the system properties from the microscopic point of view starting with the definition of the density which reads

$$\rho(\mathbf{r}, t) = \sum_i m_i \delta(\mathbf{r} - \mathbf{r}_i). \quad (2.71)$$

Moreover, the instantaneous momentum density is described by

$$\rho(\mathbf{r}, t)\mathbf{u}(\mathbf{r}, t) = \sum_i m_i \dot{\mathbf{r}}_i \delta(\mathbf{r} - \mathbf{r}_i). \quad (2.72)$$

Note, that the contribution of the streaming velocity $\mathbf{u}(\mathbf{r}, t)$ considered in Eq. (2.72) is only one of two parts of the laboratory velocity which complete form is given by

$$\dot{\mathbf{r}}_i = \mathbf{v}_i + \mathbf{u}(\mathbf{r}, t). \quad (2.73)$$

The first part of the latter equation stands for the thermal velocity of particles and does not contribute to the momentum current, from which it follows that the

equation

$$\sum_i m_i \mathbf{v}_i \delta(\mathbf{r} - \mathbf{r}_i) = 0 \quad (2.74)$$

must be fulfilled. Next, we calculate the time derivative of the momentum density in Eq. (2.72) and yield

$$\frac{\partial}{\partial t} \rho(\mathbf{r}, t) \mathbf{u}(\mathbf{r}, t) = -\frac{\partial}{\partial \mathbf{r}} \sum_i m_i \dot{\mathbf{r}}_i \dot{\mathbf{r}}_i \delta(\mathbf{r} - \mathbf{r}_i) + \sum_i m_i \ddot{\mathbf{r}}_i \delta(\mathbf{r} - \mathbf{r}_i). \quad (2.75)$$

Removing the particle index from the streaming velocity by the relation

$$\mathbf{u}(\mathbf{r}_i, t) \delta(\mathbf{r} - \mathbf{r}_i) \equiv \mathbf{u}(\mathbf{r}, t) \delta(\mathbf{r} - \mathbf{r}_i), \quad (2.76)$$

and using Eq. (2.74), the first part on the right hand side of Eq. (2.75) can be rewritten as

$$-\frac{\partial}{\partial \mathbf{r}} \sum_i m_i \dot{\mathbf{r}}_i \dot{\mathbf{r}}_i \delta(\mathbf{r} - \mathbf{r}_i) = -\frac{\partial}{\partial \mathbf{r}} \left(\sum_i m_i \mathbf{v}_i \mathbf{v}_i \delta(\mathbf{r} - \mathbf{r}_i) + \rho(\mathbf{r}, t) \mathbf{u}(\mathbf{r}, t) \mathbf{u}(\mathbf{r}, t) \right). \quad (2.77)$$

The force in the second part of Eq. (2.75) can be also split into two parts which read

$$\sum_i m_i \ddot{\mathbf{r}}_i \delta(\mathbf{r} - \mathbf{r}_i) = \frac{1}{2} \sum_{i,j} \mathbf{F}_{ij} [\delta(\mathbf{r} - \mathbf{r}_i) - \delta(\mathbf{r} - \mathbf{r}_j)] + n(\mathbf{r}, t) \mathbf{F}_e, \quad (2.78)$$

where the first summand describes the force originating from the particle interaction and the second one the external force equivalent to that included in Eq. (2.69) and Eq. (2.70). Summarizing these results Eq. (2.75) can be written in the form

$$\begin{aligned} \frac{\partial}{\partial t} \rho(\mathbf{r}, t) \mathbf{u}(\mathbf{r}, t) = & -\frac{\partial}{\partial \mathbf{r}} \left(\sum_i m_i \mathbf{v}_i \mathbf{v}_i \delta(\mathbf{r} - \mathbf{r}_i) + \rho(\mathbf{r}, t) \mathbf{u}(\mathbf{r}, t) \mathbf{u}(\mathbf{r}, t) \right) \\ & + \frac{1}{2} \sum_{i,j} \mathbf{F}_{ij} [\delta(\mathbf{r} - \mathbf{r}_i) - \delta(\mathbf{r} - \mathbf{r}_j)] + n(\mathbf{r}, t) \mathbf{F}_e. \end{aligned} \quad (2.79)$$

The comparison of Eq. (2.70) with Eq. (2.79) suggests that the pressure tensor \mathbf{P} must satisfy the relation

$$-\frac{\partial}{\partial \mathbf{r}} \mathbf{P}(\mathbf{r}, t) = -\frac{\partial}{\partial \mathbf{r}} \sum_i m_i \mathbf{v}_i \mathbf{v}_i \delta(\mathbf{r} - \mathbf{r}_i) + \frac{1}{2} \sum_{i,j} \mathbf{F}_{ij} [\delta(\mathbf{r} - \mathbf{r}_i) - \delta(\mathbf{r} - \mathbf{r}_j)]. \quad (2.80)$$

Plugging the relation

$$\delta(\mathbf{r} - \mathbf{r}_i) - \delta(\mathbf{r} - \mathbf{r}_j) = -\frac{\partial}{\partial \mathbf{r}} \left(\mathbf{r}_{ji} \sum_{n=1}^{\infty} \frac{1}{n!} \left(-\mathbf{r}_{ji} \frac{\partial}{\partial \mathbf{r}} \right)^{n-1} \delta(\mathbf{r} - \mathbf{r}_j) \right), \quad (2.81)$$

into Eq. (2.80) we yield the general expression of the pressure tensor

$$\begin{aligned} \mathbf{P}(\mathbf{r}, t) = & -\sum_i m_i \mathbf{v}_i \mathbf{v}_i \delta(\mathbf{r} - \mathbf{r}_i) \\ & + \frac{1}{2} \sum_{i,j} \mathbf{F}_{ij} \left(\mathbf{r}_{ji} \sum_{n=1}^{\infty} \frac{1}{n!} \left(-\mathbf{r}_{ji} \frac{\partial}{\partial \mathbf{r}} \right)^{n-1} \delta(\mathbf{r} - \mathbf{r}_j) \right). \end{aligned} \quad (2.82)$$

When developing a model for the pressure calculation, it is assumed that particles are uniformly distributed within the system. This allows to simplify the Eq. (2.82) considering only $n = 1$ contribution which results in

$$\mathbf{P}(\mathbf{r}, t) = -\sum_i m_i \mathbf{v}_i \mathbf{v}_i \delta(\mathbf{r} - \mathbf{r}_i) + \frac{1}{2} \sum_{i,j} \mathbf{F}_{ij} \mathbf{r}_{ji} \delta(\mathbf{r} - \mathbf{r}_j). \quad (2.83)$$

Moreover, if we are interested only in the steady state pressure within the volume V and also use the relation $\mathbf{r}_{ji} = -\mathbf{r}_{ij}$ then the latter equation can be further simplified into the form which is given by

$$\mathbf{P} = -\frac{1}{V} \left(\sum_i m_i \mathbf{v}_i \mathbf{v}_i + \frac{1}{2} \sum_{i,j} \mathbf{F}_{ij} \mathbf{r}_{ij} \right) \quad (2.84)$$

$$= -\boldsymbol{\sigma}. \quad (2.85)$$

The negative of the pressure tensor in Eq. (2.85) describes the so-called stress tensor which found a broad acceptance in rheological studies [108]. Note that the microscopic description of the pressure and stress tensor presented in Eq. (2.84) and Eq. (2.85) can be directly adopted for numerical simulations. In the absence

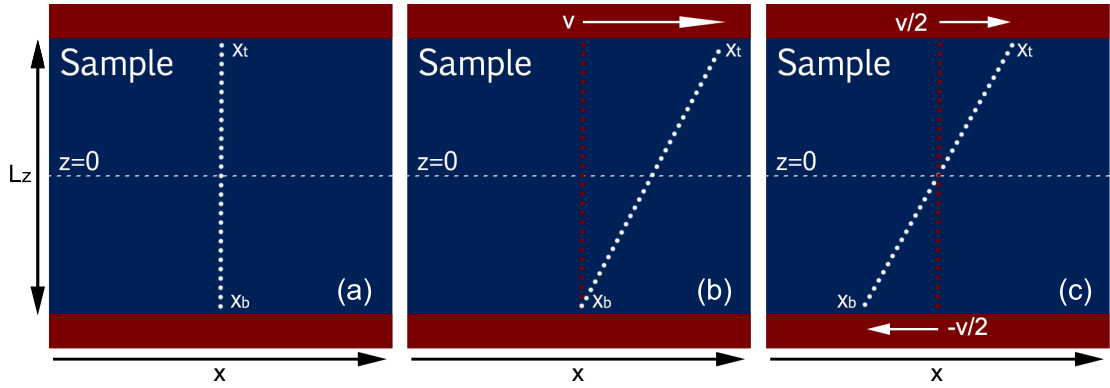


Figure 2.2: Schematic representation of a shear cell. Two parallel walls are separated by a sample of thickness L_z . The examples visualize setups without shear (a) as well as with shear induced by the motion of one (b) and two layers (c).

of shear ($\dot{\gamma} = 0$) all non-diagonal components of the pressure tensor are equal to zero and one only focuses on the diagonal contributions which provide the description of the pressure along the three spatial directions. Furthermore, it is also known that in bulk all three diagonal components of the pressure tensor are equal. However, if confinement is involved the pressure along the confinement axis generally differs from the other two components which still remain equal. Under shear ($\dot{\gamma} \neq 0$) the non-diagonal component of the stress tensor (negative pressure tensor), which connects the m -axis of the velocity gradient with the flow along n -direction, the so-called shear stress $\sigma_{mn} = \sigma_{nm}$, does not vanish. The importance of this component is in particular based on the fact that the information about the shear stress enables the calculation of the shear viscosity

$$\eta = \frac{\langle \sigma_{mn} \rangle}{\dot{\gamma}}, \quad (2.86)$$

which characterizes the response of the system to applied dynamical perturbations. This feature turns σ_{mn} into one of the key quantities in rheological studies.

2.5 Shear flow

The rheological properties of a system are of big importance for material science. In this context the term “rheology” describes the response of the system to mechanical perturbations. In solids and simple liquids the rheological properties of the system are adequately provided by elastic deformation and viscous flow, respectively. In colloidal suspensions, however, one observes behavior which shows an intermediate behavior between the simple liquid and the solid phases [142].

The common way to access the rheology of the system is to subject the sample of interest to shear. For this purpose it is usually positioned between two walls separated by a distance L_z [see Fig. (2.2a)]. The shear is induced if the relative velocity between two walls is non-zero. However, it is not decisive if only one wall moves (with the velocity v) and the other one is at rest [see Fig. (2.2b)] or the both walls are in motion (with the velocities $v/2$ and $-v/2$) [see Fig. (2.2c)]. Since both setups presented in Fig. (2.2b) and Fig. (2.2c) are equivalent for the sake of clarity in the remaining part of this section we will focus on the case visualized in Fig. (2.2c) (although in the model system discussed in the current study the shear was simulated according to the setup illustrated in Fig. (2.2c)).

The displacement of one of the walls by the distance $x_t - x_b$ induces a shear force F acting on the second fixed wall. The strength of this force is proportional to the surface area of the moving wall A and is given by

$$F = \sigma_{xz}A. \quad (2.87)$$

Note that σ_{xz} corresponds to a non-diagonal element of the stress tensor $\boldsymbol{\sigma}$ [see Eq. (2.85)]. Due to the Hooke’s law for an elastic solid σ_{xz} is proportional to the displacement $x = x_t - x_b$ divided by the sample thickness L_z . The quantity which describes this macroscopic relation via

$$\gamma = \frac{x}{L_z}, \quad (2.88)$$

is the so called shear strain. However, in contrast to solid a liquid sample transfers only transient force on the stationary wall making the macroscopic expression of the shear strain in Eq. (2.88) not appropriate [142]. Therefore, Eq. (2.88) must be represented in its differential form

$$\gamma = \frac{dx}{dz}. \quad (2.89)$$

The quantity relating the shear strain to the shear stress by the relation

$$\sigma_{xz} = G\gamma \quad (2.90)$$

is the shear modulus G . Assuming that the velocity of the moving wall $v = dx/dt$ is constant we can define the shear rate by

$$\dot{\gamma} = \frac{d}{dt} \frac{dx}{dz}, \quad (2.91)$$

which is one of the key parameters in this study. From the Eq. (2.91) follows that for simple liquids the streaming velocity (along the x -axis) must be given by

$$\mathbf{u}(\mathbf{r}, t) = \dot{\gamma}z\mathbf{e}_x. \quad (2.92)$$

However, we have already stressed that the colloidal suspensions have intermediate properties between simple liquids and solids. As a matter of fact in consequence (as already discussed in Chap. 1 and will be shown in more detail in Sec. 5.2) interactions between colloids, become more pronounced at large densities or shear rates. This leads to significant deviations between the predetermined velocity profile in Eq. (2.92) and the real one. This in turn implies that the applied shear rate $\dot{\gamma}$ and the effective shear rate $\dot{\gamma}_{eff}$ are not necessarily equal and therefore must be also distinguished.

In conclusion, it is noteworthy to mention that there are two commonly used methods to introduce shear flow in numerical simulations. First, we can simulate the moving walls explicitly using a number of rigid particle lattices at the shear cell boundaries. Moving these layers with respect to each other would shear the

intermediate sample [35]. Alternatively, one can introduce a shear-induced velocity profile $\dot{\gamma}z$ into the equation of motion [34]. This second approach was also used in our simulations [see Eq. (4.1)].

2.6 Brownian motion

The year 1827 in which the Scottish botanist Robert Brown observed a motion of pollen grains marks the birth of the concept of Brownian motion. However, the findings reported by R. Brown could be explained only decades later. First Thorvald N. Thiele in 1880 [143] and Louis Bachelier in 1900 [144] have independently proposed a mathematical description of the observed phenomenon. In the physical society the interest in the Brownian motion was sparked by Albert Einstein in 1905 [145] and Marian von Smoluchowski in 1906 [146]. They both associated the fluctuations of the pollen with collisions between the large pollen and small molecular particles in the surrounding fluid. This became an indirect probe for the existence of atoms and molecules. In 1908 the proposals concerning the equations describing the Brownian motion were verified experimentally by Jean-Baptiste Perrin [147].

Because of the very large difference between the size of the solvent molecules and the colloids, which for its part also leads to significant time scale difference, the theory of the Brownian motion became a very useful tool in the description of colloidal particles. This difference between the relaxation times of the solvent ($\approx 10^{-15}s$) and the colloids ($\approx 10^0s$) [148] enables the separation of the Newton's equation of motion in two parts.

The first part is based on the velocity of the colloid itself, as it's directed motion is slowed down by systematical collisions with the solvent particles. Due to the very large size of the colloid compared to that of the solvent molecules the deceleration of the colloid can be described by the hydrodynamical friction of a macroscopic particle. Moreover, when we assume that the velocity of the colloid is not too large, then the absolute value of the friction force γ_{fr} is directly proportional to the velocity of the colloid and can be described by the Stokes's friction coefficient

which reads

$$\gamma_{fr} = 6\pi\eta\tilde{\sigma}. \quad (2.93)$$

In Eq. (2.93) the parameter $\tilde{\sigma}$ describes the diameter of the colloid and η the shear viscosity of the solvent.

The second part of the Newton's equation is the random force $\mathbf{R}(t)$ acting on the particle due to the permanent collisions of the solvent molecules with the colloid. Summarizing all these facts the Newton's equation for the dynamics of colloidal particle in solvent can be expressed as

$$m\ddot{\mathbf{r}} = -\gamma_{fr}\dot{\mathbf{r}} + \mathbf{R}(t). \quad (2.94)$$

Since the collisions of the solvent molecules are on average undirected it can be followed that the random force in Eq. (2.94) must satisfy the condition

$$\langle \mathbf{R}(t) \rangle = \mathbf{0}. \quad (2.95)$$

Furthermore, calling the large difference in the time scales to mind, $\mathbf{R}(t)$ at two different times can be considered as uncorrelated. This condition is commonly expressed as

$$\langle \mathbf{R}(t)\mathbf{R}(t') \rangle = 2k_B T \gamma_{fr} \delta(t - t') \mathbf{I}. \quad (2.96)$$

In Eq. (2.96) the 3×3 -dimensional matrix \mathbf{I} denotes the identity matrix and $2k_B T \gamma_{fr}$ adjusts the fluctuation strength.

Being interested in time scales which are much larger than that of the colloids the momentum coordinates can be considered to be in equilibrium with the surrounding solvent. With this assumption it is possible to apply overdamped Brownian dynamics (oBD) reducing Eq. (2.94) to

$$\dot{\mathbf{r}} = \frac{\mathbf{R}(t)}{\gamma_{fr}}. \quad (2.97)$$

In the presence of additional forces \mathbf{F} acting on the colloid, the latter equation can be straightforwardly extended to

$$\dot{\mathbf{r}} = \frac{1}{\gamma_{fr}} (\mathbf{F} + \mathbf{R}(t)). \quad (2.98)$$

In this context the friction coefficient γ_{fr} can be connected to the short-time diffusion coefficient D_0 via the Einstein-Smoluchowski equation [149]

$$D_0 = \frac{k_B T}{\gamma_{fr}}. \quad (2.99)$$

Chapter 3

Simulation methods

Unlike before, nowadays the majority of open questions in physics can be hardly solved just with paper and pencil. While the analytical solution of the dynamics of two interacting bodies obeying relatively simple Newton's laws is not trivial, it is even completely impossible to track hundreds or thousands of interacting particles. Fortunately, the development of computers in the last decades enabled us to access such complex problems, with any desired precision, numerically. As a consequence a constantly increasing number of numerical studies led also to the development of algorithms and methods facilitating calculations.

In this chapter we will focus on numerical techniques which play an important role in our study.

3.1 Reduced units

Performing computer-based modeling of microscopic systems, it is convenient to non-dimensionalize system parameters using reduced instead of the real (SI) units. For this purpose, one introduces e.g., new energy, length and time units which are given by $\tilde{\epsilon}$, $\tilde{\sigma}$ and $\tilde{\tau}$, respectively. This base set of units allows the consequent representation of all other observables in the reduced system such that for instance the reduced density is given by $\rho^* = \rho\tilde{\sigma}^3$, the potential energy by $u^* = u/\tilde{\epsilon}$ and

the pressure by $\mathbf{P}^* = \mathbf{P}\tilde{\sigma}^3/\tilde{\epsilon}$.

For example the results derived for the state with $\rho^* = 0.5$ and $T^* = 0.5$ equally describe a system of Ar at 60K and the density of 840kg/m^3 as well as Xe at 112K and the density of 1617kg/m^3 [15]. The advantage of this procedure is therefore that equivalent states must be calculated only once.

Furthermore, the popularity of reduced units in numerical simulations can be also explained by the fact that all in- and output values tend to lie in the range between 10^{-3} and 10^3 in contrast to much stronger differences in the SI system [15]. Consequently the usage of reduced units increases the numerical precision and helps to minimize the risk to create over- or underflow during the calculation.

3.2 Truncated and shifted potential

In numerical simulations of multiparticle systems with short-range interaction one usually tries to make use of the fact that the interaction between the nearest neighbors is dominant compared to the relatively small contribution coming from distant particles. Therefore, in such systems it is a common practice to introduce a cutoff radius r_c , which defines the threshold distance after which the mutual interactions between the particles can be either considered as a mean field or completely neglected.

Although the choice of the cutoff radius is relatively arbitrary in simulations with periodic boundary conditions [see Sec. 3.3] the length of the simulation box defines the upper boundary, as r_c should be shorter than the half of the box length fulfilling the condition $r_c < L/2$. This condition allows to reduce the simulation time and the probability of the appearance of numerical artifacts due to the correlations arising from interactions of particles with their periodic images (finite-size effects). However, generally the value of r_c is even much smaller than the upper limit given by the latter condition. The lower limit for the cutoff radius is connected to the condition which ensures, that contributions to the potential energy originating from particles at distances with $r > r_c$ are negligible. For example, in simulations where the interaction is based on the Lennard-Jones potential given

by Eq. (2.1) the cutoff radius is usually chosen as $r_c^* \approx 2.5/\tilde{\sigma}$. This corresponds to the absolute value of potential energy of $|u_{LJ}(r_c)|^* \approx 0.016/\tilde{\epsilon}$. In setups where $r_c \ll L/2$ holds one benefits even more from the truncation of the potential energy as in such case the simulation box can be divided into subcells with the subsequent application of the *Cell lists* [see Sec. 3.4].

Note that there are two different ways to handle the contributions from particles with distances larger than r_c . In the case of simple truncation one gets the discontinuity of the interparticle potentials and consequently diverging forces at the cutoff radius. This divergence makes force calculations, indispensable in MD and BD simulations, difficult. Therefore, the latter method is generally used in MC simulations where the information about the potential energy is sufficient and no force calculations are needed. For MD and BD, it is more common to use the second method. According to this alternative approach, the truncated potential must be shifted such that the condition $u^*(r_c) = 0$ is fulfilled. Consequently, this procedure enables straightforward force calculation. The method of the truncated and shifted potential can also be extended in the sense that additionally to $u^*(r_c) = 0$ also $\mathbf{F}^*(r_c) = \mathbf{0}$ can be demanded.

3.3 Periodic boundary conditions

In numerical investigations (e.g., MC, MD and BD) of multiparticle systems the focus generally lies on the description of macroscopic processes. Although nowadays it is possible to simulate systems with up to 10^6 particles in the most cases for the sake of convenience the simulations are performed with the particle numbers ranging from 10^2 to 10^3 [15]. It is obvious that these orders of magnitude are far from thermodynamic limit. In an attempt to overcome this problem, it was suggested to introduce periodic boundary conditions in which the volume containing N particles is treated as a primitive cell of infinite periodic system [150]. In such a periodic system the reference particle i interacts with all other particles contained in the considered *periodic* system (also its own periodic images). Therefore, for a pairwise interaction between the particles the total potential energy can

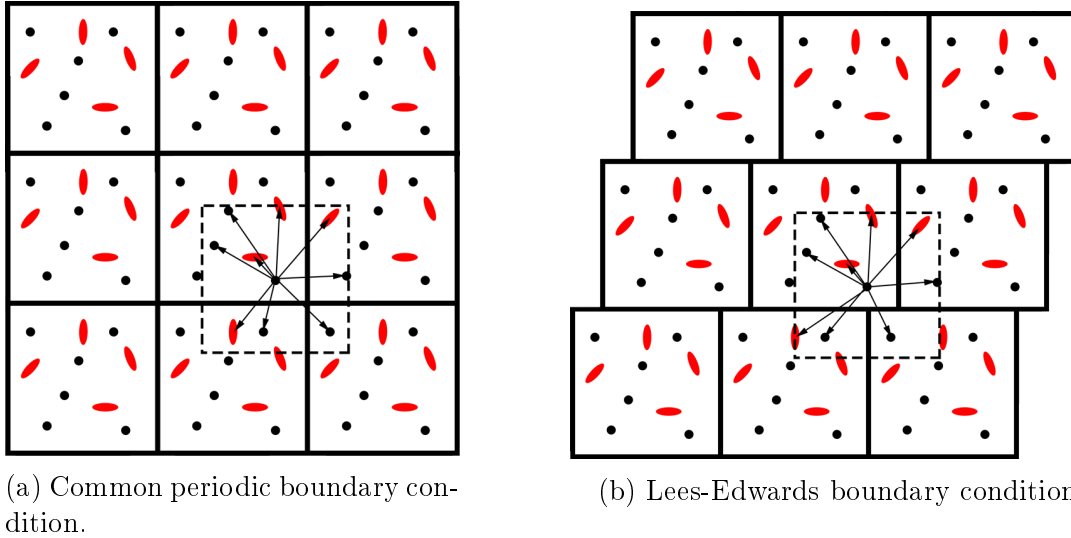


Figure 3.1: Types of periodic boundary conditions.

be expressed via

$$u_{tot} = \frac{1}{2} \sum_{i,j,\mathbf{n}} 'u(|\mathbf{r}_{ij} + \mathbf{n}L|). \quad (3.1)$$

In Eq. (3.1), L denotes the length of the periodic primitive cell and \mathbf{n} is a vector of three integer numbers. Furthermore, the prime over the sum denotes that the contribution of $i = j$ is skipped for $\mathbf{n} = \mathbf{0}$ [15]. Unfortunately the solution of one problem resulted in another one, since due to the periodicity of the boundaries the sum in Eq. (3.1) becomes infinite. For short-range interacting particles, this difficulty can be solved via truncation of the potential at the cutoff distance r_c [see Sec. 3.2], which is justified by the assumption that the contributions from distant particles are negligible. This ansatz reduces the infinite sum in Eq. (3.1) into the finite one [see Fig. (3.1a)].

Under shear, the definition of the periodic cell sketched in Fig. (3.1a) must be slightly modified. This can be explained by the fact that in sheared systems (at sufficiently small Reynolds number) the streaming velocity of the fluid and accordingly also of all simulated particles is given by Eq. (2.92). Therefore, replacing the particle which moved through the periodic cell boundaries, along the shear gradient axis, the laboratory velocity as well as the x -coordinate (along the flow direction) must be readjusted. This in turn means, that the periodic

images of the simulation cell along the velocity gradient axis cannot be static as shown in Fig. (3.1a). Taking into account all these considerations we can calculate the streaming velocity $\mathbf{u}_{n_z}(\mathbf{r}, t)$ in every periodic cell via

$$\mathbf{u}_{n_z}(\mathbf{r}, t) = (z + n_z L_z) \dot{\gamma} \mathbf{e}_x. \quad (3.2)$$

In Eq. (3.2) $n_z \in \mathbb{Z}$ is the index of the periodic simulation cell and z is the position of the particle along the shear gradient axis within the $n_z = 0$ cell. This so-called Lees-Edwards boundary condition is sketched in Fig. (3.1b).

However, all these considerations apply to the bulk. In strongly confined systems with the confinement along the z -axis (as it is the case in the current study), the width of the simulated film can become comparable to the width of the primitive cell. In such cases no periodicity along the confinement axis is necessary. Therefore, in Eq. (3.1) the condition $\mathbf{n} = (n_x, n_y, 0)^T$ with $\{n_x, n_y\} \in \mathbb{Z}$ can be demanded. The consequence of this condition is that the periodic continuation of the simulation box must be carried out only in directions perpendicular to the confinement axis. The same also applies to shear driven systems. Furthermore, if the confinement axis is equal to the axis of the shear gradient such that n_z in Eq. (3.2) has only one value $n_z = 0$, the application of Lees-Edwards boundary conditions becomes superfluous. In such case the periodicity along the confinement axis is not necessary since the two dimensional periodic boundary conditions along x - and y -axis provide sufficient framework for numerical calculations.

Although, the application of periodic boundary conditions is a very elegant way to describe the properties of a system in the thermodynamic limit, it is necessary to keep in mind that also this method has some disadvantages. First, the introduction of periodicity can induce correlations in the investigated system which do not exist in nature. In order to exclude the possibility of such correlations, it is essential to ensure that the chosen length of the primitive cell L is much larger than the cutoff radius r_c . Furthermore, it is necessary to compare the results at different L aiming to exclude the chance of the appearance of undesirable finite-size effects. Second, despite the assumption of infinitely large system the real size of the modeled cell is still dictated by the box length L . From this, it follows

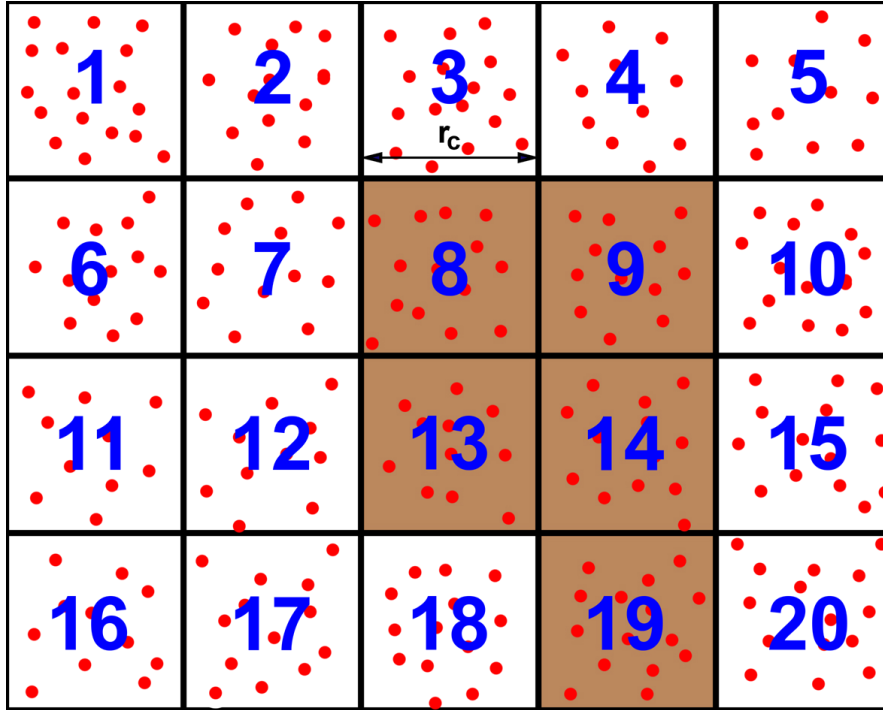


Figure 3.2: The cell list: the simulation cell is divided into cells of size $r_c \times r_c$. Each particle can interact only with particles in the same cell or neighboring cells.

that the periodic system is only able to detect fluctuations with the wavelength satisfying $\lambda \leq L$ condition.

3.4 Cell lists algorithm

The most time consuming part in numerical simulations is generally the evaluation of the force or energy contributions at each time step. This can be understood by the fact that for the calculation of the force at the particle i in systems with pair-wise additive potentials the interaction with all other particles must be considered. Thus, the time which is necessary for one time step scales with $N(N-1)/2$ where N denotes the particle number in the system. However, fortunately in systems with short-range interaction the application of various numerical techniques such as *Verlet lists* and *Cell lists* [15] allows the reduction of the simulation time.

The Cell lists method which can be conveniently applied with truncated potentials was also used to facilitate the simulation in the current study. The method is

illustrated for a two dimensional system in Fig. (3.2). In this example, the simulation box of width L is split into subcells. The width of each subcell L_s is equal or slightly larger than the cutoff radius of the truncated potential r_c . Since $L_s \geq r_c$ holds, the calculation of the interparticle potential energy (or force) can be performed by the consideration of particles in the same as well as the neighbor cells. For instance, in order to calculate the potential energy of the particle positioned in the subcell 13 [see Fig. (3.2)] one has to consider its interaction with particles positioned within the subcells 8, 9, 13, 14, and 19. The interaction with particles in 1, 2, 3, 4, 5, 6, 7, 10, 11, 12, 15, 16, 17, 18 and 20 can in turn be neglected [see Fig. (3.2)]. The allocation of particles in subcells is proportional to the particle number N and the number of subcells depends only on the cutoff radius r_c as well as the width of the simulation box L . Therefore, the overall simulation time is reduced by this method to the time step length which is proportional to N [15]. Under confinement, the particle distribution along the confinement axis (z -axis) is limited. If the width of the investigated film is comparable to the cutoff radius, it is reasonable to split the subcells in two rather than three dimensional space (equivalent to the periodic boundary conditions), which would correspond to the pattern presented in Fig. (3.2).

Chapter 4

Model

Once all the necessary background information concerning crucial theoretical approaches and numerical methods has been gathered we are now ready to focus our full attention on the investigated model system.

4.1 General setup

In this thesis, we address processes taking place in strongly confined, sheared colloidal suspensions. As discussed in Sec. 2.6, the separation of length and time scales between large colloids and much smaller solvent molecules enables an implicit description of the solvent employing overdamped Brownian dynamics simulations. Numerically the oBD of a single colloid which is based on Eq. (2.98) can be evaluated using an algorithm suggested by Ermak [151]. In this framework, the equation of motion reads

$$\mathbf{r}_i(t + \delta t) = \mathbf{r}_i(t) + \frac{D_0}{k_B T} \mathbf{F}_i(t) \delta t + \delta \mathbf{R}_i + \dot{\gamma} z_i(t) \delta t \mathbf{e}_x, \quad (4.1)$$

where $\mathbf{r}_i(t) = (x_i(t), y_i(t), z_i(t))^T$ describes the position of the i -th particle at time t and D_0 is the short time diffusion coefficient. Note that in Eq. (4.1) the influence of the solvent on each colloidal particle is not considered explicitly

but rather mimicked by the friction constant γ_{fr} [see Eq. (2.98)] and a random Gaussian displacement $\delta\mathbf{R}_i$. The displacement $\delta\mathbf{R}_i$ has zero mean and variance $2D_0\delta t$ for each cartesian component [see Sec. 2.6]. Moreover, in Eq. (4.1) we make use of the fact that the Einstein-Smoluchowski equation [see Eq. (2.99)] enables the replacement of the inverse friction constant $1/\gamma_{fr}$ by $D_0/k_B T$. The quantity $\mathbf{F}_i(t)$ in Eq. (4.1) which summarizes conservative forces acting on the particle i is familiar from Eq. (2.98). In our model this force is composed of the pair interaction potential between particles

$$u_{FF}(r) = u_{DLVO}(r) + u_{SS}(r) \quad (4.2a)$$

$$= W \frac{\exp(-\kappa r)}{r} + \tilde{\epsilon} \left(\frac{\tilde{\sigma}}{r} \right)^{12} \quad (4.2b)$$

as well as the repulsive interaction between the particles and confining walls defined in Eq. (2.3b). The interaction potentials in Eq. (4.2b) denote the DLVO and soft-sphere potentials presented in Eq. (2.51) and Eq. (2.55), respectively. Furthermore, it should be emphasized that the last summand in Eq. (4.1) namely $\dot{\gamma} z_i(t) \delta t \mathbf{e}_x$ which is not included in Eq. (2.98) was introduced in order to ensure the presence of the linear shear profile within the simulation box [see Sec. 2.5]. At this point it is important to underline that although explicit simulation of the moving walls is skipped the application of the Couette shear profile in Eq. (4.1) is a common approximation also employed in other recent numerical studies of sheared colloidal systems (see e.g., Refs. [34, 64]). From Eq. (4.1) it follows that x -, y - and z -axis denote the flow, vorticity and gradient directions, respectively. Finally, it should be noted that the definition of the shear flow in Eq. (4.1) implies that the zero-velocity plane is positioned at $z=0$ [see Fig. (4.1)].

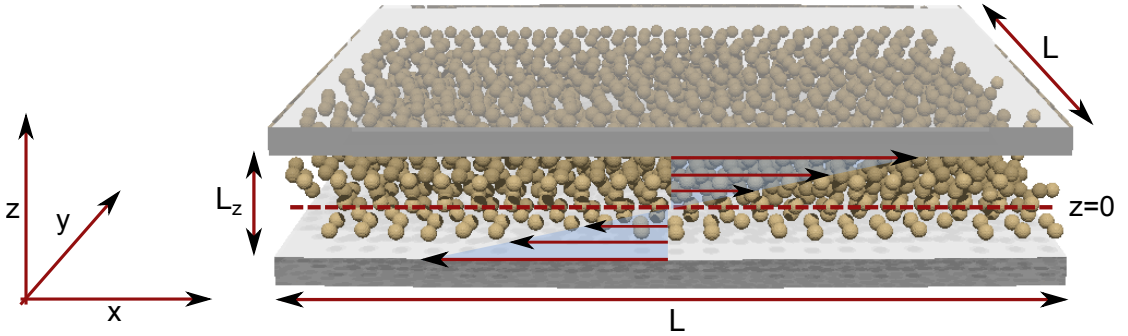


Figure 4.1: Definition of the coordinate system and schematic illustration of the shear cell. The dashed line indicates the zero-velocity plane, which is positioned at $z=0$.

4.2 Truncation of interparticle potentials

The consequence of our parameter choice (which will be discussed in detail in the next section) is that the fluid-fluid interaction in $u_{FF}(r)$ is short-ranged. Therefore, the computation can be accelerated by applying truncation technique discussed in Sec. 3.2. Truncating the potential in the framework of oBD it is also necessary to eliminate the appearing discontinuity of this function at the cutoff radius. Thus, we shift the total pair interaction potential in Eq. (4.2b) and demand that $u_{FF}(r_c) = 0$ as well as $\mathbf{F}_{FF}(r_c) = \mathbf{0}$ must hold. Note that the condition $\mathbf{F}_{FF}(r_c) = \mathbf{0}$ also ensures that not only the potential but also the force is a continuous function of the interparticle distance r . These conditions are satisfied by the truncated and shifted total pair interaction potential which reads

$$\begin{aligned}
 u_{FFS}(r) = & W \left[\frac{\exp(-\kappa r)}{r} - \frac{\exp(-\kappa r_c)}{r_c} \right] + 4\tilde{\epsilon} \left[\left(\frac{\tilde{\sigma}}{r} \right)^{12} - \left(\frac{\tilde{\sigma}}{r_c} \right)^{12} \right] \\
 & + (r - r_c) \left[W \exp(-\kappa r_c) \left(\frac{\kappa}{r_c} + \frac{1}{r_c^2} \right) + 48\tilde{\epsilon} \left(\frac{\tilde{\sigma}}{r_c} \right)^{13} \right]. \quad (4.3)
 \end{aligned}$$

The choice of the cutoff radius r_c was based on experiences with the Lennard-Jones potential which is usually truncated at $r_c = 2.5\tilde{\sigma}$ [152, 153]. This implies that the contributions to the potential energy which are smaller than $|u_{LJ}(2.5)|$ are neglected. Making use of this information we rounded up the cutoff radius from $2.5\tilde{\sigma}$ to $3.0\tilde{\sigma}$ ensuring that the contribution from the interparticle interaction neglected in our study is even smaller than that of comparable Lennard-Jones models. Therefore in our model r_c was chosen such that it had to fulfill the condition $u_{FFS}(r_c) \leq u_{LJ}(3.0\tilde{\sigma})$. The resulting cutoff radius $r_c = 2.97\tilde{\sigma}$ is used as the truncation threshold in all following discussions.

4.3 Model parameters

Using Eq. (4.3) for the calculation of the fluid-fluid interaction the parameters for the DLVO interaction [see Eq. (2.51)] were set in accordance with the experimental setups in [125, 127] to $Z=35$, $\tilde{\sigma}=26$ nm, $T=298$ K, $\epsilon=78.5$ and $I=10^{-5}$ mol/l. These parameters determine the dimensionless prefactor of the Yukawa potential, $W^*=W/(\tilde{\epsilon}\tilde{\sigma})$, and the inverse Debye screening length $\kappa^*=\kappa\tilde{\sigma}$ via Eq. (2.52) and Eq. (2.54). In the present study we have chosen the reduced density $\rho^* = 0.85$, yielding $W^* \approx 123.4$ and $\kappa^* \approx 3.22$. In using DLVO theory we have to keep in mind that the standard DLVO potential introduced in Eq. (2.51) pertains to a bulk system, where each macroion is surrounded by a spherical cloud of counterions. Here, we are considering strongly confined systems where the counterion clouds are distorted. Nevertheless, as was shown in previous investigations [125, 127], the bulk DLVO theory yields a good description at least of structural phenomena such as layering. This can be explained by the fact that, at the conditions considered ($\kappa^*=3.22$), the thickness of the screening layer κ^{-1} is small compared to the colloidal diameter $\tilde{\sigma}$. As a consequence, the deformation of the counterion clouds is only a minor effect and can be neglected. Finally, to mimic a slit-pore geometry, the colloidal particles are confined by two soft plane-parallel walls of infinite extent in the xy -plane and located at $z=\pm L_z/2$ [see Eq. (2.3b)] as shown in Fig. (4.1). While the energy scale was chosen to be $\tilde{\epsilon} = k_B T$ the time scale of the system

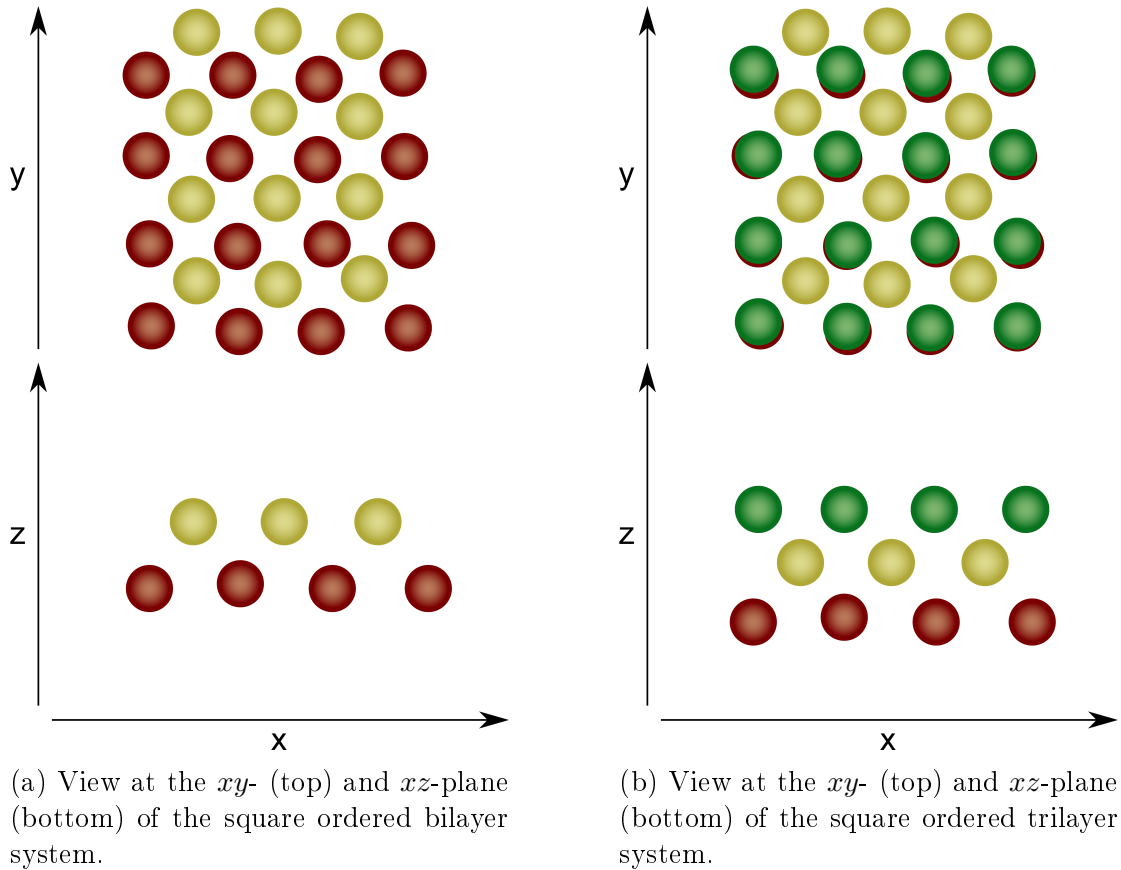


Figure 4.2: Sketch of equilibrium configurations for the bi- and trilayer film.

was set to $\tilde{\tau} = \tilde{\sigma}^2 / D_0$, which defines the so-called Brownian time. The time step was set to $\delta t = 10^{-5} \tilde{\tau}$. In preceding Monte-Carlo simulations Grandner *et al.* [124] have shown that at system parameters presented above and the wall separation of $L_z \approx 2.2\tilde{\sigma}$ and $L_z \approx 3.2\tilde{\sigma}$, the confined colloidal suspension tends to align in a two and three square ordered layers, respectively. All simulations in the present work will be started from these two initial configurations, which are illustrated in Fig. (4.2a) and Fig. (4.2b). Setting the width of the simulation box to $L \approx 23.8\tilde{\sigma}$ for the bilayer system its size was slightly increased to $L \approx 24.2\tilde{\sigma}$ in the trilayer case. Since the calculations in both cases were carried out at constant reduced density $\rho^* = 0.85$, the number of 1058 particles used for $L_z = 2.2\tilde{\sigma}$ (bilayer) had also to be increased to 1587 for $L_z = 3.2\tilde{\sigma}$ (trilayer). The simulation box of the volume $V = L \times L \times L_z$ was periodically continued along the flow (x) and vorticity (y) direction [see Sec. 3.3]. Starting with configurations sketched in Fig. (4.2a) and Fig. (4.2b) both systems were equilibrated for 10^7 steps (i.e., $100\tilde{\tau}$). Then the

shear force was switched on. After the shearing was started, the simulation was carried out for an additional period of 100τ . During this time the steady state was reached. Only after these preparations the actual analysis has been performed.

Chapter 5

Confined colloidal bilayer in a planar shear flow

As mentioned before the current thesis is devoted to the impact of shear in strongly confined colloidal suspension. Therefore, we present detailed overdamped Brownian dynamics simulation [see Eq. (4.1)] study of a system of charged colloidal spheres under the combined influence of strong spatial confinement, as realized by two plane-parallel, smooth walls [see Eq. (2.3b)], and planar, steady shear flow [see Eq. (4.1)]. In this section we focus on a system composed of only two layers of particles between the confining plates (bilayers). The corresponding set of parameters was introduced in Sec. 4.3

The choice of the interparticle interaction [see Eq. (4.2b)] was motivated by recent studies which showed a very good accordance between numerical and experimental results [125, 127].

The zero-shear (equilibrium) structure is characterized by crystalline in-plane order with square-like symmetry visualized in Fig. (4.2a). Starting from this initial configuration the influence of shear on the dynamical and structural features of the system were explored.

5.1 Shear-induced structural changes

As a first step, we calculated the density profile along the z -direction according Eq. (2.58). Second, we have focused on the translational in-plane order parameter Ψ_n defined by Eq. (2.66). Note that the distance to the next neighbors in Eq. (2.66) is extracted from the intralayer radial pair distribution function given by Eq. (2.65). In the following we focus on the order parameters Ψ_4 and Ψ_6 measuring how close the system is to a perfect square ($\Psi_4=1, \Psi_6=0$) or hexagonal order ($\Psi_4=0, \Psi_6=1$), respectively. Numerical results for $\rho(z)$, $\Psi_{4/6}$ and $g(r)$ are plotted in Fig. (5.2), Fig. (5.3) and Fig. (5.4), respectively. For their interpretation, it is instructive to inspect additionally the simulation “snapshots” at different shear rates shown in [see Fig. (5.1a – d)]. From these snapshots and the plots of Ψ_n we find that there are three different structural regimes. At small shear rates ($\dot{\gamma}\tilde{\tau} \leq 220$) the system retains in-plane crystalline order with square symmetry. Indeed, as seen from Fig. (5.3), the order parameter Ψ_4 is close to 1 throughout this range of

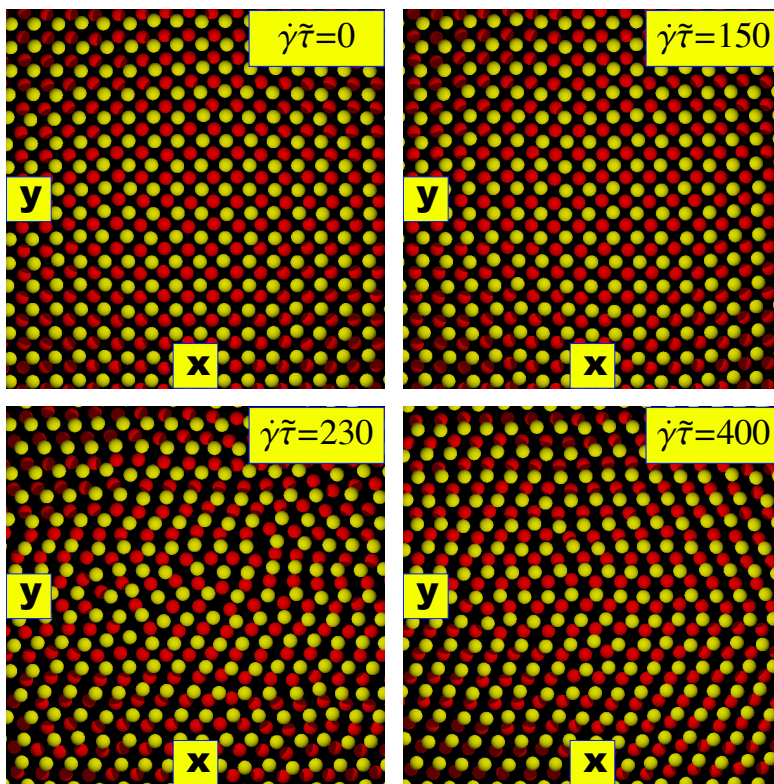


Figure 5.1: Simulation snapshots at $\rho^*=0.85$ and $L_z=2.2\tilde{\sigma}$ for different shear rates. The yellow (red) circles represent particles of the upper (lower) layer.

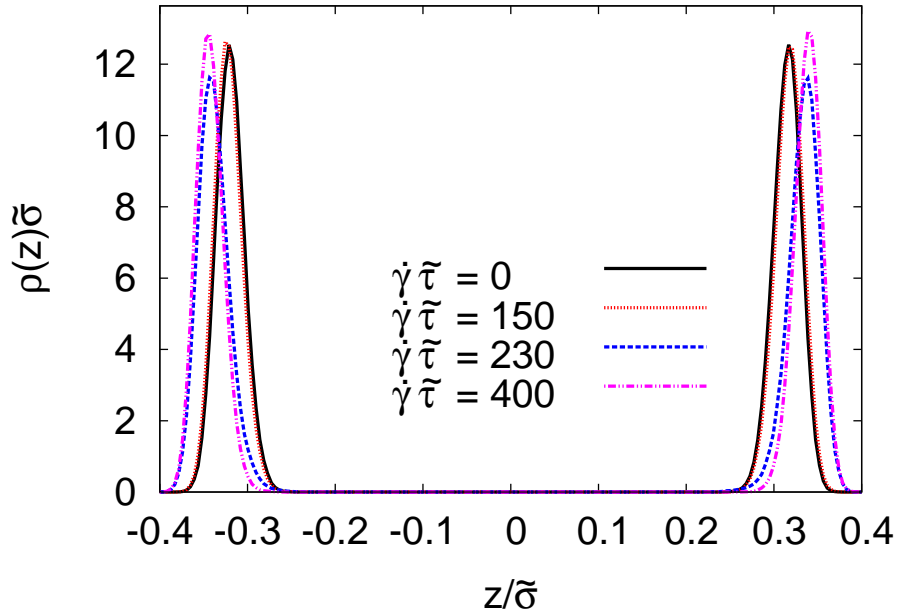


Figure 5.2: Density profiles in the shear gradient (and confinement) direction for different shear rates.

shear rates. In the subsequent, relatively small regime ($230 \leq \dot{\gamma}\tilde{\tau} \leq 250$) the intralayer structure becomes disordered [see Fig. (5.1c)], and the system can be considered as shear-molten. Finally, at ($\dot{\gamma}\tilde{\tau} \geq 260$) the system displays a reentrant crystallization into a state with hexagonal symmetry. This is characterized by an increase of the hexagonal order parameter Ψ_6 above the threshold value 0.7 [see Fig. (5.3)]. The shear-induced structural changes are also reflected by the density profile [see Fig. (5.2)]. At small shear rates, at which the system persists in the square crystalline state the layers remain to have the same distance with respect to each other (as inferred from the location of the density peaks) as at $\dot{\gamma}\tilde{\tau}=0$. But entering the shear-molten state, the distance between two layers slightly increases. This can be explained by the fact that the shear force now yields a net motion of the layers [see Sec. 5.2], while at the same time, particles can now escape their lattice positions. This induces an effective repulsion between the layers, which the system compensates by accepting a smaller distance between the layers and the confining walls. Finally, we briefly inspect the correlation function $g(r)$ plotted in Fig. (5.4). It is seen that this function displays profound changes when going from one shear regime to the next. Specially, in the range $\dot{\gamma}\tilde{\tau} \leq 220$, $g(r)$ has a well defined form corresponding to the 4-fold symmetry [see Fig. (5.4a – b)].

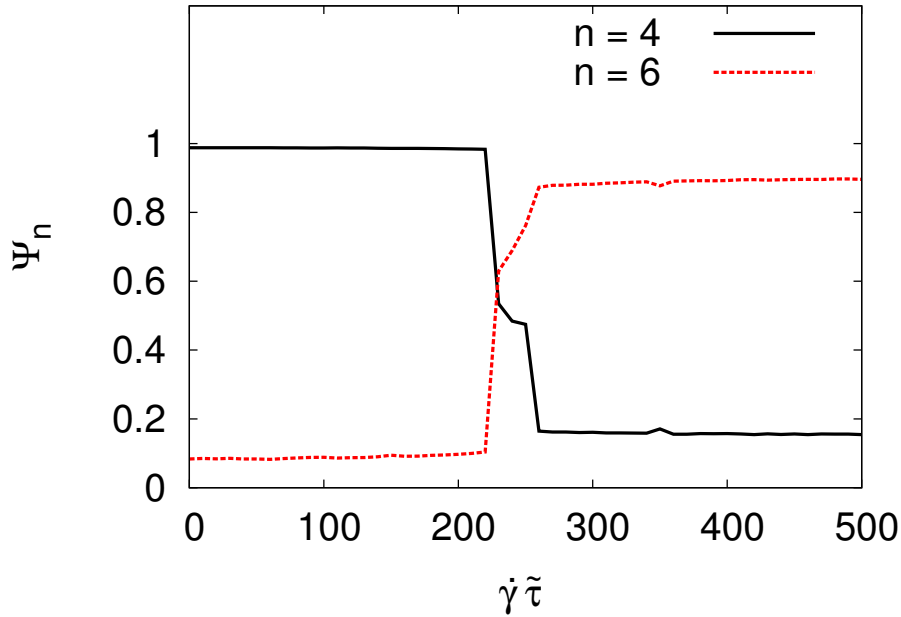
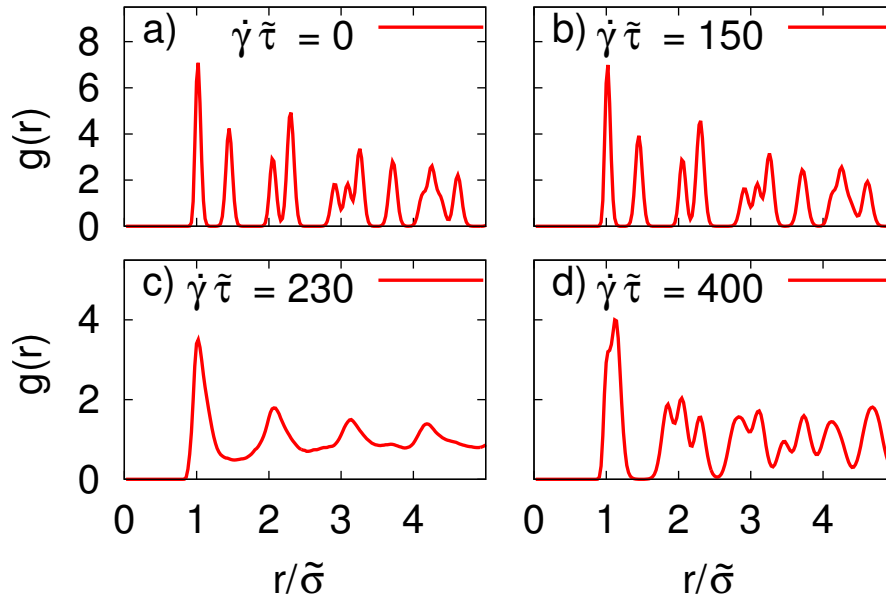


Figure 5.3: In-plane order parameter for square (Ψ_4) and hexagonal (Ψ_6) symmetry as a function of the shear rate $\dot{\gamma}$.

Entering the disordered state, the intralayer distribution function displays a liquid-like structure reflecting a loss of long-range positional correlations. At even larger shear rates $g(r)$ becomes again crystal-like, this time reflecting a 6-fold symmetry. Similar results were observed in an earlier simulation study of a colloidal bilayer under shear [34]. However, the calculations in [34] were performed at a significantly lower reduced density. This may explain why the first peak of $g(r)$ in the hexagonal state is a single peak in [34], whereas it is splitted in our study [see Fig. (5.4d)]. We interpret this splitting as an indication that the shear slightly distorts the hexagonal symmetry in very dense layers. To this end we view the hexagonal lattice as a collection of strings along the flow (i.e., x -) direction. Due to the shear and the presence of an adjacent layer [see Fig. (5.1d)], the distance between nearest neighbors in different strings along the flow (i.e., x -) direction will be slightly larger than that of nearest neighbors in the same string. It seems plausible that this effect will be partially pronounced at high densities such as the one considered in our study ($\rho^*=0.85$).

Figure 5.4: Intralayer distribution function $g(r)$ at different shear rates.

5.2 Translational dynamics

We now turn to the discussion of the dynamical properties of our bilayer system. We start by investigating the motion of one of the layers in the shear flow. To this end we calculate the position of the layers center of mass,

$$\Delta \mathbf{r}_{cm}(t) = \left\langle \frac{1}{N_l} \sum_{i=1}^{N_l} (\mathbf{r}_i(t+t') - \mathbf{r}_i(t')) \right\rangle, \quad (5.1)$$

with t' referring to the starting point of the calculation. In Fig. (5.5a) we plot results for the function $\Delta \mathbf{r}_{cm}(t)$ in flow direction. It is seen that the square-ordered structure appearing at small shear rates is characterized by zero net motion of the layers. This changes only when $\dot{\gamma}$ is increased towards values pertaining to the shear-molten state. Finally, after the reentrance of the crystalline state (with hexagonal order) we observe in Fig. (5.5a) even faster net motion of the layers. These trends are also reflected by the velocity profile defined as

$$v_x(z) = \frac{1}{N(z)} \sum_{i=1}^{N(z)} \frac{x_i(t + \Delta t) - x_i(t)}{\Delta t}, \quad (5.2)$$

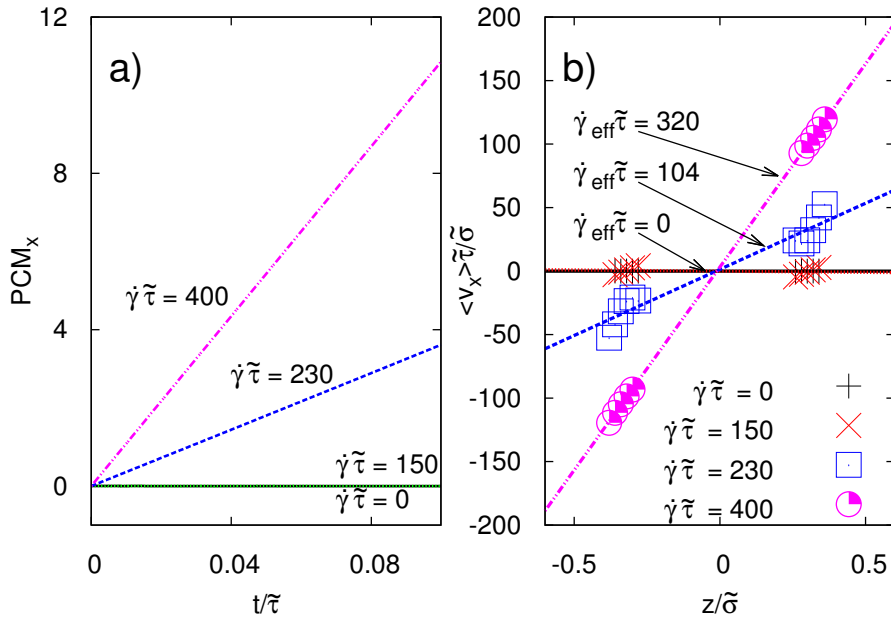


Figure 5.5: The position of the center of mass (PCM) in flow direction (a) and the velocity profile of the system (b) at different shear rates.

with $N(z)$ corresponding to the number of particles at the considered z -position. Results for $v_x(z)$ are plotted in Fig. (5.5b). The data are strongly accumulated at $z \approx \pm 0.4\tilde{\sigma}$, corresponding to the peaks in the density profile [see Fig. (5.2)]. Nevertheless, as seen in Fig. (5.5b), we can fit the data, to a reasonable degree, by linear functions, consistent with our ansatz for the imposed shear flow in Eq. (4.1). Some deviation from linearity occurs in the molten state, where we observe an increase of the velocity very close to the walls. We recall that the particles in the molten state are not caged within a lattice, but can rather move like in a fluid. In this situation, a particle close to the wall feels less friction than a particle in the middle region, resulting in a somewhat larger velocity. As expected, the slope of these fitted linear profiles, $\dot{\gamma}_{eff}$, turns out to be different from the externally imposed value $\dot{\gamma}$. In order to understand the deviation between the applied and the effective shear rate we have plotted the effective shear rate $\dot{\gamma}_{eff}$ as a function of the applied shear rate $\dot{\gamma}$. The results are plotted in Fig. (5.6). Indeed $\dot{\gamma}_{eff}\tilde{\tau} \approx 0$ in the square-ordered regime ($\dot{\gamma}\tilde{\tau} \leq 220$), reflecting the zero net motion of the particles. Entering into the shear molten state we observe a jump of the $\dot{\gamma}_{eff}$. This behavior is not surprising because entering into the molten state the layers start to move with respect to each other. The system loses its order and becomes nonlinear until the

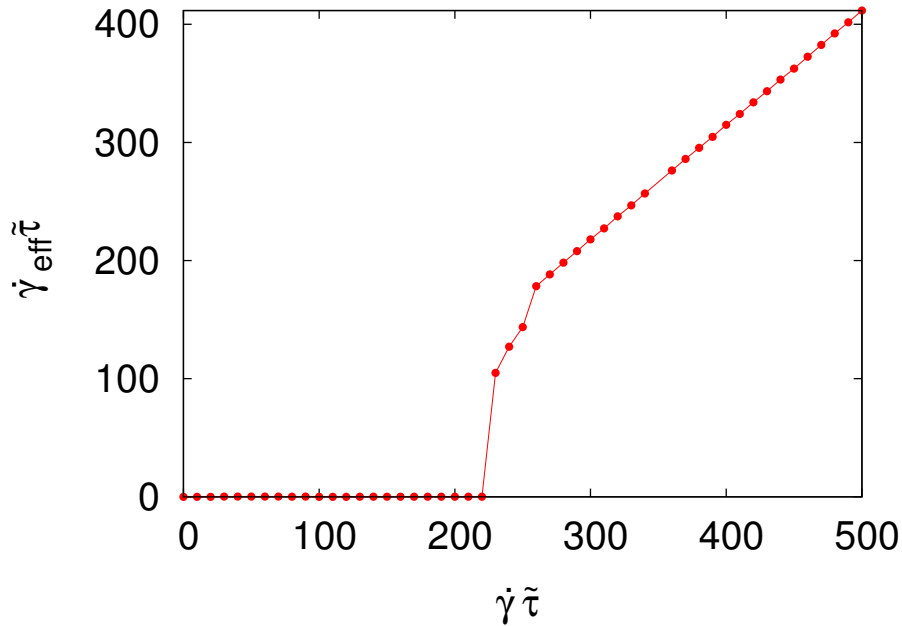


Figure 5.6: Effective shear rate (as determined from the velocity profile) as a function of the shear rate $\dot{\gamma}$.

recrystallization into the hexagonal state, where the $\dot{\gamma}_{eff}$ enters in a linear regime again. Similar behavior has been recently observed in systems of Yukawa-particles driven over a substrate [154]. In the shear-molten and hexagonal state, we find $\dot{\gamma}_{eff} \tilde{\tau} > 0$, but with values which are significantly lower than $\dot{\gamma}$. We conclude that the increased effective repulsive interaction stemming from the mutual velocities of the adjacent layers leads to an increase of the interlayer distance [see Fig. (5.2)]. Next, we consider the relative mean squared displacement (MSD) of particles within the layers. This function corresponds to the usual MSD corrected by the motion of the center of mass. Specifically,

$$\Delta \mathbf{r}^2(t) = \left\langle \frac{1}{N_l} \sum_{i=1}^{N_l} (\mathbf{r}_i(t+t') - \mathbf{r}_i(t') - \Delta \mathbf{r}_{cm}(t))^2 \right\rangle. \quad (5.3)$$

By considering the relative MSD we can directly compare the mobility in the hexagonal and shear-molten state, where the entire layers move, with the mobility in the square-ordered state, where there is no such motion. Results for the components of the relative MSD in flow and vorticity direction are shown in Fig. (5.7). At zero shear rate, both MSD components approach a plateau at long times, reflecting the (persistent) trapping of the particles at the sites of the square lattice.

With the onset of the shear flow (small shear rates) this behavior at first persists. In fact, the y -component does indicate a small degree of mobility, but the entire behavior remains subdiffusive (i.e. $\text{MSD} \propto t^\alpha$ with $\alpha < 1$) for the whole time range investigated. An appreciable in-plane mobility is only observed in the shear-molten state. Here, the particles escape their lattice positions and start to diffuse along both, the flow and the vorticity direction. The resulting non-trivial time dependence of the MSD will be analyzed in detail in Sec. 5.3. Upon further increase of $\dot{\gamma}$ we find from Fig. (5.7a) that the MSD in flow direction develops a new plateau, thus indicating the reentrance of crystalline (this time, hexagonal) ordering within the still-moving layers. The emergence of a plateau at long times is also visible in the MSD in vorticity (i.e., y -) direction.

5.3 Diffusion in the shear-molten state

In this section we attempt to describe the translational dynamics within the shear-molten state in an analytical fashion. The key ingredient is the fact that, although the lateral structure within this state is liquid-like, the particles are still essentially trapped in their layers. Here we approximate this confinement by a harmonic potential acting on each particle in z -direction, i.e. the shear gradient direction. We also assume that the confinement into the layers already represents the most important many-particle effect in our system. In other words, after introducing the (harmonic) confinement we consider the particles as independent. The corresponding equations of motion read

$$\dot{x}(t) = \dot{\gamma}z(t) + \sqrt{2D_x}R_x(t) \quad (5.4a)$$

$$\dot{y}(t) = \sqrt{2D_y}R_y(t) \quad (5.4b)$$

$$\dot{z}(t) = -\frac{D_z\omega}{k_B T}(z(t) - z_0) + \sqrt{2D_z}R_z(t) \quad (5.4c)$$

with $\langle R_i(t) \rangle = 0$ and $\langle R_i(t)R_j(t') \rangle = \delta_{ij}\delta(t - t')$. The harmonic trap enters into Eq. (5.4c), with ω playing the role of a spring constant. Similar equations have

been recently derived and analyzed in [155, 156]. Solving Eq. (5.4) we obtain

$$x(t) = x_0 + \int_0^t \left(\dot{\gamma}z(t') + \sqrt{2D_x}R_x(t') \right) dt', \quad (5.5a)$$

$$y(t) = y_0 + \sqrt{2D_y} \int_0^t R_y(t') dt', \quad (5.5b)$$

$$z(t) = z_0 + \sqrt{2D_z} \exp\left(-\frac{D_z\omega}{k_B T}t\right) \int_0^t \exp\left(\frac{D_z\omega}{k_B T}t'\right) R_z(t') dt'. \quad (5.5c)$$

From Eq. (5.5) we can calculate the MSDs in the flow direction,

$$\begin{aligned} \langle (x(t) - x_0)^2 \rangle &= \sqrt{2D_x} \left\langle \int_0^t \left(\frac{\dot{\gamma}z(t')}{\sqrt{2D_x}} + R_x(t') \right) dt' \int_0^t \left(\frac{\dot{\gamma}z(t'')}{\sqrt{2D_x}} + R_x(t'') \right) dt'' \right\rangle \\ &= 2D_x t + \int_0^t \int_0^t \dot{\gamma}^2 \langle z(t')z(t'') \rangle dt' dt'' \end{aligned} \quad (5.6a)$$

$$\begin{aligned} &= 2D_x t + \dot{\gamma}^2 z_0^2 t^2 - \\ &\quad \frac{\dot{\gamma}^2 k_B^3 T^3}{D_z^2 \omega^3} \left(3 + \exp\left(-\frac{2D_z\omega t}{k_B T}\right) - 4 \exp\left(-\frac{D_z\omega t}{k_B T}\right) - \frac{2D_z\omega t}{k_B T} \right) \end{aligned} \quad (5.6b)$$

$$\begin{aligned} &= 2D_x t + \dot{\gamma}^2 z_0^2 t^2 + \frac{2D_z \dot{\gamma}^2 t^3}{3} + \\ &\quad \dot{\gamma}^2 D_z \left(\sum_{n=4}^{\infty} \frac{2^n t^n}{n!} \left(-\frac{D_z\omega}{k_B T}\right)^{n-3} - 4 \sum_{n=4}^{\infty} \frac{t^n}{n!} \left(-\frac{D_z\omega}{k_B T}\right)^{n-3} \right) \end{aligned} \quad (5.6c)$$

and vorticity direction,

$$\langle (y(t) - y_0)^2 \rangle = 2D_y \left\langle \int_0^t R_y(t') dt' \int_0^t R_y(t'') dt'' \right\rangle \quad (5.7a)$$

$$= 2D_y t. \quad (5.7b)$$

Inspecting Eq. (5.6) and Eq. (5.7) we see that, within our idealized model, the MSD in vorticity direction displays normal diffusive behavior $\propto t$. Regarding the MSD in flow direction, the first and the second term on the right side of Eq. (5.6c) represent contributions from the free diffusion and the net motion of the entire layer (with velocity $\dot{\gamma}z_0$), respectively. The third term $\propto t^3$ also appears when one considers a free particle under shear flow [157]. It results from the diffusion of the particle along the velocity gradient. The last terms stem from the interplay of the harmonic confinement and the shear flow. Indeed, one finds that for $\omega \rightarrow 0$ the

MSD reduces to that for a free particle in shear flow.

To compare these analytical predictions with our simulation results, we set $k_B T = \tilde{\epsilon}$, $z_0 = \pm 0.341\tilde{\sigma}$ and $\dot{\gamma}\tilde{\tau} = 104$. The latter value corresponds to the effective shear rate at $\dot{\gamma}\tilde{\tau} = 230$ [see Fig. (5.5b)]. We then use the functions defined in Eq. (5.6c) and Eq. (5.7b) to fit the simulation data, the fitting parameters being D_x^* , D_y^* , D_z^* and ω^* . The results of this procedure are shown in Fig. (5.8a) and Fig. (5.8b), where we focus on the MSDs at long times. It turns out that the two MSDs obtained from the BD simulation can indeed be fitted nearly perfectly by the analytical expressions. Specifically, we find $D_x^* = 3.37$, $D_y^* = 0.0024$ and $D_z^* = 3.16 \times 10^{-5}$. We can easily understand that D_x^* has the largest value due to the drag of particles in the velocity direction. The very small value of D_z^* shows that the particles are strongly caged within the layer and their fluctuations in z -direction are very small. The value of D_y^* is between D_x^* and D_z^* as the particles are neither dragged nor caged in y -direction. The value obtained for the spring constant is $\omega^* = 6521$. The resulting harmonic potential is plotted in Fig. (5.8c) together with the density profile, showing that the widths of the harmonic wall describes that of the density profile very well.

Taken together, we can conclude that lateral diffusion in the shear-molten state of our confined system is indeed accurately described by the dynamics of a harmonically trapped free particle under flow.

5.4 Zig-zag motion at high shear rates

In this section we explore the appearance and characteristics of collective particle motion in our shear-driven colloidal bilayers. The presence of such collective modes is suggested by recent real-space experiments on three-dimensional colloidal crystals of Polymethylmethacrylate (PMMA) spheres under planar shear [65]. At suitable shear rates and densities, this real system consists of hexagonally ordered sliding layers, similar to what we see in our bilayer system. Investigating then the motion of individual PMMA spheres, a collective zig-zag motion into the vorticity direction (i.e., the y -direction) was observed [65]. In other words, strings of

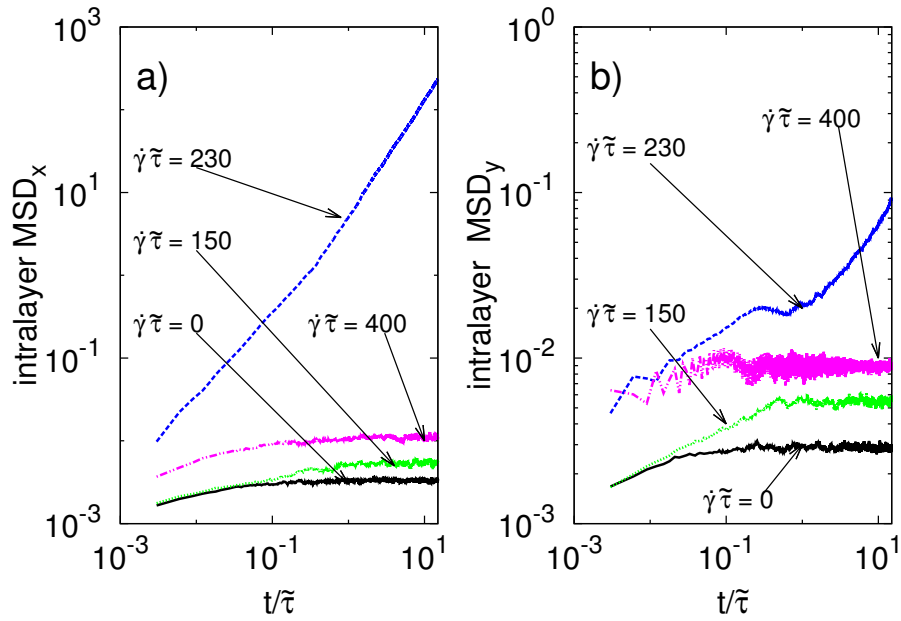


Figure 5.7: The mean squared displacements within the layer in flow (MSD_x) and vorticity (MSD_y) directions at different shear rates.

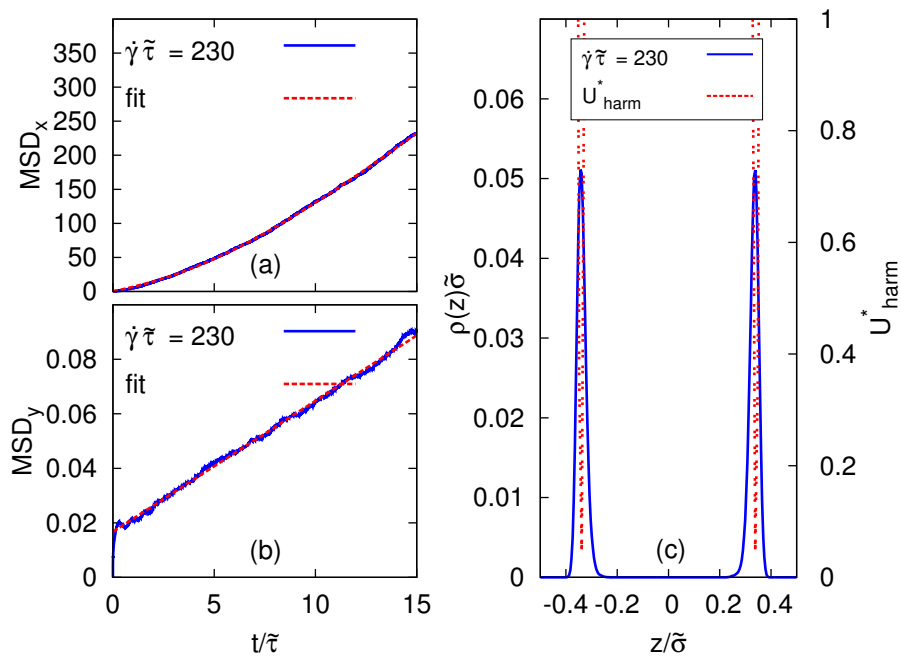


Figure 5.8: Fit of the mean squared displacements of one sheared particle in harmonic potential with the simulated system at $\dot{\gamma}\tilde{\tau} = 230$ in flow direction (a) and vorticity direction (b). From the fit resulting harmonic potential was compared with the density profile in (c). The parameters used in the fit are $D_x^* = 3.37$, $D_y^* = 0.0024$, $D_z^* = 3.16 \times 10^{-5}$ and $\omega^* = 6521$.

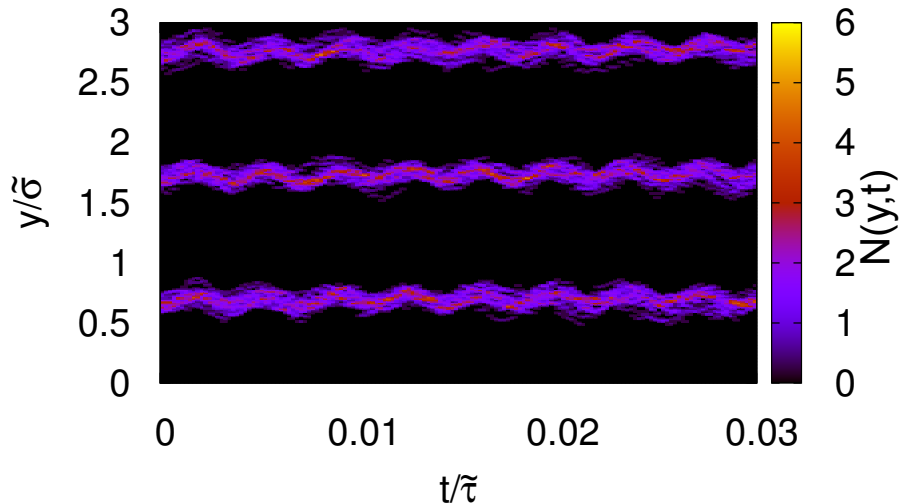


Figure 5.9: Time evolution of the number density $N(y, t)$ at $\dot{\gamma}\tilde{\tau} = 500$.

particles aligned in x -(flow) direction oscillate in phase. The microscopic origin of these oscillations can be understood when we recall the mutual arrangement of two hexagonal layers [see Fig. (5.1d)]. If these layers are moved relative to one another, each particle of one layer experiences barriers induced by the particles in the neighboring string in the adjacent layers. To circumvent these barriers the particles have to bypass and then come back, yielding effectively a zig-zag motion. We have found that the same kind of collective motion also occurs in our bilayer system. It is also noteworthy that setting the particle size $\tilde{\sigma} = 1.67\mu$ and short-time diffusion coefficient $D_0 = 0.005\tilde{\sigma}^2/s$ at a shear rate of $1s^{-1}$ corresponding to the parameters of the system investigated in [65] we find that in our study the zig-zag motion emerges at dimensionless shear rates comparable to those in [65]. To visualize the zig-zag mode we plot in Fig. (5.9) the number density of one layer in y -direction defined by

$$N(y, t) = \left\langle \sum_{i=1}^{N_i} \delta(y - y_i(t)) \right\rangle \quad (5.8)$$

as function of time (horizontal axis) and space (vertical axis). One clearly identifies the regular character of the oscillations; also, neighboring strings apparently oscillate in phase. Having in mind the microscopic origin of the oscillations, one expects their frequency to increase with the shear rate. More precisely, the relevant shear rate in this context should be not $\dot{\gamma}$ (i.e., the externally imposed

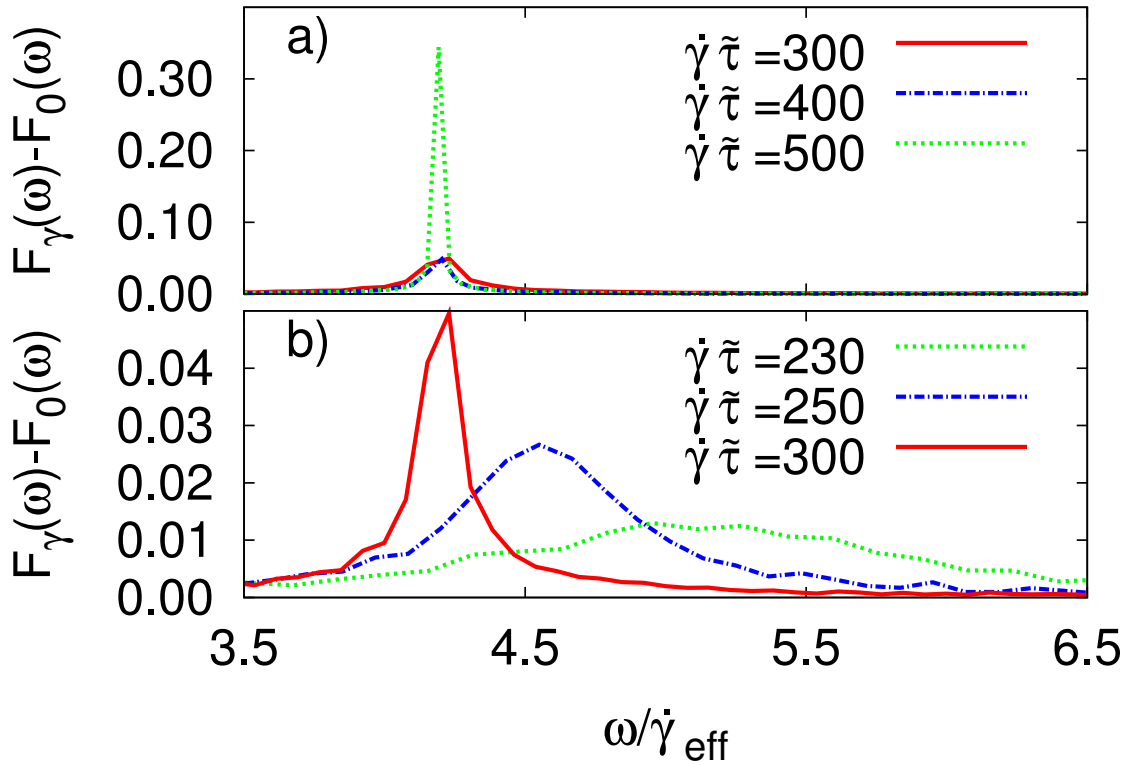


Figure 5.10: Rescaled oscillation frequencies of the zig-zag motion at different shear rates.

rate) but rather $\dot{\gamma}_{eff}$, which corresponds to the effective local shear rate already considered in Sec. 5.2 [see Fig. (5.5b)]. Indeed, in the experiments [65] it was found that the oscillation frequency ω_0 is proportional to the effective shear rate. To test this expectation in our system, we now consider the Fourier transform of the center-of-mass position of one layer as function of time,

$$F_{\dot{\gamma}}(\omega) = \left\langle \int_0^{t_{max}} \Delta y_{cm}(t) \exp(-\omega t) dt \right\rangle, \quad (5.9)$$

where $\Delta y_{cm}(t)$ describes the shift of the position of the center of mass as a function of time. Results for $F_{\dot{\gamma}}(\omega)$ at different shear rates are plotted in Fig. (5.10). Note that we have scaled the frequency (horizontal axis) by the effective shear rate, $\dot{\gamma}_{eff}$. From Fig. (5.10a) we see that, within the hexagonally ordered state ($\dot{\gamma}\tilde{\tau} \geq 300$), the functions $F_{\dot{\gamma}}(\omega)$ are essentially zero apart from one, relatively sharp peak, with its height and sharpness increasing with increasing $\dot{\gamma}$. This signals the presence of one dominant oscillation frequency, consistent with the real-time plot in Fig. (5.9). Moreover, the peaks are located at the same scaled frequency $\omega_0/\dot{\gamma}_{eff} \approx 4.19$. This

scaling is in agreement with the corresponding experimental observation [65].

For the present system, we have found that the oscillation frequency ω_0 obeys the relation

$$\frac{\omega_0}{2\pi} = \frac{\dot{\gamma}_{eff}\Delta z}{x_0}, \quad (5.10)$$

where $\Delta z = 0.69\tilde{\sigma}$ is the distance between the layers and x_0 corresponds to the in-plane distance between nearest neighbors in flow direction. From the in-plane correlations plotted in Fig. (5.4) we obtain $x_0 \approx 1.03\tilde{\sigma}$. The constancy of the ratio $\omega_0/\dot{\gamma}_{eff}$ for a range of shear rates then shows that Δz and x_0 remain approximately constant within the hexagonal regime. Figure (5.10b) contains additional data for $F_{\dot{\gamma}}(\omega)$ at lower shear rates. Recall that the values $\dot{\gamma}\tilde{\tau} = 230$ and 250 pertain to the shear-molten regime. As seen in Fig. (5.10b), the corresponding functions $F_{\dot{\gamma}}(\omega)$ still have one maximum, but its height is much lower and the entire distribution is much broader than in the hexagonal regime. In other words, there are still oscillations in the shear-molten state, but these have a broader spectrum of frequencies and are less synchronized. Moreover, the location of the maximum is different from the value $\omega_0/\dot{\gamma}_{eff} \approx 4.19$ in the hexagonal state and now depends on $\dot{\gamma}$. This can be understood when we recall that the particles in the shear-molten regime are not bound to lattice sites, thus, there is no fixed nearest neighbor distance. For completeness, we also note that the maximum of $F_{\dot{\gamma}}(\omega)$ still present in the shear-molten state vanishes entirely upon further decrease of $\dot{\gamma}$ into the square-ordered state. Hence, there is no motion of the layers, and thus no need for the particles to perform oscillations.

In view of the collective zig-zag motion of the particles, seen in the number density $N(y, t)$ (or, equivalently, the center of mass) it is an interesting question whether spatial correlations between the particles are influenced as well. To this end we now consider the distinct part of the intralayer van Hove correlation function defined by

$$G(y, t) = \left\langle \frac{1}{N_l} \sum_{i=1}^{N_l} \sum_{j \neq i}^{N_l} \delta[y - y_j(t + t') + y_i(t')] \right\rangle. \quad (5.11)$$

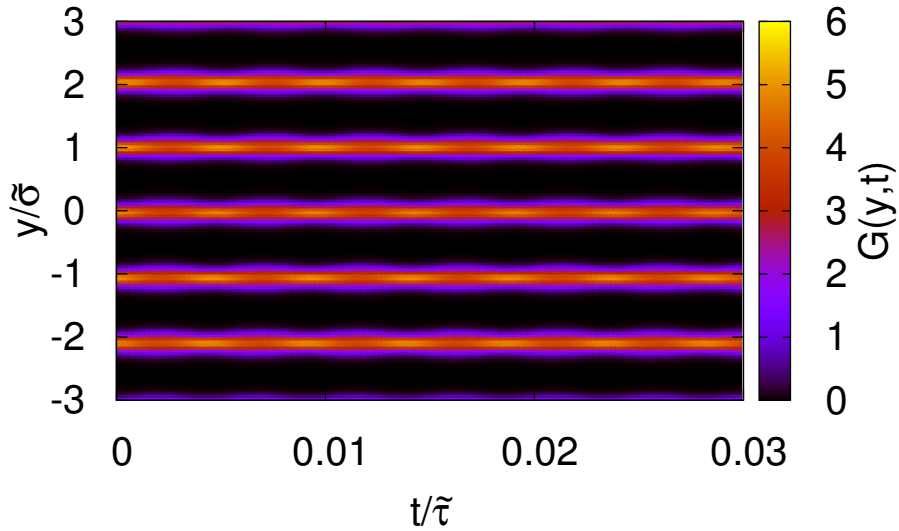


Figure 5.11: The distinct part of the van Hove function in vorticity direction at $\dot{\gamma}\tilde{\tau} = 400$.

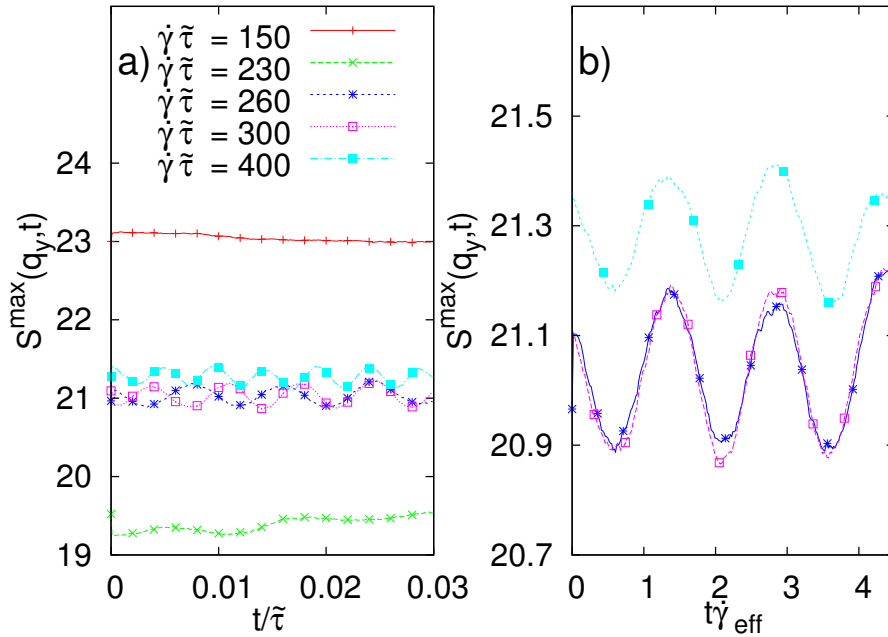


Figure 5.12: Rescaled oscillation of the structure factor in the vorticity direction.

At $t = 0$ this function couples to the conventional pair distribution function via $G(\mathbf{r}, 0) = \rho g(\mathbf{r})$ [16]. A representative result obtained at $\dot{\gamma}\tilde{\tau} = 400$ is shown in Fig. (5.11). The plot clearly reflects strong correlations induced by the hexagonal ordering. Note that, by definition, the oscillations of $N(y, t)$ are not directly visible in $G(y, t)$. However, closer inspection of the time dependence of the correlations at fixed y -distance reveals that there are oscillations in the *degree* of the correlations. The period of these oscillations appears to be constant over time. For a

better analysis we have calculated the spatial Fourier transform of $G(y, t)$, yielding the dynamic structure factor in vorticity direction, $S(q_y, t)$. As expected in a strongly correlated system, $S(q_y, t)$ (not plotted here) displays pronounced maxima at multiple of $q = 2\pi/y_0$ where $y_0 \approx 1\bar{\sigma}$ is the average nearest neighbor distance in y -direction. The height of the largest peak, $S^{max}(q_y, t)$ can then be interpreted as a measure of the degree of correlations. In Fig. (5.12a), we plot $S^{max}(q_y, t)$ at different shear rates. We can easily see that in the crystalline square-ordered state the correlation level of the system is very high. Increasing the shear rate and entering in the molten state the correlation strength in the system decreases until the layers recrystallize in the hexagonal state which leads to the increase of $S^{max}(q_y, t)$. Furthermore we can see, that the correlation strength in the hexagonal state performs oscillations. In order to understand this oscillatory behavior we plotted $S^{max}(q_y, t)$ rescaling the time scale with $\dot{\gamma}_{eff}$ for several shear rates pertaining to the hexagonal regime. The results are visualized in Fig. (5.12b). One observes indeed regular oscillations, confirming that not only the particles themselves, but also their correlations oscillate in time. Moreover, the frequency of the correlational oscillations coincides with those obtained for the position of the center of mass [see Fig. (5.10)]. We understand these correlations as follows: During one period of the zig-zag motion, a particle moves from its original position on the y -axis towards a position dictated by the “bypassing” of the barrier induced by particle in the adjacent layer, and then back to its original y -position. In the instant corresponding to the bypass, the available space is severely restricted. The same happens to the neighboring particle in the same layer in y -direction. As a consequence, correlations during the “bypass” are enhanced relative to those in the original arrangement.

Chapter 6

Shear induced laning in confined colloidal trilayer

Sometimes it can be of great importance to understand the behavior of the investigated system under very definite conditions. However, in the majority of cases more general description of the system properties is desired. Therefore, in this chapter our goal is to generalize the findings discussed in Chap. 5 and show which differences can be observed when the parameters are changed. Since it is impossible to investigate the change of all parameters at the same time we must make a decision and focus on one single characteristics. We opt for the variation of the distance between the confining walls, because small differences in L_z can induce significant changes within the system.

Using $L_z = 3.2\tilde{\sigma}$ instead of $L_z = 2.2\tilde{\sigma}$ [for details see Sec. 4.3] the colloids form three layers instead of two. Note that also in a trilayer system the zero-shear (equilibrium) structure is characterized by crystalline in-plane order with square-like symmetry [see Fig. (4.2b)].

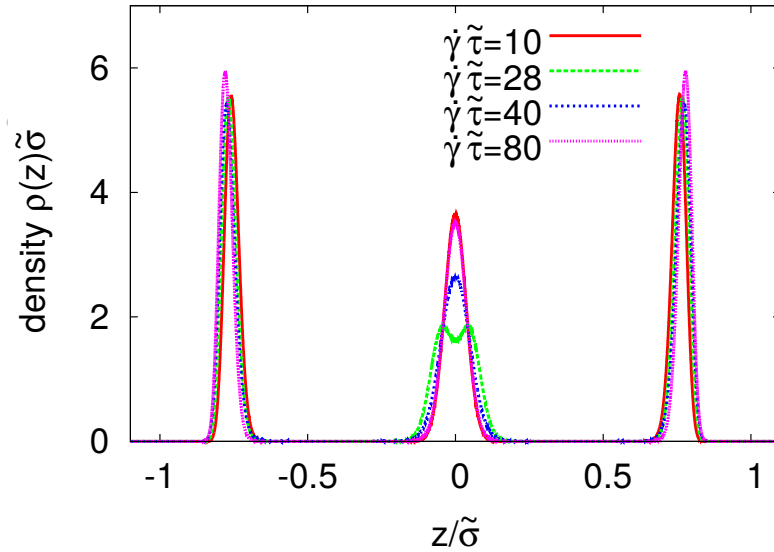


Figure 6.1: Density profiles along the shear gradient (and confinement) direction for different shear rates.

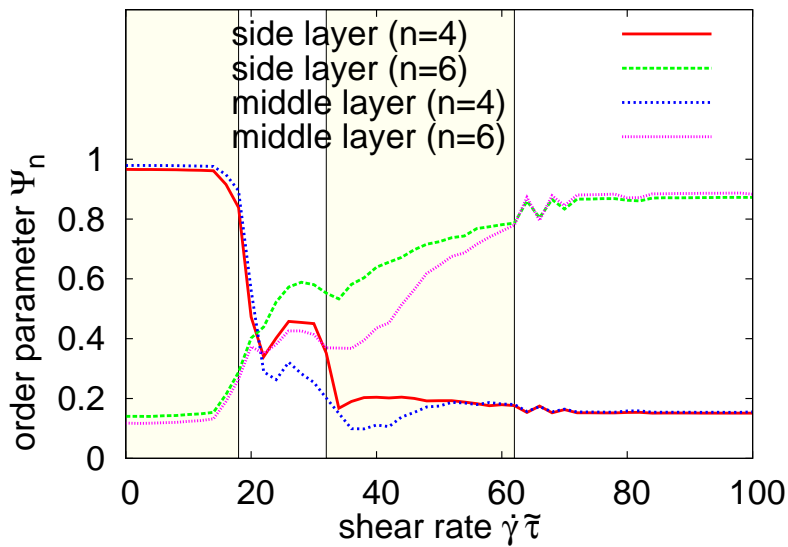


Figure 6.2: In-plane order parameter for square (Ψ_4) and hexagonal (Ψ_6) symmetry as a function of the shear rate $\dot{\gamma}$. The order parameter was calculated separately for the middle and the side layer.

6.1 Density distribution and translational order in a shear driven trilayer system

In our first step we calculate the density profile along the z -axis [see Eq. (2.58)] and the in-plane translational order parameter Ψ_n [see Eq. (2.66)]. In accordance with the previous chapter we also focus only on the square (*perfect square* $\Psi_4 = 1$)

and the hexagonal (*perfect hexagonal* $\Psi_6 = 1$) order. Numerical results for $\rho(z)$ and Ψ_n are plotted in Fig. (6.1) and Fig. (6.2), respectively. The interpretation of the results can be supported by the additional inspection of the simulation snapshots at different shear rates shown in Fig. (6.3).

Evaluating the results for the density distribution along the confinement axis we can see, that at low shear rates e.g., $\dot{\gamma}\tilde{\tau} = 10$ the middle peak in Fig. (6.1) is lower and wider compared to the side peaks. The shape of this peak becomes particularly interesting at e.g., $\dot{\gamma}\tilde{\tau} = 28$. Its decreasing height accompanied by significant changes of its shape [see Fig. (6.1)] leads to the assumption that the middle layer must split into two very near sublayers. At larger shear rates e.g., $\dot{\gamma}\tilde{\tau} = 40$ we observe a renewed increase of the maximum in the density profile of the middle layer and sharpening of the particle distribution. The splitting vanishes. In the last fourth state e.g., $\dot{\gamma}\tilde{\tau} = 80$ no substantial changes in the density distribution of the middle peak can be observed. It recovers to the shape observed at $\dot{\gamma}\tilde{\tau} = 10$.

The discussion of the translational order parameter reveals much more complex shear induced behavior of the trilayer system compared to the bilayer case [see Chap. 5]. At the discussed system parameters we can identify four different states. The first one is the *square state*, which corresponds to the equilibrium configuration [see Fig. (6.3a)] and persists at small shear rates. As discussed in Chap. 5 this state is characterized by the large value of Ψ_4 and the small value of Ψ_6 . Here the values of Ψ_4 and Ψ_6 do not change with the shear rate variation and the system persists in the crystalline state. The second state [see Fig. (6.3b)] shows a sharp decrease of the square, and increase of the hexagonal order parameter followed by a local maximum for Ψ_4 as well as Ψ_6 . The behavior shown by Ψ_n in this state could not be observed in Chap. 5 and occurs simultaneously with the splitting of the density profile in the middle layer. The third state [see Fig. (6.3c)] is denoted by the increasing hexagonal order and can be identified as the *molten* state discussed in Sec. 5.1. Further increase of the shear rate results in a saturation of Ψ_6 . At this range of shear rates Ψ_4 is very low. Thus, the last state is the *hexagonal* one [see Fig. (6.3d)]. From these discussions we can follow that the results concerning

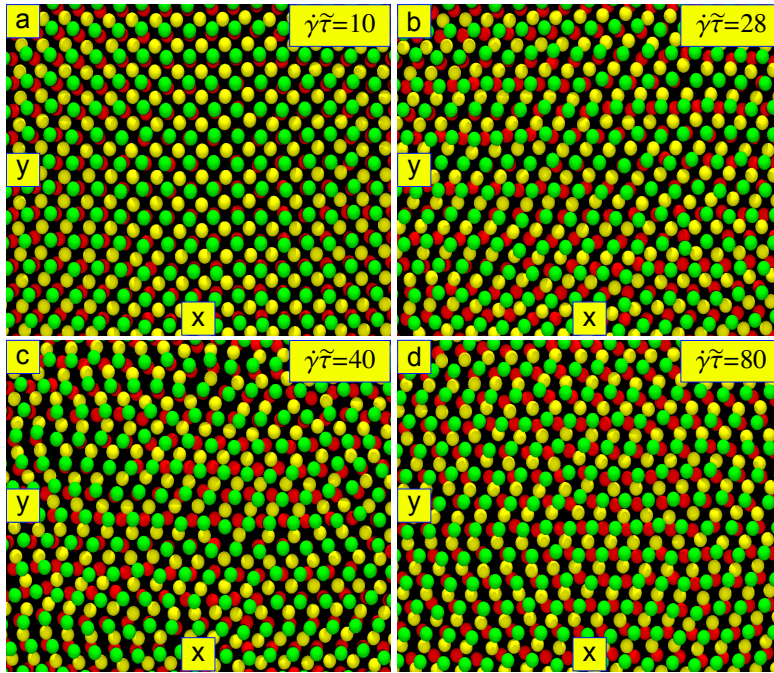


Figure 6.3: Simulation snapshot of the xy -plane at $\rho^* = 0.85$ and $L_z = 3.2\tilde{\sigma}$ for different shear rates. The green (yellow, red) circles represent particles of the upper (middle, lower) layer.

shear-induced order transitions presented in the bilayer case [see Sec. 5.1] are not unique and can be generalized for systems with larger number of layers. Moreover, the observation of the local maxima of the order parameter in Fig. (6.2), which characterize the second state, implies that the diversity of the system increases with increasing number of layers. Due to its novelty this new state deserves special attention and therefore will be discussed in detail in the following sections.

6.2 Semi-laning

For the explanation of the new state our attention must be focused on the processes occurring in the middle layer. Therefore, we plotted a snapshot of the middle layer [see Fig. (6.4)] and also calculated the density profile of this layer in the vorticity direction (y -axis) [see Fig. (6.5)]. In both cases we distinguished between the particles above and below the center of the simulation box at $z = 0$. As one can see in Fig. (6.4) in the square, molten and hexagonal states the particles of the *virtual* sublayers are arbitrarily distributed with respect to $z = 0$. However, in

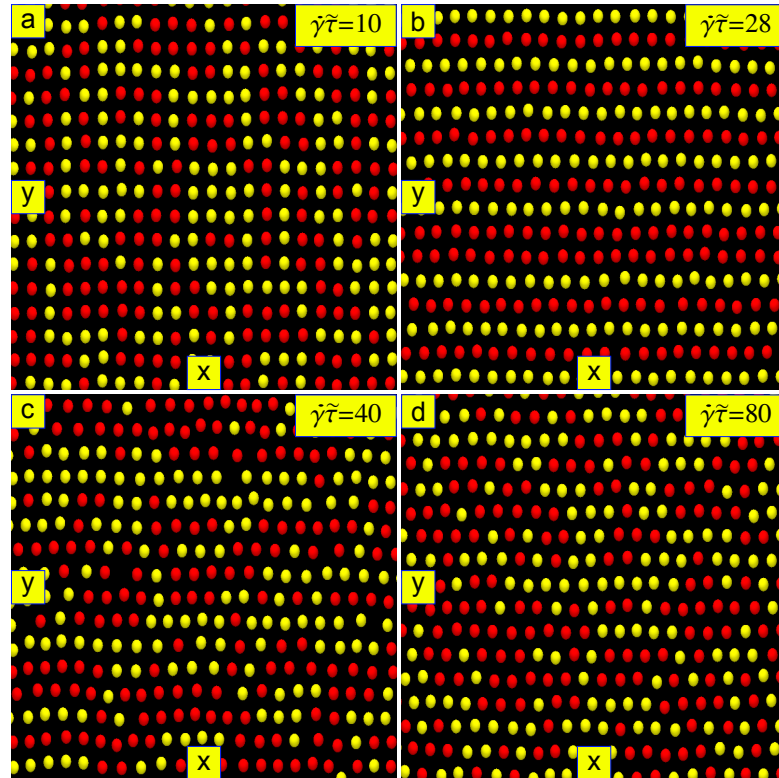


Figure 6.4: Simulation snapshot of the middle layer calculated along the xy -plane at $\rho^* = 0.85$ and $L_z = 3.2\tilde{\sigma}$ for different shear rates. The yellow (red) circles represent particles of the upper (lower) sublayer separated at $\langle z \rangle = 0$.

the second state the configuration of the particles shows a well pronounced laning behavior within the sublayers. The sequence of lanes from adjacent sublayers in this regime can be quantitatively accessed via the Fig. (6.5) in which the density profiles at $\dot{\gamma}\tilde{\tau} = 28$ and $\dot{\gamma}\tilde{\tau} = 40$ are compared.

The quality of the laning can be characterized via the laning order parameter suggested in [158]. In this formalism ϕ_i assigns the order parameter for each particle of the middle layer, which is chosen to be 1, when the lateral distance $|y_i - y_j|$ to all particles of the adjacent *sublayer* j is larger than a length scale $r_{lane} = \rho^{-1/3}$. Otherwise, ϕ_i is set to 0 [see Fig. (6.6)]. The total laning order parameter reads

$$\Phi = \frac{1}{N_{lane}} \left\langle \sum_{i=1}^{N_{lane}} \phi_i \right\rangle. \quad (6.1)$$

In Eq. (6.1) N_{lane} denotes the number of particles within the lane defined by the lateral distance r_{lane} . The result is visualized in Fig. (6.7). Here we can see that

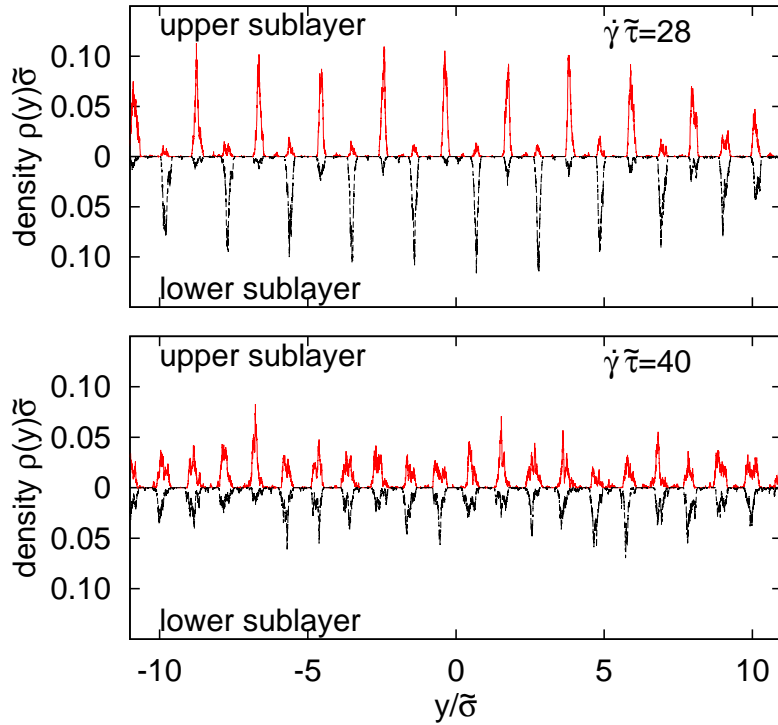


Figure 6.5: Density profiles of the sublayers of the middle layer in the vorticity direction. The sublayers were separated at $\langle z \rangle = 0$.

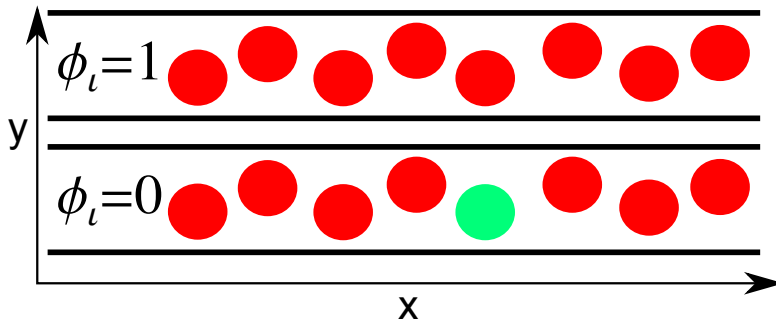


Figure 6.6: Sketch of the definition of the laning order parameter ϕ_i .

the assumptions made about the formation of lanes in the middle layer at shear rates $18 \lesssim \dot{\gamma}\tilde{\tau} \lesssim 32$ can be quantitatively verified.

Consequently, it should be also stressed that the calculation of the translational order parameter in the *semi-laned* state must yield distorted results due to the separation of the middle layer into sublayers. For the proper calculation of this order parameter the sublayers must be distinguished. Such a distinction is all the more important as each sublayer can have different velocities with a consequence of instantaneous changes of their mutual configuration.

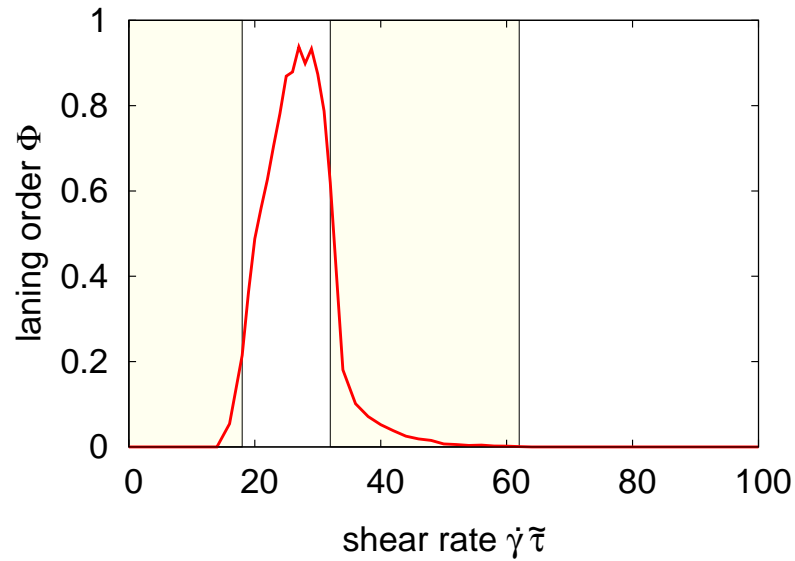


Figure 6.7: Laning order parameter calculated within the middle layer as a function of the shear rate $\dot{\gamma}$.

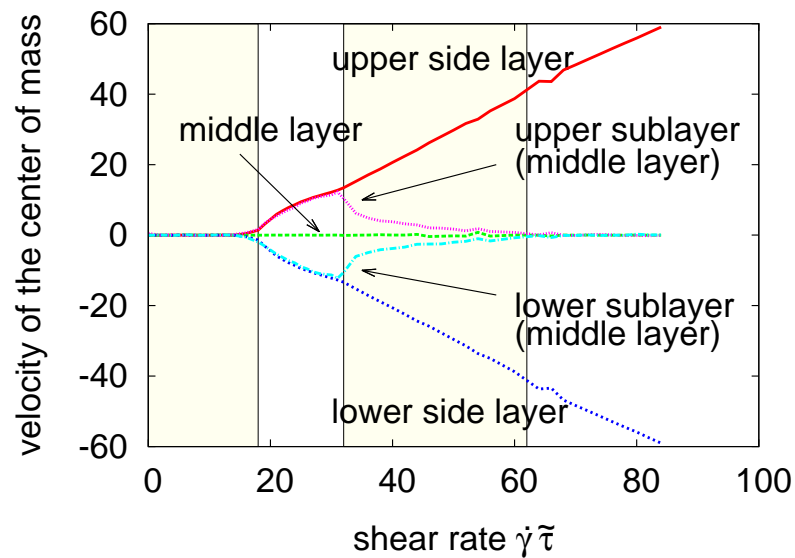


Figure 6.8: Velocity of the position of the center of mass of all three layers as well as the sublayers of the middle layer.

6.3 Shear induced dynamics

After the intensive discussion of the structural properties we want to focus on the system dynamics. For this purpose we calculated the velocity of the position of the center of mass for each layer and sublayer separately and plotted the results in Fig. (6.8). Furthermore, attempting to visualize the dynamics of the single particle the trajectories of every 10th particle along the flow direction (x -axis)

were plotted in Fig. (6.9).

In the square state we observe a still-standing behavior of particles [see Fig. (6.9a)] since they are caged within their lattice positions within the resting layers [see Fig. (6.8)]. However, evaluating the dynamics of the newly discovered semi-laned state and especially comparing it with the molten one we can see that the difference between the both states which was hardly detectable on the configuration level is obvious from the dynamical point of view. Inspecting the behavior of single trajectories [see Fig. (6.9b)] as well as the velocity of the center of mass [see Fig. (6.8)] we observe that in the middle layer all particles move either with the velocity of the upper or the lower side layer. As a consequence the shear profile transforms into two domains with opposite velocities separated at $z = 0$, the so-called plug flow. Moreover, the events at which trajectories in Fig. (6.9b) change their slope (changing the direction but not the absolute velocity) can be identified as jumps of particles from one layer or sublayer into the other one. In contrast to the latter state in the molten regime we observe a decoupling of the velocities of sublayers from their adjacent side layers [see Fig. (6.8)]. The shear rate at which this decoupling occurs can be identified as the starting point of the gradual destruction of the semi-laned state which finally transforms into the molten one. In the molten state the plug flow breaks down such that the shear profile is restored [see Fig. (6.9c)]. If there is a further rise of the shear rate we enter into the hexagonal regime in which the system dynamics is governed by the shear profile on the layer [see Fig. (6.8)] as well as on the particle level [see Fig. (6.9d)].

In the following we aim to deepen the understanding of the dynamics in the investigated system evaluating the mean squared displacement relative to the center of mass. We only focus on the MSD within the middle layer and consider flow (x) and vorticity (y) directions. Picking out only the middle layer and neglecting the behavior of sidelayers as well as the individual sublayers we can set the velocity of the position of the center of mass in this layer to zero which is justified by Fig. (6.8). The results for the MSD_x and MSD_y which were calculated via Eq. (5.3) are presented in Fig. (6.10). As we can see in the square ($\dot{\gamma}\tilde{\tau} = 10$) and the hexagonal ($\dot{\gamma}\tilde{\tau} = 80$) states the mean squared displacements in x - as well as in y -direction

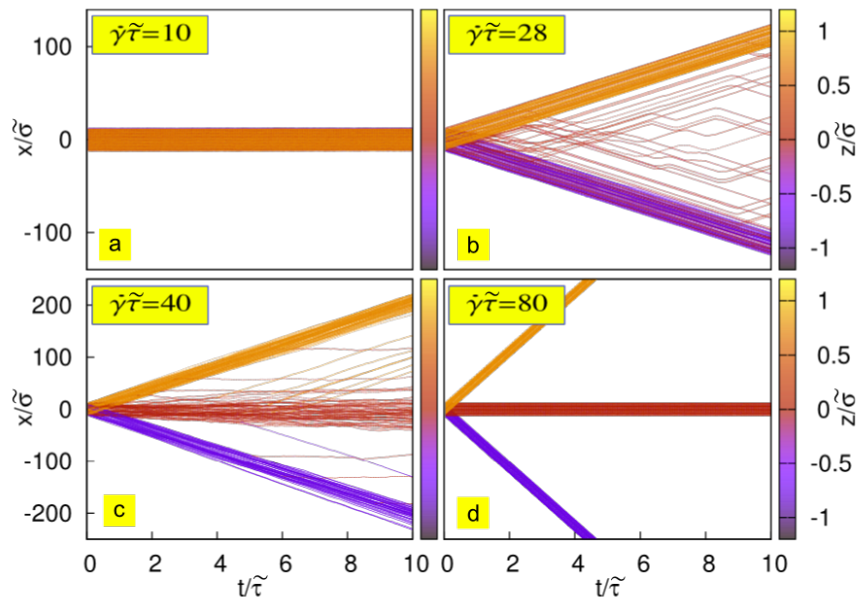


Figure 6.9: Trajectories of arbitrarily chosen particles at different shear rates.

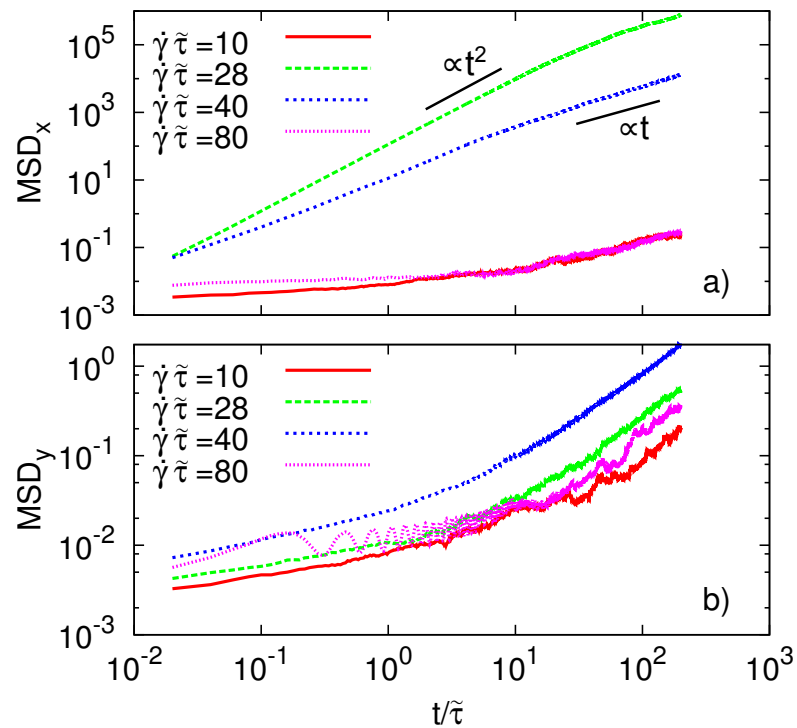


Figure 6.10: Mean squared displacement relative to the center of mass of the particles in the middle layer at different shear rates.

stays below $1\tilde{\sigma}$ in accordance with the observation of crystallization within the layers. In accordance with Chap. 5 in the shear molten state we observe enhanced transport of the particles within the layer. Furthermore, we can see that the diffusion in the flow direction is much faster than in the vorticity direction (since it is enhanced by the presence of shear).

At this point it should also be mentioned, that the application of the semi-analytical discussion, which is based on the motion of one sheared particle in harmonic potential presented in Sec. 5.3 is also very well suitable for the description of the mean squared displacement in the shear molten state in Fig. (6.10).

In the semi-laned state we expect the lanes to enhance the particle transport in the direction of shear. This fact which was already discussed in Fig. (6.8) and Fig. (6.9) can be also confirmed in Fig. (6.10a). However, in contrast to our expectation the mean squared displacement in flow direction is only at intermediate times $\propto t^2$. Inspecting the dynamics of the particles for longer times we observe that the slope of the corresponding MSD_x becomes diffusive ($\propto t$). Such a slowdown of particles in the semi-laned state at long time scales can be explained via calculation of the MSD_x for one single system which is presented in Fig. (6.11). Here, we observe an alternating change of the MSD_x slope which reflects that the motion of lanes is unstable. It is obvious that the particles in the middle layer perform a collective change of their direction of motion which can be explained by the reconfiguration of lanes.

Finalizing this chapter we also want to look at the particle exchange between the middle and side layers. The results presented in Fig. (6.12) show the relation of particles which stayed in the middle layer after time t to their initial number. As we can see in the square and hexagonal states $N_{middle}(t)/N_{middle}(0)$ is constant throughout the entire simulation time. In contrast to that we observe a well pronounced particle exchange between the layers in the semi-laned as well as in the shear molten state. The transport dynamics observed for these both states is characterized by significant differences. Since in the semi-laned state the particle transport is governed by a linear behavior in the shear molten state it is exponential.

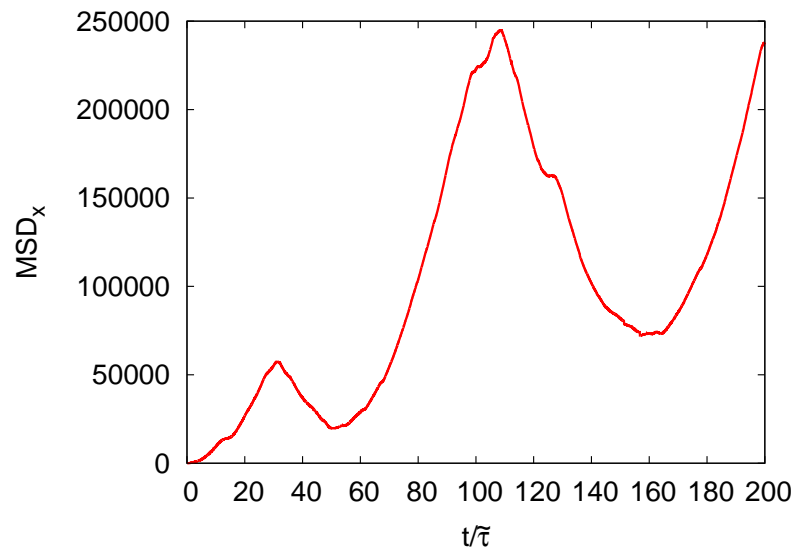


Figure 6.11: MSD_x of one single system at $\dot{\gamma}\tilde{\tau} = 28$. For the calculation only the particles from the middle layer were considered.

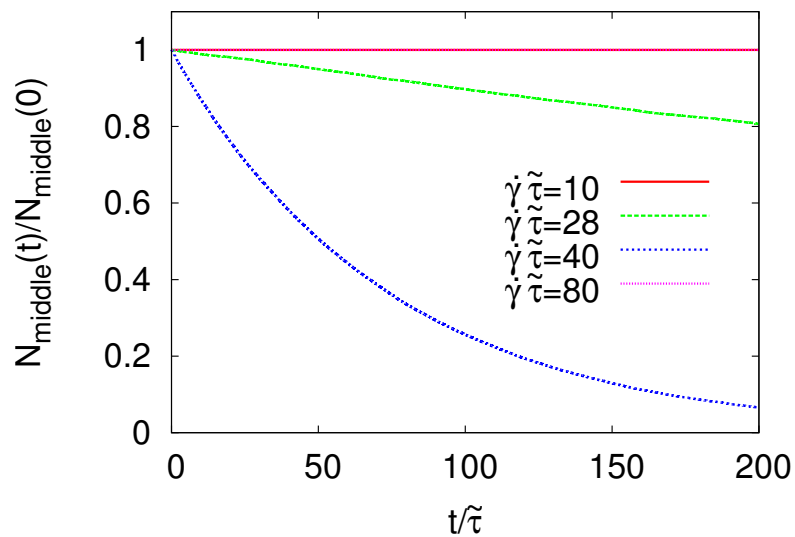


Figure 6.12: Particle transition from the middle layer to the side layers as a function of time. The number of particles was related to its initial value in the middle layer. For the calculation only the particles were considered which stayed in the middle layer during the time period $[0,t)$.

Chapter 7

Feedback control of non-equilibrium transitions

After the detailed discussion of the order transitions as well as the dynamical behavior of strongly confined colloidal suspension in the current chapter we focus on the viscoelastic properties of the investigated model system. The information gained about the stress response to the influence of shear will be used to apply feedback control. This implies that the shear rate $\dot{\gamma}$ will not be controlled by us (open-loop) as it was done in the previous chapters, but rather determined via the instantaneously measured input parameter (shear stress σ_{xz}). This in turn means that initially static shear rate becomes a dynamical variable.

The quantity of prime interest in the current chapter is the xz -component of the stress tensor,

$$\sigma_{xz} = \left\langle \frac{1}{V} \sum_i \sum_{j>i} F_{x,ij} z_{ij} \right\rangle, \quad (7.1)$$

which detailed derivation was presented in Sec. 2.4.4. We consider only the configuration dependent contribution to σ_{xz} ; the kinematic contribution (which involves the velocity components in x - and z -direction) is negligible under the highly confined conditions here. Moreover, note that apart from the kinematic contribution, Eq. (7.1) also neglects higher-order contributions involving gradients [159, 160]. In continuum approaches, one typically includes non-local terms which

are essential for the description of interfaces between shear-bands [52, 59]. The importance of such terms in our highly confined system, which is characterized by pronounced layer formation, remains to be investigated.

We introduce a feedback scheme, which is based on the shear stress, as follows. Starting from an initial value for $\dot{\gamma}$ and making use of Eq. (7.1) we calculate, in each time step, the configuration-dependent stress σ_{xz} and adjust $\dot{\gamma}$ via the relaxation equation

$$\frac{d}{dt}\dot{\gamma} = \frac{1}{\tau_c} \frac{\sigma_0 - \sigma_{xz}(t)}{\eta_0}, \quad (7.2)$$

where σ_0 is a *pre-imposed* value of σ_{xz} , and τ_c determines the time scale of relaxation. Also, η_0 is the shear viscosity obtained for $\dot{\gamma} \rightarrow 0$ (Newtonian regime). This control scheme is inspired by experiments under fixed stress [see, e.g. Ref. [77]], where the adaptation of the shear rate to a new stress value always takes a finite time. From a more formal point of view, we note that through Eq. (7.2), $\dot{\gamma}$ becomes an additional dynamical variable. Therefore, and since $\sigma_{xy}(t)$ depends on the instantaneous configuration $\{\mathbf{r}_i(t)\}$ of the particles, simultaneous solution of the $N + 1$ equations of motion via Eq. (4.1) and Eq. (7.2) forms a closed feedback loop with *global* coupling. Interestingly, this feedback scheme is in accordance with the common view that, in a stable system, the shear stress σ_{xz} should *increase* with the applied shear rate. This can be shown (at least for a homogeneous system) by a linear stability analysis of Eq. (7.2) as outlined in App. A.3.

7.1 Rheology of shear-induced transitions

We start by considering flow curves for systems at constant $\dot{\gamma}$. The functions $\sigma_{xz}(\dot{\gamma})$ for both, two- and three layer systems are plotted in Fig. (7.1), where we have included data for the viscosity $\eta = \sigma_{xz}/\dot{\gamma}$ [see Sec. 2.4.4]. Note that we have defined η via the externally applied rate $\dot{\gamma}$ rather than via the *effective* shear rate within the system (characterized by the average velocity of the layers [see Sec. 5.2]), which can show significant deviations from $\dot{\gamma}$. As seen from Fig. (7.1), both the bi- and the

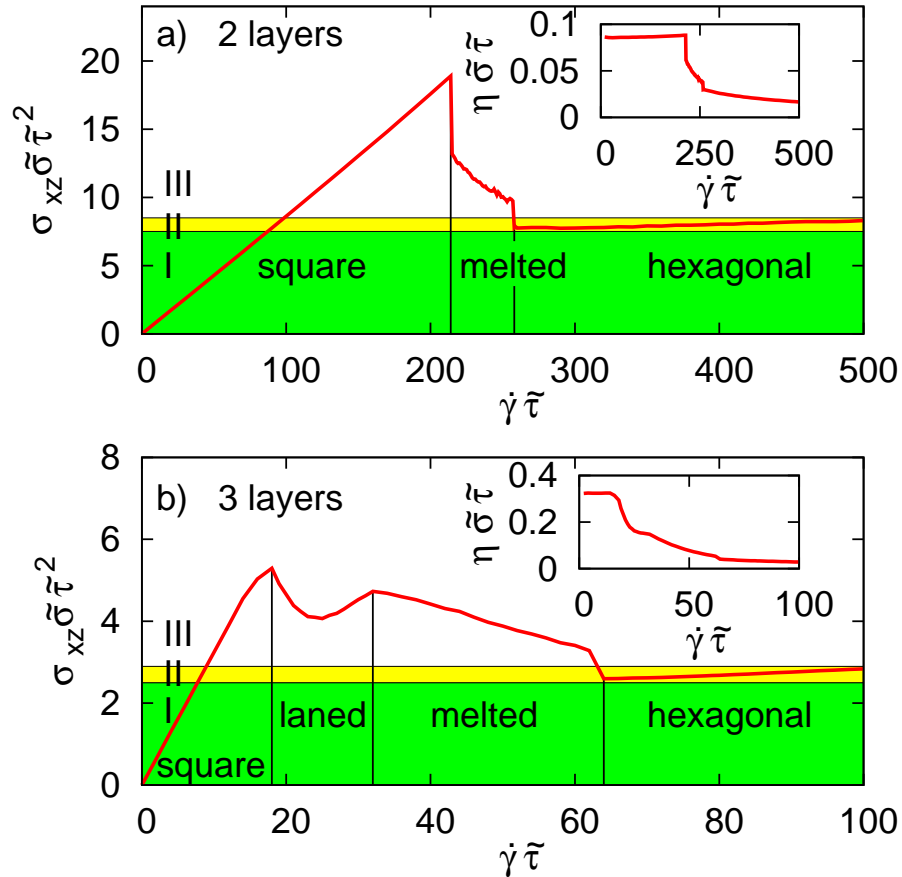


Figure 7.1: Steady state shear stress and shear viscosity (insets) for bi- and trilayer systems as function of the applied shear rate. Regions indicated as I, II, III are discussed in the main text.

trilayer systems are characterized by a non-monotonic flow curve, accompanied by pronounced shear-thinning. At small shear rates, the systems display linear stress, related to a Newtonian response of the square in-plane lattice structure. In fact, within the Newtonian regime (square state) the layer velocities are zero, i.e., the particles are “locked” [see Sec. 5.2]. In this state the lattice structure persists and the system reacts to the displacement of the particles in elastic manner. Further increase of the shear rate then destroys the square order. In the bilayer, the system then enters a shear-molten state characterized by the absence of translational order within the layers (as indicated, e.g., by a non-zero long-time diffusion constant in lateral directions [see Sec. 5.3]). At the same time, the entire system starts to flow, that is, the layer velocities increase from zero to non-zero values as shown in Fig. (5.6). From the function $\sigma_{xz}(\dot{\gamma})$ plotted in Fig. (7.1a), the appearance of the shear-molten state is indicated by a sudden decrease of σ_{xz} , implying the onset

of shear-thinning. In fact, within the shear-molten regime the slope of the flow curve is negative. For bulk systems, such a behavior implies that the system is mechanically unstable [see Sec. A.2] [161, 162]. Here we are considering a strongly confined system, where the macroscopic arguments cannot be immediately applied. Nevertheless, it is an interesting question to which extent the flow curve pertains to a true steady state in the regime where the shear rate has values corresponding to shear-molten configurations. Investigating the shear stress as function of strain [see Sec. 7.6] we find that σ_{xz} assumes indeed a constant value on the time scale of our simulations; however, the relaxation time is extremely long [see Sec. 7.3]. We also mention that our observation of shear-molten (long-time) configurations in the regime, where σ_{xz} decreases with $\dot{\gamma}$, is consistent with findings in an earlier theoretical study of a colloidal suspension under shear [163]. Somewhat different behavior is found in the trilayer system which displays a local minimum of the shear stress, before melting. This intermediate state is the semi-laned state discussed in Chap. 6. Only further increase of $\dot{\gamma}$ leads to the shear-molten state characterized by a decreasing flow curve. Finally, both systems transform into a state with in-plane hexagonal ordering and low viscosity. Regarding the stress, we see that the hexagonal regime is (in both systems) characterized by a slight increase of σ_{xz} with $\dot{\gamma}$. As a consequence, there is a parameter range (indicated as region "II" in Fig. (7.1)) where the flow curve is *multivalued*, that is, different $\dot{\gamma}$ lead to the same σ_{xz} . In many contexts (such as for worm-like micelles), multivalued flow curves are associated with the phenomenon of shear-banding, that is, the separation of the system into spatial regions with different shear rates. In our case, where the system consists of two or three layers such a separation can not occur. Instead, the non-monotonic stress curve is a consequence of the structural transitions of the system induced by the shear.

7.2 Stress tensor of shear-driven colloidal trilayer

In the previous section we focused on the shear stress and the corresponding viscosity under the influence of shear. However, for the sake of completeness the

behavior of other components of the stress tensor should be briefly discussed. Since the shear-induced trilayer system turned out to be more versatile compared to the bilayer in the current section we only focus on the former one. The results derived for the trilayer are presented in Fig. (7.2). Note that for the sake of consistency with the latter section the calculation of the components of the stress tensor was carried out via

$$\sigma_{mn} = \left\langle \frac{1}{V} \sum_i \sum_{j<i} F_{m,ij} n_{ij} \right\rangle, \quad (7.3)$$

with $n, m \in \{x, y, z\}$ such that the higher-order contributions involving gradients as well as the kinetic contribution were neglected. In accordance with previous observations inspecting the behavior of the diagonal elements of the stress tensor σ_{mm} as well as at the non-diagonal element σ_{mn} the existence of four well pronounced regimes becomes obvious. On the Fig. (7.2a) we observe that σ_{xx} and σ_{yy} are very similar. The relatively slight deviation between these both curves can be explained by the larger pressure of the particles in the flow (x -) direction due to the presence of shear. However, the structure and the absolute value of σ_{zz} is very different from the latter two. Nevertheless, the deviation of σ_{zz} towards much larger values of pressure with $P_{zz} = -\sigma_{zz}$ has its logical justification in the strong confining force applied by the plain parallel walls along the z -axis. Furthermore, we can see that the transition from one state into the next one, which is accompanied by an increase of the applied shear rate, is characterized by the increase of the pressure along the z -axis. This observation can be explained by the fact that the rise in the velocity and consequently the interaction strength between the particles pushes the layers slightly towards confining walls increasing their relative distance which can be verified from the density profile along the confinement direction in Fig. (5.2). One further interesting observation can be made inspecting the behavior of σ_{xy} in [see Fig. (7.2b)]. It was expected that the value of σ_{xy} would be equal to 0 (for all shear rates). However, it turned out that in the last state, at the shear rates which correspond to the hexagonal regime the σ_{xy} component of the stress tensor exhibits a behavior resembling Pitchfork bifurcation. Detailed inspection of this phenomenon showed that in this special

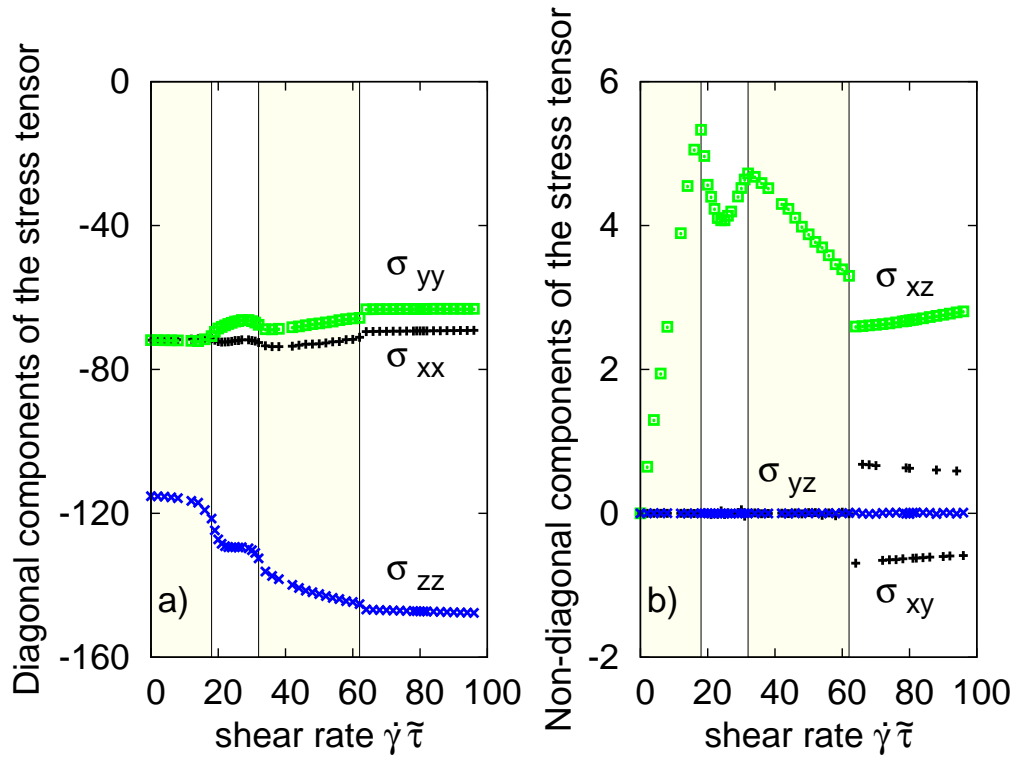


Figure 7.2: Components of the stress tensor as a function of the applied shear rate.

state the way of ensemble generation is of a big importance. It was observed that generating different ensembles before the transition into the hexagonal state took place we yield the expected results such that $\sigma_{xy} = 0$. However, if we start to generate a set of ensembles starting from the hexagonal configuration, then we observe that σ_{xy} relaxes towards one of two “pitchfork” branches as can be seen in Fig. (7.2b).

The reason for this discrepancy lies in small oscillations of the mutual layer distance along the z -axis. These oscillations drive the system into two different regimes which are sketched in Fig. (7.3). These regimes influence the spatio-temporal interaction strength between the colloids and therefore affect σ_{xy} . Generating a set of ensembles starting from the hexagonal configuration the system always begins and stays in one of the two regimes. Consequently, every single system as well as the whole ensemble average contains the contribution from only one regime (σ_{xy} is positive or negative). However, if the ensemble sampling is started before the transition into the hexagonal state takes place, the systems can evolve into the first or the second regime. Under such circumstances averaging over single

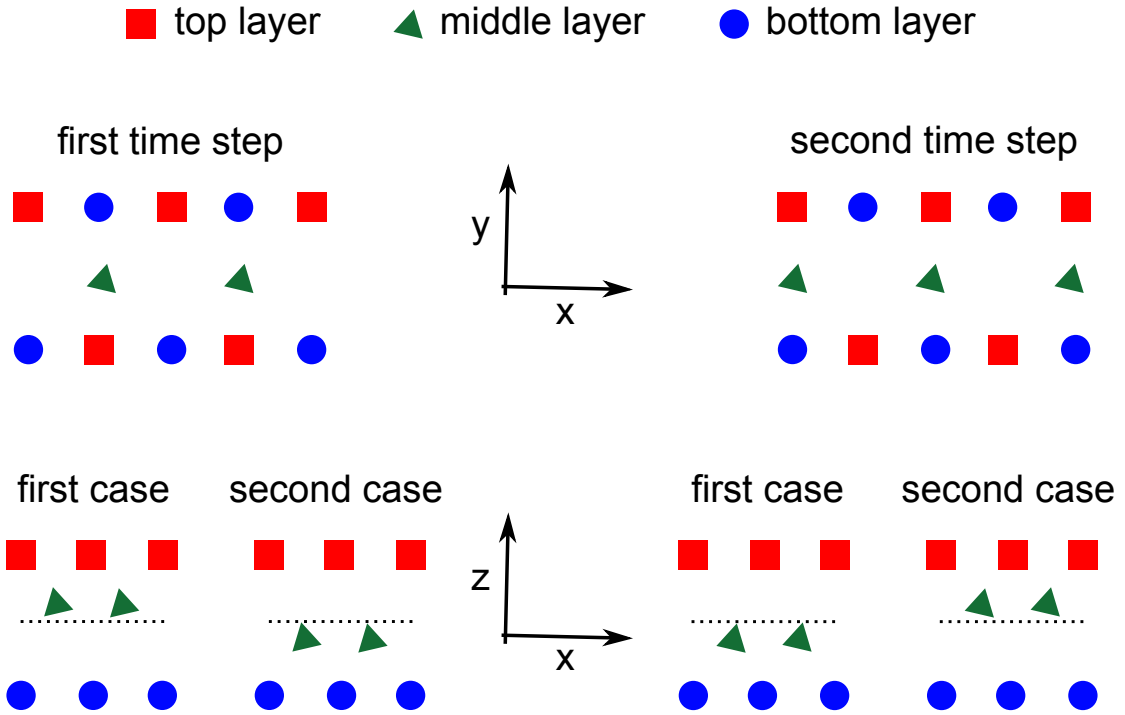


Figure 7.3: Sketch of the two possible regimes by which the pitchfork-like behavior of σ_{xy} in Fig. (7.2) can be explained.

systems one takes into account both cases and consequently yields $\sigma_{xy} = 0$.

7.3 Intrinsic time scales

Before exploring the impact of shear-stress control, which involves a time scale itself through the parameter τ_c [see Eq. (7.2)], we take a closer look at the *intrinsic* time scales characterizing the uncontrolled systems. We focus on the bilayer (the same findings apply qualitatively on the trilayer) and consider the response of the unsheared equilibrium system, which is in a square state, to a *sudden* switch-on at time τ_{on} of shear with rate $\dot{\gamma}_{\text{new}}$. The resulting time dependence of the instantaneous stress is plotted in Fig. (7.4).

If $\dot{\gamma}_{\text{new}}\tilde{\tau}$ has a value pertaining to the square state, the shear stress jumps at τ_{on} to a non-zero value but then settles quickly to its steady-state value [see Fig. 7.1]. At shear rates corresponding to the shear-molten state we can also observe a relaxation at some non-zero value. However, it should be emphasized that this value is *transient* in character. The true, steady state value is only achieved at

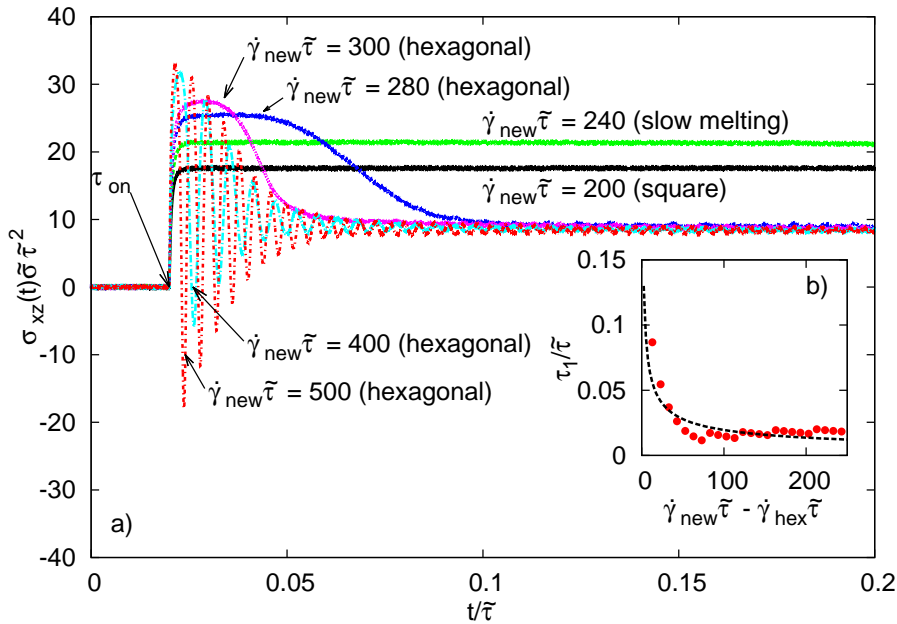


Figure 7.4: Response of $\sigma_{xz}(t)$ to a sudden switch-on (at time τ_{on}) of shear with different rates $\dot{\gamma}_{\text{new}}\tilde{\tau}$. The simulations were started from the equilibrium (square) state in a bilayer system. The inset shows the fit of the relaxation times τ_1 according to Eq. (7.4).

much longer simulation times (see the stress-strain relations presented in Sec. 7.6). Finally, for shear rates related to the hexagonal steady state ($\dot{\gamma}_{\text{new}}\tilde{\tau} > \dot{\gamma}_{\text{hex}}\tilde{\tau} \approx 257$, [see Fig. (7.1)]), we observe a well-pronounced stress overshoot, similar to what is observed e.g. in soft glassy systems [74], wormlike micelles [164] and polymer melts [165]. Closer inspection shows that the actual value of τ_1 as well as the functional behavior of $\sigma_{xz}(t)$ strongly depends on the distance between $\dot{\gamma}_{\text{new}}\tilde{\tau}$ and the threshold between shear-molten and hexagonal state, $\dot{\gamma}_{\text{hex}}\tilde{\tau}$: the smaller this distance is, the larger becomes τ_1 , and the more sensitive it is against small changes of the shear rate. Moreover, a sudden quench *deep* into the hexagonal state leads to an *oscillatory* relaxation of the stress $\sigma_{xz}(t)$ [see curves $\dot{\gamma}_{\text{new}}\tilde{\tau} = 400, 500$], with τ_1 (which now corresponds to the relaxation time of the envelope) being still quite large. Taken together, for $\dot{\gamma}_{\text{new}}\tilde{\tau} > \dot{\gamma}_{\text{hex}}\tilde{\tau}$, τ_1 can be fitted according to (see inset in Fig. (7.4))

$$\tau_i = \frac{a_i}{|\dot{\gamma}_{\text{new}}\tilde{\tau} - \dot{\gamma}_i\tilde{\tau}|^{b_i}}, \quad (7.4)$$

where we find $a_1/\tilde{\tau} = 0.21$, $b_1 = 0.52$ (setting $\dot{\gamma}_1\tilde{\tau} = \dot{\gamma}_{\text{hex}}\tilde{\tau}$). The oscillations occurring at large $\dot{\gamma}_{\text{new}}$ induce yet a different time scale τ_{os} , which is smaller than

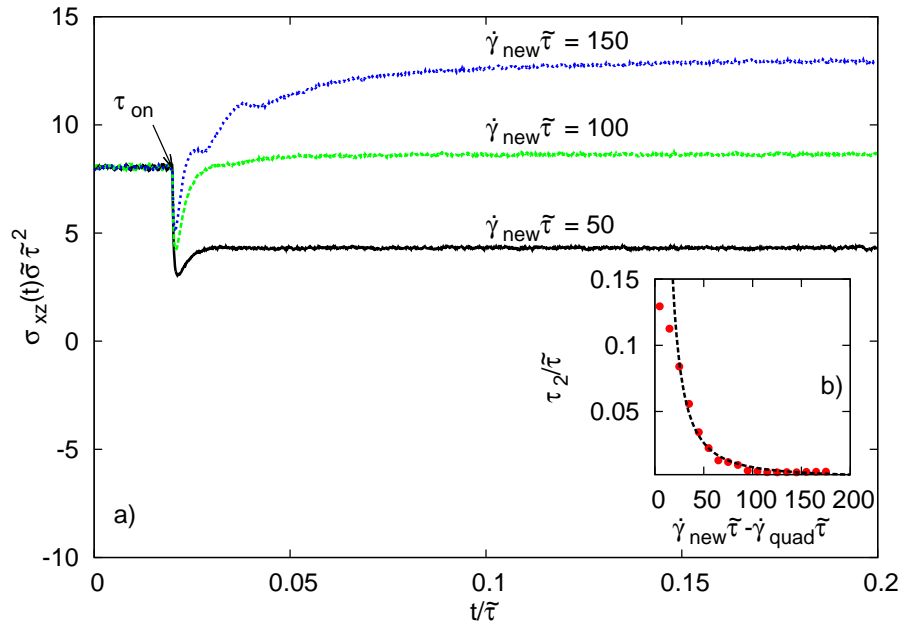


Figure 7.5: Response of $\sigma_{xz}(t)$ to a sudden change (at time τ_{on}) of shear. The new shear rates $\dot{\gamma}_{\text{new}}\tilde{\tau}$ result in a relaxation in the square state. The simulations were started from the hexagonal steady state at $\dot{\gamma}\tilde{\tau} = 400$ in a bilayer system. The inset shows the fit of the relaxation times τ_3 according to Eq. (7.4).

τ_1 . Specifically, we find $\tau_{\text{os}}/\tilde{\tau} = \mathcal{O}(10^{-3})$. The physical reason for these oscillations is the “zig-zag” motion of particles in adjacent layers [see Sec. 5.4]. This motion is accompanied by periodic variations of nearest-neighbor distances, and thus, pair forces, which eventually leads to oscillations of $\sigma_{xz}(t)$.

Furthermore, it is interesting to relate the relaxation times extracted from Fig. (7.4) to the structural transition from square to hexagonal state in Fig. (7.1). To this end we consider the Peclet number $Pe \equiv \dot{\gamma}\tau_{\text{Pe}}$ where τ_{Pe} is a “typical” relaxation time [166]. Identifying τ_{Pe} with τ_1 and considering shear rates $\dot{\gamma}$ close to the transition from the square into the shear-molten state, we find $Pe = \mathcal{O}(10^0)$. In other words, the shear-induced structural transitions happen at $Pe \geq 1$, consistent with our expectations [166].

For comparison we have also investigated the reverse situation, where the system is initially in a hexagonal steady state at shear rate $\dot{\gamma}_{\text{init}}\tilde{\tau} = 400$. We then suddenly change the shear rate towards a much smaller value and consider the relaxation towards the square equilibrium state. The corresponding behavior of $\sigma_{xz}(t)$ is shown in Fig. (7.5). Again we find that, the smaller the difference $\dot{\gamma}_{\text{new}}\tilde{\tau} - \dot{\gamma}_2\tilde{\tau}$ is, the larger τ_2 becomes (and the more pronounced is the sensitivity to small

changes in $\dot{\gamma}_{\text{new}}$). The resulting relaxation times can be also fitted via Eq. (7.4) with $a_2/\tilde{\tau} = 22.58$, $b_2 = 1.73$ and $\dot{\gamma}_2\tilde{\tau} = 215$, whereby $\dot{\gamma}_2\tilde{\tau} = \dot{\gamma}_{sq}\tilde{\tau}$ denotes the threshold between the square and the molten states. The result for this fit is visualized in the inset of the Fig. (7.5).

7.4 Impact of feedback control

We now discuss the impact of our shear stress control scheme defined in Eq. (7.2). The latter involves the zero-shear viscosity, η_0 , which is estimated from Fig. (7.1) to $\eta_0 = 0.086/\tilde{\sigma}\tilde{\tau}$ and $0.323/\tilde{\sigma}\tilde{\tau}$ for the bilayer and trilayer, respectively.

The overall dynamical behavior under feedback control strongly depends on the value of σ_0 (imposed shear) relative to the flow curve of the original system [see Fig. (7.1)]. We can differentiate between regimes I, II, and III, which are indicated in Fig. (7.1).

For a σ_0 chosen in region I, the response of the system is *unique*, that is, the final state is independent of the control time scale τ_c , as well as of the initial shear rate $\dot{\gamma}_{\text{init}}$ and the initial microstructure. Thus, when starting from a square state, with a corresponding initial shear rate $\dot{\gamma}_{\text{init}}$, the system immediately settles at this state. As a more critical test of the injectivity of the flow curve in region I, we plot in Fig. (7.6a) and Fig. (7.6b) the functions $\dot{\gamma}(t)$ and $\sigma_{xz}(t)$ for the bilayer system at $\sigma_0\tilde{\sigma}\tilde{\tau}^2 = 6$ and various τ_c , starting from a *hexagonal* configuration (and $\dot{\gamma}_{\text{init}}\tilde{\tau} = 400$). In all cases, the shear rate decreases towards the value $\dot{\gamma}\tilde{\tau} \approx 70$ and the structure relaxes into the square state pertaining to the value $\sigma_{xz}\tilde{\sigma}\tilde{\tau}^2 = 6$ in the *uncontrolled* system. This indicates that the square state in region I is indeed the only fixed point of the dynamics. We also see from Fig. (7.6a) that the relaxation time into this steady state increases with τ_c . Figure (7.6b) additionally shows that $\sigma_{xz}(t)$ displays a pronounced peak. The peak indicates the time window in which the initial hexagonal ordering transforms into a square one. In fact, the high values of σ_{xz} at the peak reflect the large friction characterizing the intermediate molten state. Similar behavior occurs in region I of the trilayer system [see Fig. (7.6c-d)] where, however, fluctuations of $\sigma_{xz}(t)$ are generally larger.

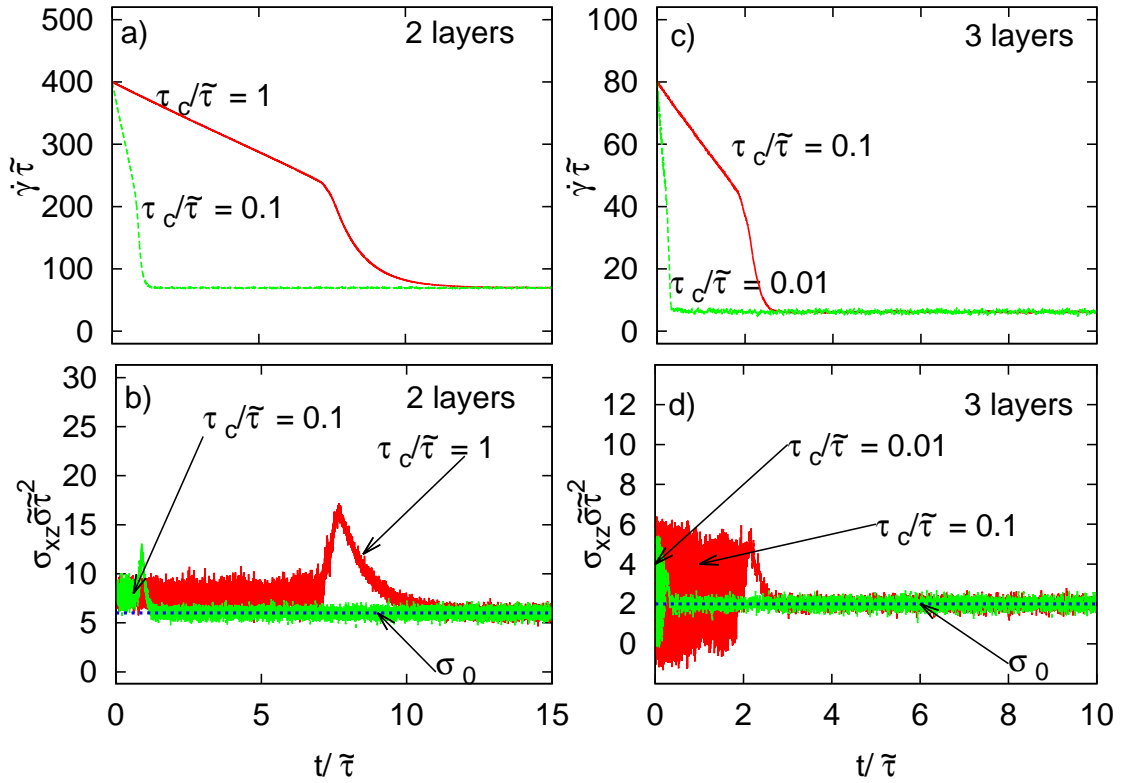


Figure 7.6: Time dependence of the instantaneous shear rate and shear stress for a bilayer- (a,b) and a trilayer system (c,d) in presence of feedback control within region I. The imposed stress was set to $\sigma_0\tilde{\sigma}\tilde{\tau}^2 = 6(2)$ for the bilayer (trilayer) system. Various values of $\tau_c/\tilde{\tau}$ are considered. The initial configuration is hexagonal.

We now choose σ_0 within region II of the flow curve, where there are three different shear rates (and thus, three fixed points) pertaining to the same stress [see Fig. (7.1)]. We focus on systems which are initially in a square configurations, whereas the initial shear rate $\dot{\gamma}_{\text{init}}$ has a value pertaining to the hexagonal state (other initial conditions will be discussed below). The impact of τ_c on the time dependence of $\dot{\gamma}(t)$ and $\sigma_{xz}(t)$ is shown in Fig. (7.7). For small values of the control time scale the systems stays in the initial lattice configuration, i.e., $\dot{\gamma}$ relaxes towards the value pertaining to the square state ($\dot{\gamma}\tilde{\tau} \approx 90$). Different behavior occurs at larger values of $\tau_c/\tilde{\tau}$: Although the initial structure is square, the final state is *hexagonal*, and the shear rate essentially remains at its high initial value. We stress that these findings crucially depend on the choice of $\dot{\gamma}_{\text{init}}$. In particular, the dependency of the long-time behavior on $\tau_c/\tilde{\tau}$ only arises for large values of $\dot{\gamma}_{\text{init}}$; for small values the system remains in the square state irrespective of τ_c . An overview of the final dynamical states in the feedback-controlled bilayer at $\sigma_0\tilde{\sigma}\tilde{\tau}^2 = 8$ and various

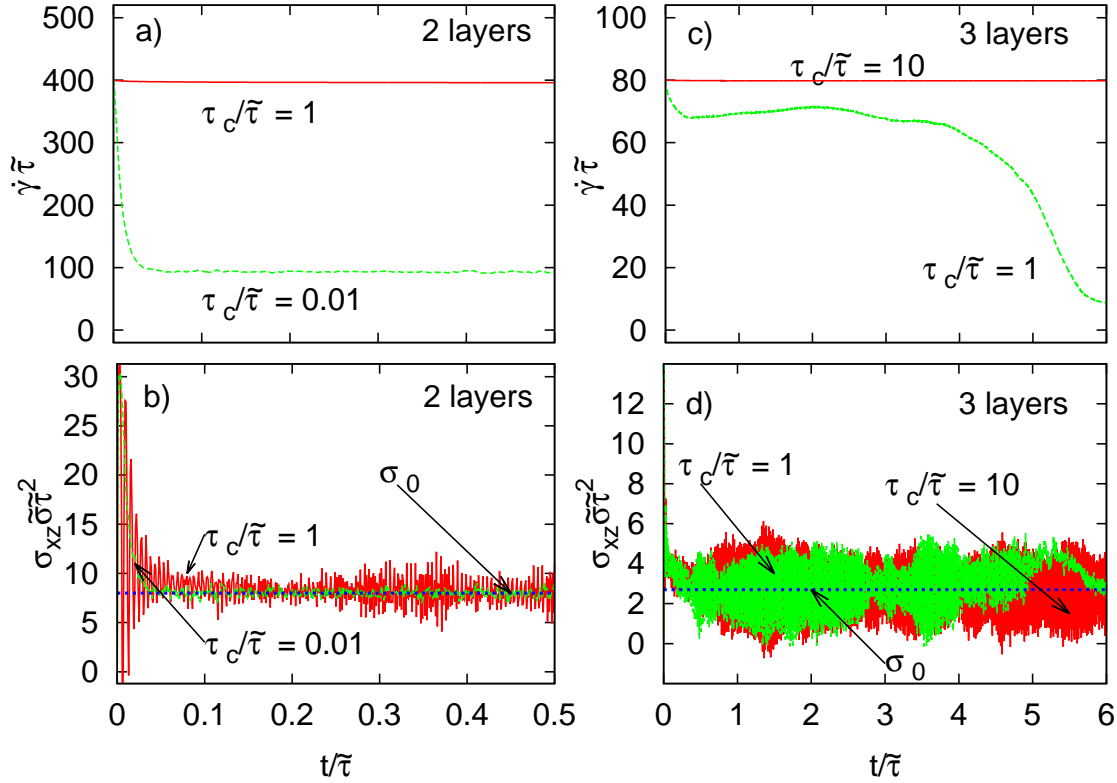


Figure 7.7: Same as Fig. (7.6), but for $\sigma_0\tilde{\sigma}\tilde{\tau}^2 = 8(2.7)$ for the bilayer (trilayer) system (region II). The initial configuration is square.

combinations of $\dot{\gamma}_{\text{init}}$ and $\tau_c/\tilde{\tau}$ (assuming a square initial structure) is given in Fig. (7.8). The colour code indicates the ratio of local translational order parameters $\langle\Psi_6/\Psi_4\rangle$ [for a definition of the Ψ_n see Sec. 2.4.3]. The restriction to values $\langle\Psi_6/\Psi_4\rangle \leq 6$ is related to the actual values observed in the simulations. From Fig. (7.8) one clearly sees that for initial shear rates $\dot{\gamma}_{\text{init}}\tilde{\tau} > \dot{\gamma}_{\text{hex}}\tilde{\tau} \approx 257$, the final state of the feedback-controlled system depends on $\tau_c/\tilde{\tau}$. This is in contrast to the uncontrolled system which becomes hexagonal for all $\dot{\gamma}_{\text{init}} > \dot{\gamma}_{\text{hex}}$. For a hexagonal initial configuration the diagram looks similar from a qualitative point of view; however, the range of control times where the system retains a hexagonal state despite of $\dot{\gamma}_{\text{init}} < \dot{\gamma}_{\text{quad}}$ (with $\dot{\gamma}_{\text{quad}}$ being the threshold between square/molten states) is much smaller [see Fig. (7.9)] We conclude that, by varying τ_c and the initial structure, we can “select” between the two stable, steady-state configurations arising in the multivalued region of the uncontrolled system. That these states are stable also under feedback (stress) control is supported by the linear stability analysis presented in App. A.3. Indeed, the dynamics under feedback

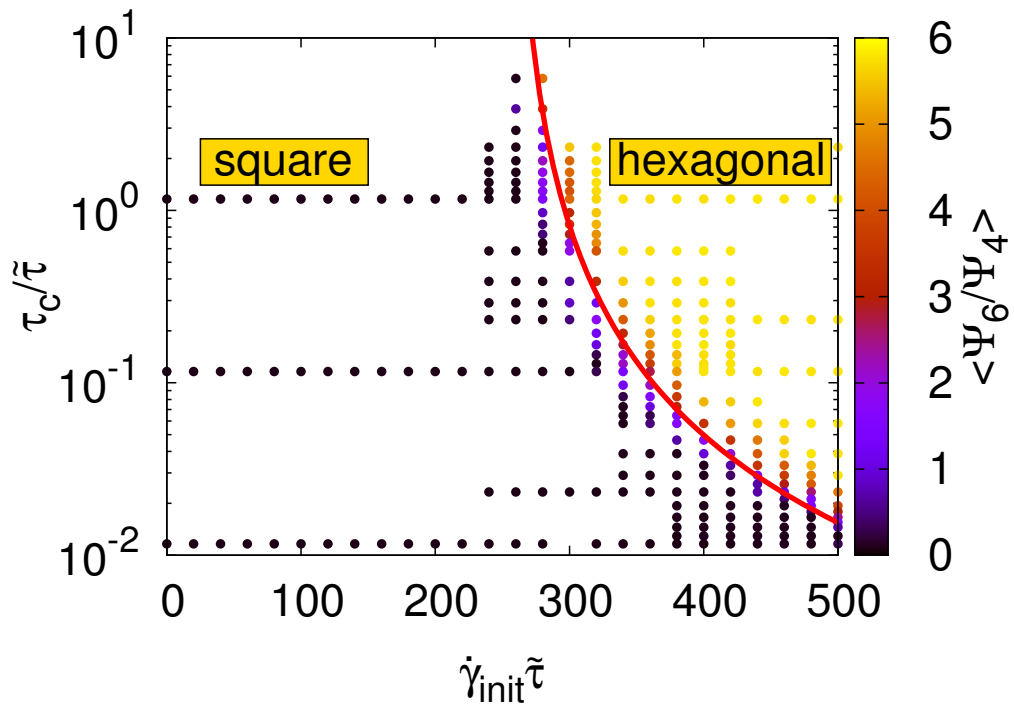


Figure 7.8: State diagram indicating long-time lattice structures. All simulations were started from a square ordered bilayer and the imposed shear stress was set to $\sigma_0\tilde{\sigma}\tilde{\tau}^2 = 8$. The line shows the result from Eq. (7.8).

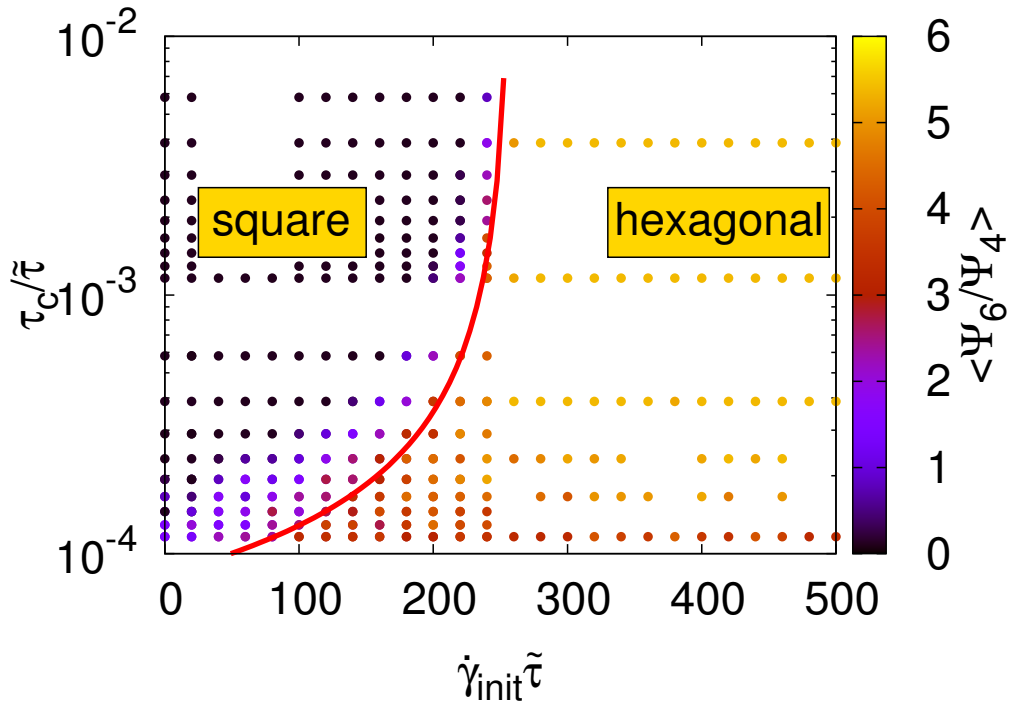


Figure 7.9: State diagram indicating long-time lattice structures. All simulations were started from the hexagonal ordered bilayer and the imposed shear stress was set to $\sigma_0\tilde{\sigma}\tilde{\tau}^2 = 8$.

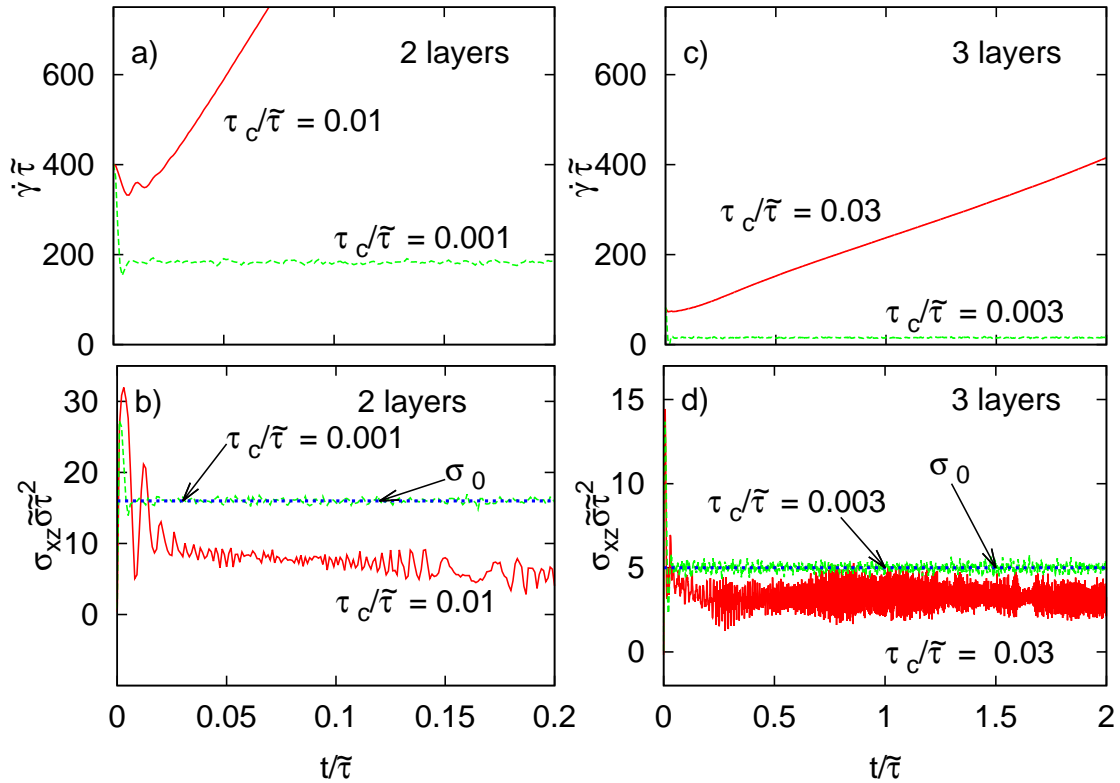


Figure 7.10: Same as Fig. (7.7), but for $\sigma_0 \tilde{\sigma} \tilde{\tau}^2 = 16(5)$ for the bilayer (trilayer) system (region III). The initial configuration is square.

control *never* evolves towards the intermediate, shear-molten states, consistent with the view that these states are mechanically unstable. This holds also in region III of the flow curve of the uncontrolled system [see Fig. (7.1)], e.g., for $\sigma_0 \tilde{\sigma} \tilde{\tau}^2 = 16(5)$ for the bilayer (trilayer): Here, a small value of τ_c yields relaxation towards the square state, whereas for large τ_c , the system evolves into a hexagonal state [see Fig. (7.10)]. However, note that although the system evolves towards the hexagonal state, this state cannot be stabilized since in the considered range of shear rates all $\sigma_{xz}(\dot{\gamma})$ pertaining to the hexagonal state are smaller than the imposed value of the shear stress σ_0 . Finally, we note that completely analogous behavior is found in the trilayer system [see Fig. (7.7c-d)] for a σ_0 pertaining to the regime where square, molten and hexagonal states exist.

7.5 Transition line

The most significant observation from Fig. (7.8) is that at high values of $\dot{\gamma}_{\text{init}}$, the feedback-controlled system can achieve *either* the hexagonal or the square configuration, provided that we start from a square configuration and choose $\tau_c/\tilde{\tau}$ accordingly. We now propose a simple model which allows us to estimate the *transition* values of the control time, τ_c^{trans} .

The physical idea behind our model is that, with the initial conditions described above, relaxation into the hexagonal state only occurs if the *reorganization* time τ_{reorg} required by the system to transform from a square into a hexagonal configuration, is smaller than the time τ_{decay} in which $\dot{\gamma}$ decays to a value pertaining to the square state. We can estimate τ_{decay} from Eq. (7.2) if we assume, for simplicity, a *linear* relationship $\sigma_{\text{xz}}(t) = m\dot{\gamma}(t)$ (note that such a relationship is indeed nearly fulfilled *within* the square and hexagonal states [see Fig. (7.1)]. Under this assumption Eq. (7.2) can be easily solved, yielding

$$\dot{\gamma}(t) = m^{-1}e^{-mt/\eta_0\tau_c} (m\dot{\gamma}_{\text{init}} - \sigma_0 + e^{mt/\eta_0\tau_c}\sigma_0). \quad (7.5)$$

From Eq. (7.5) we find that the decay time of $\dot{\gamma}$ to the threshold value $\dot{\gamma}_{\text{hex}}\tilde{\tau} \approx 257$ (below which the hexagonal state of the uncontrolled system is unstable) is given by

$$\tau_{\text{decay}} = \frac{\tau_c\eta_0}{m} \ln \left(\frac{m\dot{\gamma}_{\text{init}} - \sigma_0}{m\dot{\gamma}_{\text{hex}} - \sigma_0} \right). \quad (7.6)$$

To estimate the reorganization time τ_{reorg} (from the initial square into a hexagonal configuration), we assume that its dependence on $\dot{\gamma}_{\text{init}}$ is analogous to that of the relaxation time τ_1 introduced for the *uncontrolled* system [see Eq. (7.4)]. Specifically, we make the ansatz

$$\tau_{\text{reorg}} = \frac{a'}{|\dot{\gamma}_{\text{init}}\tilde{\tau} - \dot{\gamma}_{\text{hex}}\tilde{\tau}|^{b'}}. \quad (7.7)$$

As stated above, a crucial assumption of our model is that the system can only reach the hexagonal state if τ_{reorg} does not exceed τ_{decay} . Note that the latter involves (in fact, is proportional to) the time τ_c . By equating expressions Eq.

(7.6) and Eq. (7.7) for τ_{decay} and τ_{reorg} , respectively, we can therefore find an expression for the *minimal* control time, τ_c^{trans} , above which the system reaches the hexagonal state, that is

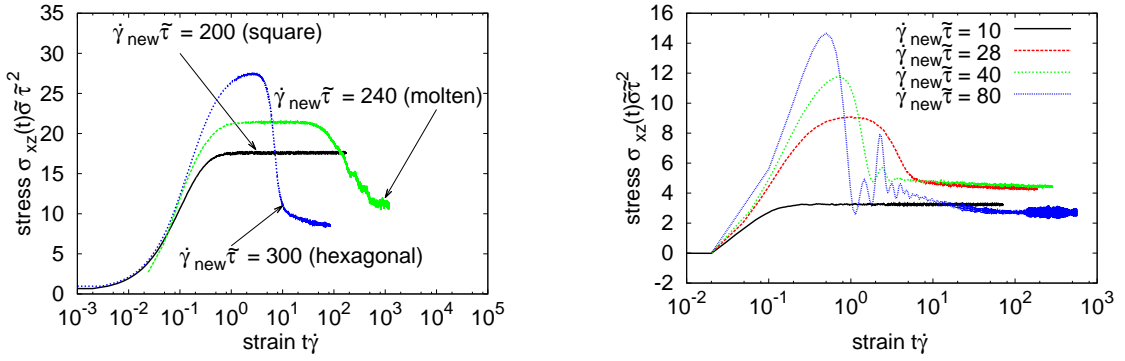
$$\tau_c^{\text{trans}} = \frac{a'm}{|\dot{\gamma}_{\text{init}}\tilde{\tau} - \dot{\gamma}_{\text{hex}}\tilde{\tau}|^{b'}\eta_0 \ln\left(\frac{m\dot{\gamma}_{\text{init}} - \sigma_0}{m\dot{\gamma}_{\text{hex}} - \sigma_0}\right)}. \quad (7.8)$$

Due to the square initial configuration, we set $m = \eta_0$ and $\sigma_{xz}(t) = m\dot{\gamma}(t)$ as defined in our *ansatz*. The remaining parameters a' and b' are determined by fitting the numerical results for $\tau_c/\tilde{\tau}$ at the boundary [see Fig. (7.8)] to expression (7.8), yielding $a'/\tilde{\tau} = 54.127$ and $b' = 1.503$. The resulting line $\tau_c^{\text{trans}}(\dot{\gamma}_{\text{init}})$ is included in Fig. (7.8), showing that our estimate describes the transition between square and hexagonal states very well.

Similar considerations are possible, when we use a hexagonal initial lattice structure. Choosing then a *small* value of $\dot{\gamma}_{\text{init}}\tilde{\tau}$ we find that we can switch between hexagonal and square state. This is illustrated in Fig. (7.9). To obtain the corresponding transition values of τ_c , we use the same strategy as before, but take a different *ansatz* for the stress. Specially, we set $\sigma_{xz}(t) = n + m\dot{\gamma}(t)$ which approximately describe the flow curve in the hexagonal state of the uncontrolled system. From the results plotted in Fig. (7.1) we find $n = 7.0477/\tilde{\sigma}\tilde{\tau}^2$ and $m = 0.0025$. The analog of the Eq. (7.8) then reads

$$\tau_c^{\text{trans}} = \frac{a'm}{|\dot{\gamma}_{\text{init}}\tilde{\tau} - \dot{\gamma}_{\text{hex}}\tilde{\tau}|^{b'}\eta_0 \ln\left(\frac{n+m\dot{\gamma}_{\text{init}} - \sigma_0}{n+m\dot{\gamma}_{\text{hex}} - \sigma_0}\right)} \quad (7.9)$$

with $a'/\tilde{\tau} = 0.012$ and $b' = 0.237$ [see Fig. (7.9)]. The result is visualized in Fig. (7.9). Comparing the typical control time scales at the transition with those seen in Fig. (7.8) we find that $\tau_c/\tilde{\tau}$ which is necessary to switch from square into the hexagonal state [see Fig. (7.8)] is about two orders of magnitude larger than switching from hexagonal into the square state. We suspect that this difference results from the differences of the slope of the shear stress in the square and hexagonal regimes.



(a) Stress-strain relations in the colloidal bilayer for different shear rates, starting from the equilibrium (square) configuration.

(b) Stress-strain relations in the colloidal trilayer for different shear rates, starting from the equilibrium (square) configuration.

Figure 7.11: Stress-strain relations for bi- and trilayer.

7.6 Strain-stress relation under constant shear rate

In this section we present results for stress-strain relations at different fixed values of $\dot{\gamma}$ for bi- and trilayer systems. In contrast to the other numerical simulations here we start from equilibrium and switched the shear on. Numerical results are shown in Fig. (7.11).

In both systems one observes simple, monotonic behavior when the shear rate pertaining to the square state is applied, while at larger shear rates pronounced stress overshoots can be measured. Moreover, we also observe that the relaxation time of the overshoot increases when $\dot{\gamma}_{new}$ approaches the regime of shear rates characteristic for the square ordered state.

Note that these findings are consistent with the appearance of a particularly large intrinsic relaxation time as discussed in Sec. 7.3.

Chapter 8

Conclusion and Outlook

8.1 Conclusion

In the framework of this thesis the influence of shear on strongly confined colloidal suspensions has been discussed. The investigations are mainly based on the model proposed for the simulation of charged silica suspensions [2, 124–127] as well as the observations made in sheared colloidal melts [3]. In our study we focused on structural, dynamical and rheological properties of the model system.

In Chap. 5 we have started from a high-density equilibrium state with lateral square-ordered colloidal bilayer. We found that at low shear rates the structure remains unchanged, with both layers being “pinned” in their original positions (i.e., zero net motion of the layers). Only above a certain shear rate the layers start to move and the crystalline order melts. At large shear rates the system recrystallizes into a state with hexagonal in-plane ordering. To address the dynamical properties of our model system the mean squared displacement for all three states was calculated. In the square and the hexagonal states the MSD reaches a plateau at long times. However, in the shear molten regime the particles are able to escape their lattice positions. For the latter state we proposed a simple, semi-analytic model by which the time-dependence of the in-plane mean squared displacement can be accurately described. Furthermore, in the hexagonal state we observed

the appearance of the zig-zag motion of layers along the vorticity direction. The frequency of these oscillations scales with the effective shear rate. The same behavior has been recently observed in experiments of shear-driven colloidal films, performed at macroscopic film thicknesses [65]. Moreover, we have shown that the oscillations of the particle positions are accompanied by oscillations of their spatio-temporal correlation [see Sec. 5.4].

In Chap. 6 we aimed to generalize the findings gained in the bilayer system. For this purpose we mainly focused on the trilayer system. Using increased number of layers we could confirm all observations made in the bilayer system. Additionally to the three intensively discussed states under conditions which pertain to the trilayer system a novel “semi-laned” state was observed. This state is positioned at shear rate values between those which are typical for the square and the shear-molten states. In the new state the dynamics can be described by the formation of the plug flow (two domains with the same velocity magnitude but opposite flow directions) rather than by the shear profile. The plug flow velocity interface is positioned in the middle of the shear cell which consequently means a breakup of the middle layer in two sublayers sliding past each other. This results in a significant increase of the particle velocity within the middle layer. Furthermore, the sublayers align in lanes. The appearance of lanes within the middle layer is even more intriguing when one considers that the particles of the adjacent lanes belong to the same species and are distinguished only by their position in the system which was dictated implicitly by the system parameters and without any explicit separation into species or charges.

In Chap. 7 we have studied the complex dynamical behavior of sheared colloidal (bilayer and trilayer) films under a specific type of feedback control. Proposing to control the shear rate via the instantaneous value of the shear stress we were inspired by the real experimental setup [77]. In the latter experimental study the shear rate of the system is not directly controlled (no open-loop control). The dynamics is rather determined by the controlled shear stress which for its part influences the shear rate within the system. From a theoretical point of view we based on an approach which was used (in continuum system) to select states

and even suppress chaos in shear-driven nematic liquid crystals [76]. Focusing on a systems with multivalued flow curves (which result from the successive non-equilibrium order transitions) we found that, by tuning the control time scale τ_c as well as the initial conditions, it is possible to select the steady-state configuration of our system. In the present system these configurations are either the state with square in-plane ordering and high viscosity, or the hexagonal state which is characterized by low viscosity. Mathematically, this scheme can be viewed as feedback control with exponentially distributed time-delay [167] (as can be seen by formally integrating Eq. (7.2) and inserting it into Eq. (4.1)). Similar schemes are used to stabilize dynamical patterns in laser networks [168], neural systems [169], and more generally, coupled oscillator systems [170]. The implications of these connections are yet to be explored. Indeed, we expect the method to allow for state selection in any shear-driven system with multivalued flow curve. It therefore seems safe to assume that the capabilities of the present scheme are quite wide. For colloidal layers one may envision, e.g., the stabilization of time-dependent structures such as oscillatory density excitation, which may have profound implications for lubrication properties [171].

Regarding the feedback control most of our results pertain to a colloidal bilayer, however, the fact that we found analogous results for the trilayer suggests that the proposed technique can also be applied for systems with larger number of layers. In fact, we think that the proposed feedback control technique, after some minor adaptations such as consideration of the kinematic (and, possibly, also the non-local) contributions in Eq. (7.1), should also be applicable and fruitful in bulk systems. Moreover, many of other results observed in our study (e.g., translational order transition, zig-zag motion) are in a good agreement with experimental studies which makes us hope that despite disregard of the explicit hydrodynamics, which will be discussed in more detail in Sec. 8.2 the findings discussed in this study can be applied to real colloidal suspensions.

It is also noteworthy that despite an abundance of insights gained in the framework of this study our work also raises many new exciting questions and offers the possibilities for accessing them. Therefore, in the next section we will shortly

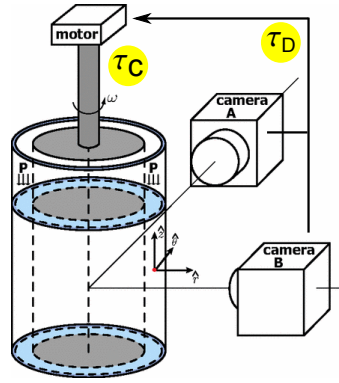


Figure 8.1: Sketch of an experimental setup for an application of the time-delayed feedback control.

discuss a selection of proposals concerning the goals of future research.

Finally, we want to refer to Refs. [66, 172] in which the results presented in Chap. 5 and Chap. 7 were published. The publication containing the findings discussed in Chap. 6 is currently in preparation.

8.2 Outlook

Making proposals for future investigations we want to start with the feedback control method discussed in Chap. 7. In the current study the system dynamics was controlled via the difference between the instantaneously measured shear stress $\sigma_{xz}(t)$ and its imposed value σ_0 . Such an approach enabled us to select the steady state configuration as a function of the control time scale τ_c .

Even though it is very useful to be able to choose the final state of the system one can also imagine applications at which it could be more advantageous to induce oscillations between different structures. An exemplary application where the oscillatory ordering could be of big importance is an optical system in which the reflection or transmission of light is directly coupled to the structure of the contact medium. It is well known that the introduction of time-delayed feedback control can lead to the emergence and stabilization of oscillations within the considered system. Therefore, aiming at inducing oscillations between hexagonal and square

ordered states we suggest to replace the feedback control scheme proposed in Eq. (7.2) by

$$\frac{d}{dt}\dot{\gamma} = \frac{1}{\tau_c} \frac{\sigma_0 - \sigma_{xz}(t - \tau_D)}{\eta_0}. \quad (8.1)$$

In the latter equation the value τ_D describes the time-delay which is necessary to feed the instantaneously measured shear stress back into the system. Experimentally such time-delayed feedback control procedure can be realized via the setup illustrated in Fig. (8.1).

In the scope of our study we performed some preliminary calculations which showed that the method proposed in Eq. (8.1) is able to cause time-delay induced order fluctuations within the system [for details see Sec. B.1].

In addition to that, it could be of interest to investigate the behavior of the system under Pyragas control [173]. The corresponding control function reads

$$\frac{d}{dt}\dot{\gamma} = \frac{1}{\tau_c} \frac{\sigma_{xz}(t) - \sigma_{xz}(t - \tau_D)}{\eta_0}. \quad (8.2)$$

The key feature which makes this method very popular for experimental implementations [174–176] as well as theoretical models [177, 178] is the fact that for its realization no information about the exact structure of the flow curve is needed. The only information which is necessary is the output value of the control parameter at time step t as well as $t - \tau_D$. Moreover, the Pyragas method can be regarded as a “method of time-delay autosynchronization” [179] since the both states placed in relation to each other must be synchronized in order to stabilize the target orbit of the system.

In attempt to access the time-dependent rheological behavior of strongly confined colloidal suspensions the sample can be subjected to oscillatory shear. Similar to the steady shear (Couette flow) small amplitudes of the oscillatory shear were reported to enhance ordering within the sheared material [109]. Moreover, the application of the oscillatory shear can also lead to formation of time-dependent structures [64]. Additionally to the influence on the system structure, the oscillatory shear is also a very useful and common tool if it is necessary to access the

time-dependent rheological properties of the investigated system. Applying oscillatory shear with small strain amplitudes the harmonic stress response is observed. In this regime the stress follows the applied oscillations of the shear field. At larger shear amplitudes, however, the system response becomes increasingly plastic. As a consequence the influence of higher harmonics rises [108].

In our preliminary studies [see Sec. B.2] applying large amplitude oscillatory shear we could observe the plastic response of the considered model system. This behavior strongly resembles the rheology reported in Refs. [180, 181]. Therefore, we hope that more detailed consideration of the oscillatory shear in the framework of our model system can help to deepen the understanding of the rheological properties of strongly confined colloidal suspensions.

Another point of concern is that investigating the dynamics of the bilayer system [see Sec. 5.2] it was found that the functional behavior of the effective shear rate $\dot{\gamma}_{eff}$ as a function of the applied shear rate $\dot{\gamma}$ [see Fig. (5.6)] strongly resembles the results gained in the generalized Frenkel-Kontorova model [92, 154]. In this alternative model the monolayer composed of repulsive interacting particles slides over the hexagonal ordered substrate [92, 154]. The similarity between the dynamics of both models suggests that the proper preparation of our system would also enable us to develop a model which is suited to investigate density excitations, so-called kinks or antikinks [92, 154]. The importance of such density excitations can be explained by the fact that they significantly affect the friction properties of the system.

In our particular case the “proper preparation” implies that instead of one species we have suggested to use a mixture composed of two colloid species. Furthermore, we proposed the introduction of a sort of separation potential U^{sep} .

In the framework of his master thesis Sascha Gerloff pursued the latter idea. In his investigations he could show that the proposed model system indeed leads to an increased mobility due to the development of high density excitations [for more details see Sec. B.3]. His results build a bridge between monolayers sliding over the substrate and strongly confined shear driven mixtures. We hope, that the insights which were motivated by our study and gained by Sascha Gerloff open a

path for future exciting investigations.

Furthermore, investigating colloidal suspensions and evaluating the results gained in numerical studies it is essential to keep in mind that the suspensions are composed not only of large colloids but also of tiny solvent molecules. Although the influence of these particles on colloids, the so-called hydrodynamic interactions, plays a minor role in equilibrium studies it *can* become crucial if non-equilibrium properties of the system are explored. Due to the huge length and time scale differences between microscopic solvent molecules and mesoscopic colloids the proper consideration of the hydrodynamic forces is not trivial. For instance, a colloid with the diameter of $1\mu m$ and the typical Brownian time of $1s$ displaces approximately 10^{10} solvent molecules which explicit simulation must be taken into account with times on the order of $10^{-15}s$ [148]. It is obvious that the computing power available nowadays is not sufficient to cover such large differences between the length- and time scales. Also the exact consideration of the huge number of solvent molecules surpasses the available processing capacity. The only way to incorporate the both particle types in the numerical study is coarse-graining of solvent particles.

The simplest and therefore also very popular method is the simulation of the solvent molecules via the the combination of the random force, mimicking the Brownian motion, and friction acting on colloids as presented in Sec. 2.6. Despite its simplicity this method is widely used in non-equilibrium simulations see e.g., Refs. [34, 64, 108, 109] (also in the current study), since it proved to be able to provide sufficient information about structural and dynamical properties of colloidal suspensions. For example the results concerning shear-driven order transitions and zig-zag motion reported in this thesis [see Chap. 5] are consistent with the findings made in comparable experimental non-equilibrium studies [3, 65].

It should be noted that the overdamped Brownian dynamics method used here neglects the momentum transport via the solvent which is incorporated into the Navier-Stokes equation. This with $1/r$ decaying long range interaction [148] can, however, influence some results more than others. In particular, the rheological properties of the investigated model system and the feedback control strategies reported in Chap. 7 should be confirmed under conditions where the influence of

a solvent is described in a more detailed way. Furthermore, the splitting of the middle layer into sublayers and the existence of lanes, which move at small mutual distances in opposite directions, reported in Chap. 6 can be also strongly affected by hydrodynamics.

One popular method to take into account these interactions was proposed by Ermak and McCammon [182]. They suggested to use an analytical approximation of hydrodynamic interactions via the extension of the “simple” Brownian dynamics by the Oseen tensor [183]. An alternative method to consider the hydrodynamic interaction is *multiple-particle collision dynamics*. The main idea behind this method used for the investigation of the flow behavior of polymers [184] and colloids [185] is to simulate a subset of small fluid particles distributed in subcells and then to calculate the influence of the subcell momenta on large particles.

Appendix A

Theoretical details

A.1 Calculation of the bond angle order parameter

In the current section we are going to clarify how bond angle order can be efficiently calculated numerically. From Eq. (2.66) in Sec. 2.4.3 follows that the bond angle order for one particle can be calculated via

$$\psi_{n,i} = \left| \frac{1}{N_i^b} \sum_{j=1}^{N_i^b} \exp(in\theta_j) \right| \quad (\text{A.1})$$

where the value N_i^b stands for the number of next neighbors of the particle i in the xy -plane. Since we are interested in the absolute value of Eq. (A.1) the latter equation can be rewritten using the following relation

$$\begin{aligned} \sum_{j=1}^{N_i^b} \exp(in\theta_j) &= \sum_{j=1}^{N_i^b} \cos(n\theta_j) + i \sum_{j=1}^{N_i^b} \sin(n\theta_j) \\ &= \Re_{n,i} + i\Im_{n,i}. \end{aligned} \quad (\text{A.2})$$

Here $\Re_{n,i}$ and $\Im_{n,i}$ denote relative and imaginary parts of $\sum_{j=1}^{N_i^b} \exp(in\theta_j)$. Plugging the definition from Eq. (A.2) into Eq. (A.1) we straightforwardly derive

$$\psi_{n,i}^0 = \frac{1}{N_i^b} \sqrt{\Re_{n,i}^2 + \Im_{n,i}^2}. \quad (\text{A.3})$$

Note that since θ_j denotes the bond angle between the arbitrary in-plane axis (in our case x -axis) and the two dimensional (in our case xy -plane) vector \mathbf{r}_{ij} the sine and the cosine of this angle are defined by

$$\cos\theta_j = \frac{\Delta x_{ij}}{\sqrt{\Delta x_{ij}^2 + \Delta y_{ij}^2}}, \quad (\text{A.4})$$

$$\sin\theta_j = \frac{\Delta y_{ij}}{\sqrt{\Delta x_{ij}^2 + \Delta y_{ij}^2}}. \quad (\text{A.5})$$

A.2 Mechanical stability analysis

In Sec. 7.1 it was claimed that the condition $\partial\sigma_{xz}/\partial\dot{\gamma} < 0$ implies a mechanical instability of the system. In this section we perform stability analysis in attempt to verify and clarify the latter statement. For this purpose let us start with Eq. (2.86) which can be rewritten into

$$\sigma_{xz} = \eta(\dot{\gamma})\dot{\gamma}. \quad (\text{A.6})$$

Furthermore, we have to assume that the imposed velocity profile (simple shear flow) $\dot{\gamma}_0 z$ is supplemented by an additional small fluctuation $\epsilon\xi(z, t)$. Consequently the total velocity field is given by

$$u_x(z, t) = \dot{\gamma}_0 z + \epsilon\xi(z, t). \quad (\text{A.7})$$

Then plugging Eq. (A.7) into Navier-Stokes equation which reads

$$\rho \left(\frac{\partial \mathbf{u}}{\partial t} + (\mathbf{u} \cdot \nabla) \mathbf{u} \right) = \nabla \sigma + \mu \Delta \mathbf{u}, \quad (\text{A.8})$$

we can see that the latter reduces to

$$\rho \frac{\partial u_x}{\partial t} = \frac{\partial \sigma_{xz}}{\partial z}. \quad (\text{A.9})$$

Now we insert Eq. (A.6) and Eq. (A.7) into Eq. (A.9). Calculating the Taylor series with the assumption $\epsilon \ll 1$ we yield

$$\rho \frac{\partial \xi(z, t)}{\partial t} = \frac{\partial^2 \xi(z, t)}{\partial z^2} \left(\eta(\dot{\gamma}) + \dot{\gamma} \frac{\partial \eta(\dot{\gamma})}{\partial \dot{\gamma}} \right) \Big|_{\dot{\gamma}_0}. \quad (\text{A.10})$$

Since we consider the dynamics in a strongly confined system, we have introduced appropriate boundary conditions at $z = -L_z/2$ and $z = L_z/2$ with average velocities $u(-L_z/2, t) = -\dot{\gamma}L_z/2$ and $u(L_z/2, t) = \dot{\gamma}L_z/2$, respectively. The function $\xi(z, t)$ which satisfies these boundary conditions is for instance

$$\xi(z, t) = \sum_{m=i}^{\infty} e^{\alpha_m t} \cos \frac{m\pi z}{L_z}, \quad (\text{A.11})$$

Therefore, using Eq. (A.11) we can rewrite Eq. (A.10) in

$$\alpha_m = -\frac{m^2 \pi^2}{\rho L_z^2} \left(\eta(\dot{\gamma}) + \dot{\gamma} \frac{\partial \eta(\dot{\gamma})}{\partial \dot{\gamma}} \right) \Big|_{\dot{\gamma}_0}. \quad (\text{A.12})$$

From Eq. (A.12) follows that the dynamics of the system is unstable whenever the value of the bracket is negative. Thus, the condition for the stability can be defined as

$$\frac{d\sigma}{d\dot{\gamma}} > 0. \quad (\text{A.13})$$

A.3 Stability of the feedback controlled system

In this appendix we investigate the stability of the solutions of Eq. (7.2). Specifically, we consider the impact of small variations of the shear rate from its steady state value $\dot{\gamma}_0$ related to the imposed stress σ_0 . Expanding the right side of Eq.

(7.2) with respect to the difference $\dot{\gamma} - \dot{\gamma}_0$ yields

$$\frac{d}{dt}\dot{\gamma} \approx \frac{\sigma_0 - \sigma_{xz}(\dot{\gamma}_0, t)}{\tau_c \eta_0} - \left. \frac{\partial \sigma_{xz}(\dot{\gamma}, t)}{\partial \dot{\gamma}} \right|_{\dot{\gamma}_0} (\dot{\gamma} - \dot{\gamma}_0) + O(\dot{\gamma}^2). \quad (\text{A.14})$$

For long times we expect the first term on the right side of Eq. (A.14) to vanish, since $\sigma_{xz}(\dot{\gamma}_0, t) \rightarrow \sigma_0$. To linear order, Eq. (A.14) then reduces to

$$\frac{d}{dt}\dot{\gamma} \approx -\frac{1}{\tau_c \eta_0} \left. \frac{\partial \sigma_{xz}(\dot{\gamma}, t)}{\partial \dot{\gamma}} \right|_{\dot{\gamma}_0} (\dot{\gamma} - \dot{\gamma}_0) + O(\dot{\gamma}^2). \quad (\text{A.15})$$

Noting that the values of τ_c and η_0 are both positive, we can follow that the feedback controlled shear rate approaches a steady-state value only if

$$\frac{\partial \sigma_{xz}}{\partial \dot{\gamma}} > 0. \quad (\text{A.16})$$

This corresponds to the usual criterion of mechanical stability [see Sec. A.2] [161].

Appendix B

Preliminary results

B.1 Time-delayed feedback control

Starting from the square ordered configuration and using the parameters of the bilayer system [see Sec. 4.3] we performed some preliminary calculations applying time-delayed feedback control function proposed in Eq. (8.1). One example result is presented in Fig. (B.1). Now comparing the results in Fig. (B.1b) with Fig. (5.3) we can see that the fluctuations observed in the system range from shear rate values which are typical for the square state up to the shear rates at which the layers structure becomes hexagonal. From this it follows that extending Eq. (7.2) by time-delay, as proposed in Eq. (8.1), indeed induces a complex multiparticle behavior which results in fluctuations between different states. Nonetheless at the present stage we only observed fluctuation-like behavior of the shear rate whereby the strict periodicity could not be achieved.

For the future work it can be suggested to perform more detailed scanning of the parameter space in search of the stable periodic orbit.

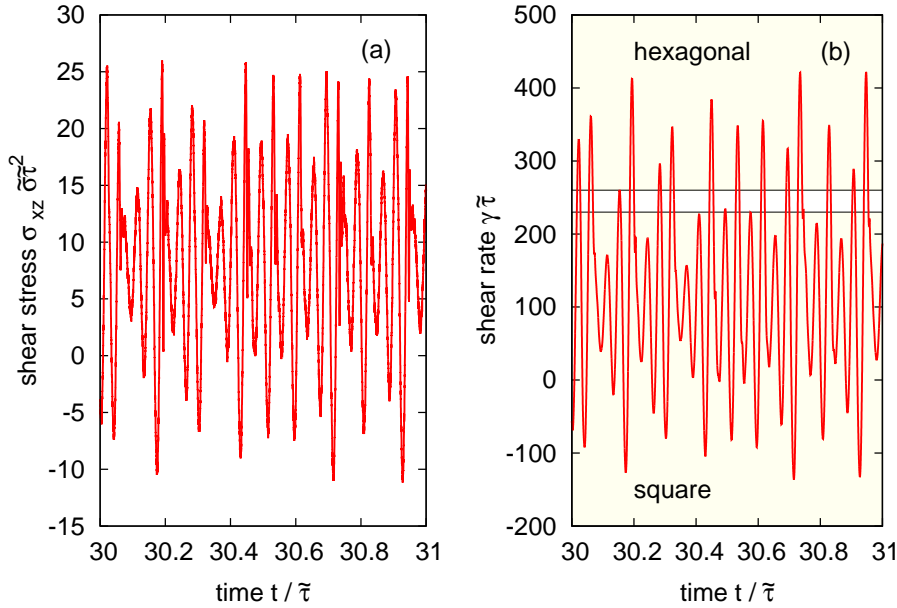


Figure B.1: Fluctuations of the shear stress (a) and the shear rate (b) for the time-delay feedback-controlled colloidal bilayer at $\sigma_0^* = 8$, $\eta_0^* = 0.086$, $\tau_c^* = 0.01$ and $\tau_D^* = 500$. The simulation was started from a square-ordered configuration.

B.2 Oscillatory shear

In the first attempt to access the time-dependent viscoelastic properties of our model system in more detail we replaced the Couette flow in a bilayer system [see Chap. 4] by the oscillatory shear field such that the shear rate was governed by the equation

$$\frac{d}{dt}\dot{\gamma} = \gamma_0 2\pi\nu \cos(t2\pi\nu). \quad (\text{B.1})$$

A selection of the results is presented in Fig. (B.2). In our preliminary results increasing the amplitude of the zero-strain γ_0 we observe the appearance of self-intersection (loops) in the flow curve which is in accordance with other studies performed in other systems under large amplitude oscillatory sheared [180, 181]. These loops correspond to the stress overshoots discussed in Sec. 7.6.

According to the discussion performed in Ref. [108] results similar to those presented in Fig. (B.2) can be used for the characterization of the viscoelastic characteristics of the system. This can be done via the calculation of the storage

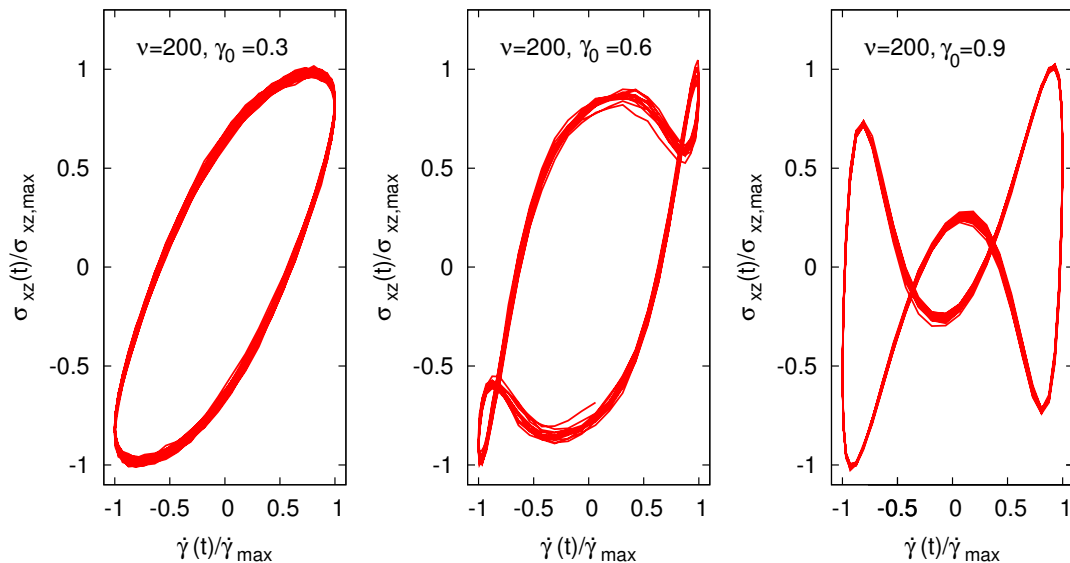


Figure B.2: Lissajous figures illustrating the non-linear character of the stress response at large amplitude oscillatory shear.

and the loss components of the shear modulus [see Eq. (2.90)]. Therefore, we are sure that the preliminary results presented here pave the way for further investigations on the time-dependent rheological properties of strongly confined colloidal suspensions.

B.3 Density excitations

Following experimental studies of strongly confined ludox-silica (colloidal) mixtures [138] Sascha Gerloff has chosen the species such that they had a diameter of $\tilde{\sigma}_1 = 26nm$ and $\tilde{\sigma}_2 = 11nm$ as well as the charge of $Z_1 = 35$ and $Z_2 = 6$ for the first and the second particle type, respectively. A separation potential used in his investigations acts along the confinement direction (z -axis) and reads

$$U_\nu^{sep}(z) \propto \tilde{\sigma}_\nu^3 z. \quad (\text{B.2})$$

The parameter ν denotes the type of the influenced species. The use of this force in combination with two different particle species leads to the situation where the larger particles are stronger pushed towards the lower confining wall. As a result

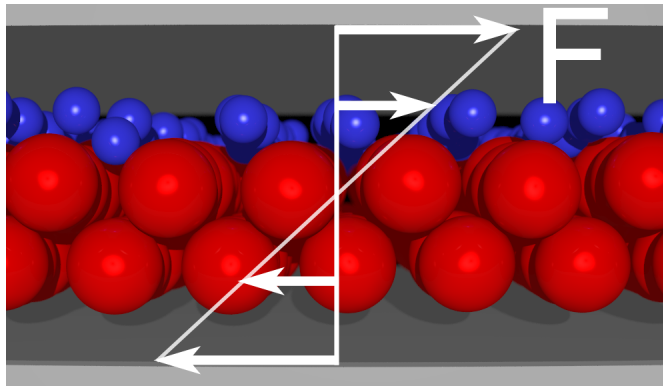


Figure B.3: Sketch of the strongly confined mixture. The model system was used by Sascha Gerloff to investigate the appearance of density excitations. The sketch was provided by Sascha Gerloff.

the layer composed of large particles acts as a substrate whereby the smaller particles correspond to the sliding monolayer.

For a 2:1 mixture a stable long-ranged square order can be achieved. The colloids arrange into three layers [see Fig. (B.3)]. Moreover, the two lower layers, which are composed of larger colloids and mimic a substrate, retain the stability of the square ordered lattice for all considered shear rates.

In his first results Gerloff was able to show that the proposed model system of a strongly confined and sheared mixture displays moving high density excitations (kinks). The findings are comparable to that observed in monolayers driven over the substrate [92, 154]. Furthermore, he observed an increased mobility of the monolayer due to the increase of the number of high density excitations (kinks) [see Fig. (B.4)].

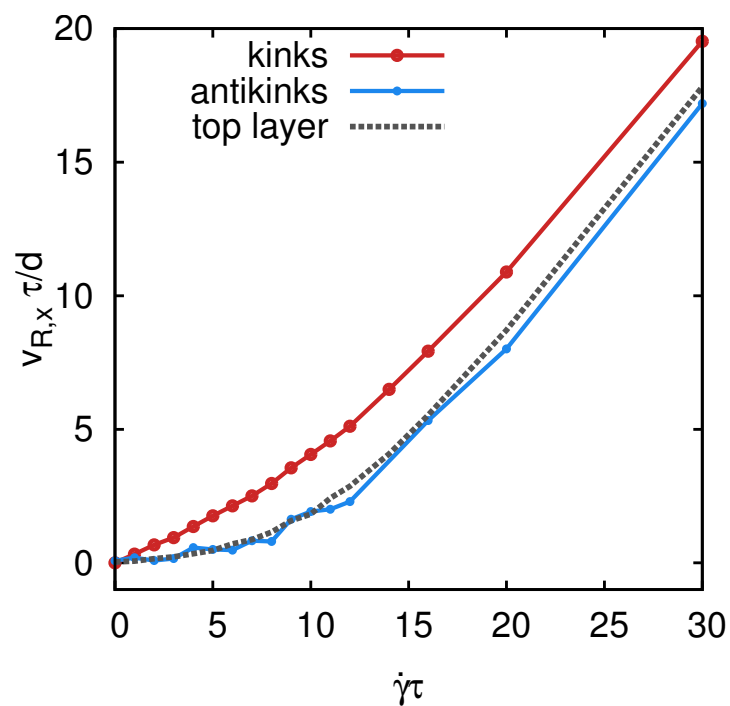


Figure B.4: Velocity of kinks and antikinks compared to the velocity of the center of mass of the reference (upper) layer. The model system was used by Sascha Gerloff to investigate the appearance of density excitations. The graphic was provided by Sascha Gerloff.

Bibliography

- [1] J. D. Martin and Y. T. Hua. Transient and steady-state shear banding in aging soft glassy materials. *Soft Matter*, 8(6940), 2012.
- [2] S. H. L. Klapp, S. Grandner, Y. Zeng, and R. von Klitzing. Charged silica suspensions as model materials for liquids in confined geometries. *Soft Matter*, 6(2330), 2010.
- [3] A. Stipp, R. Biehl, T. Preis, J. Liu, A. B. Fontecha, H. J. Schöpe, and T. Palberg. Heterogeneous nucleation of colloidal melts under the influence of shearing fields. *J. Phys.: Condens. Matter*, 16:S3885, 2004.
- [4] I. W. Hamley. *Introduction to Soft Matter*. Wiley, revised edition, 2007.
- [5] M. Krein. *Herstellung und Anwendung von nanostrukturierten Metalloxiid-Kolloiden*. PhD thesis, Fakultät für Chemie an der Ruhr-Universität Bochum, 2002.
- [6] M. J. Solomon A. S. Almusallam, K. F. Seefeldt, A. Somwangthanaroj, and P. Varadan. Rheology of polypropylene/clay hybrid materials. *Macromolecules*, 34(1864), 2001.
- [7] A. Terray, J. Oakey, and D. W. M. Marr. Microfluidic control using colloidal devices. *Science*, 296(1841), 2002.
- [8] Y. A. Vlasov, N. Yao, and D. J. Norris. Synthesis of photonic crystals optical wavelength from semiconductor quantum dots. *Adv. Mater.*, 11(165), 1999.
- [9] J. A. Lewis. Colloidal processing of ceramics. *J. Am. Ceram. Soc.*, 83(2341), 2000.

-
- [10] D. J. Irvine, A. Stachowiak, and S. Jain. Engineering biomaterials for control of immune cell functions. *Mater. Sci. Forum*, 426(3213), 2005.
- [11] P. C. Hiemenz and R. Rajagopalan. *Principles of Colloid and Surface Chemistry*. Dekker, 3rd edition, 1997.
- [12] A. Blanco, E. Chomski, S. Grabtchak, M. Ibisate, S. John, S. W. Leonard, C. Lopez, F. Meseguer, H. Miguez, J. P. Mondia, G. A. Ozin, O. Toader, and H. M. van Driel. Large-scale synthesis of a silicon photonic crystal with a complete three-dimensional bandgap near 1.5 micrometres. *Nature*, 405(437), 2000.
- [13] M. P. Lettinga, Z. Dogic, H. Wang, and J. Vermant. Flow behavior of colloidal rodlike viruses in the nematic phase. *Langmuir*, 21(8048), 2005.
- [14] R. Jurgons, C. Seliger, A. Hilpert, L. Trahms, S. Odenbach, and C. Alexiou. Drug loaded magnetic nanoparticles for cancer therapy. *J. Phys.: Condens. Matter*, 18(S2893), 2006.
- [15] D. Frenkel and B. Smit. *Understanding Molecular Simulations*. Academic Press, 2nd edition, 2006.
- [16] J. P. Hansen and I. R. McDonald. *Theory of Simple Liquids*. Academic Press, 3rd edition, 2002.
- [17] L. E. Helseth, H. Z. Wen, and T. M. Fischer. Particle diffusion in a field-guided microfluidic channel. *J. Appl. Phys.*, 99(024909), 2006.
- [18] C. T. Kresge, M. E. Leonowicz, W. J. Roth, J. C. Vartuli, and J. S. Beck. Ordered mesoporous molecular sieves synthesized by a liquid-crystal template mechanism. *Nature*, 359(710), 1992.
- [19] W. A. Ducker, T. J. Senden, and R. M. Pashley. Direct measurement of colloidal forces using an atomic force microscope. *Nature*, 353(239), 1991.
- [20] J. N. Israelachvili and R. M. Pashley. Molecular layering of water at surfaces and origin of repulsive hydration forces. *Nature*, 306(249), 1983.

-
- [21] D. T. Wasan and A. D. Nikolov. Spreading of nanofluids on solids. *Nature*, 423(156), 2003.
- [22] M. Kittner and S. H. L. Klapp. Screening effects on structure and diffusion in confined charged colloids. *J. Chem. Phys.*, 126(154902), 2007.
- [23] J. Jordanovic and S. H. L. Klapp. Field-induced layer formation in dipolar nanofilms. *Phys. Rev. Lett.*, 101(038302), 2008.
- [24] I. B. Ivanov and D. S. Dimitrov. *This Liquid Films*. Dekker, 1st edition, 1988.
- [25] J. Gao, W. D. Luedtke, and U. Landman. Origins of solvation forces in confined films. *J. Phys. Chem. B*, 101(4013), 1997.
- [26] P. Pieranski, L. Strzelecki, and B. Pansu. Thin colloidal crystals. *Phys. Rev. Lett.*, 50(12), 1997.
- [27] D. H. Van Winkle and C. A. Murray. Layering transitions in colloidal crystals as observed by diffraction and direct-lattice imaging. *Phys. Rev. A*, 34(562), 1986.
- [28] C. A. Murray, W. O. Sprenger, and R. A. Wenk. Comparison of melting in three and two dimensions: Microscopy of colloidal spheres. *Phys. Rev. B*, 42(688), 1990.
- [29] B. Pansu, Pi. Pieranski, and Pa. Pieranski. Structures of thin layers of hard spheres : high pressure limit. *J. Phys. France*, 45(331), 1984.
- [30] S. Nesper, C. Bechinger, P. Leiderer, and T. Palberg. Finite-size effects on the closest packing of hard spheres. *Phys. Rev. Lett.*, 79(2348), 1997.
- [31] F. Ramiro-Manzano, F. Meseguer, E. Bonet, and I. Rodriguez. Faceting and commensurability in crystal structures of colloidal thin films. *Phys. Rev. Lett.*, 97(028304), 2006.

- [32] S. Heidenreich, S. Hess, and S. H. L. Klapp. Shear-induced dynamic polarization and mesoscopic structure in suspensions of polar nanorods. *Phys. Rev. Lett.*, 102(028301), 2009.
- [33] M. K. Chalam, K. E. Gubbins E. de Miguel, and L. F. Rull. A molecular simulation of a liquid-crystal model. *Mol. Sim.*, 7(357), 1991.
- [34] R. Messina and H. Löwen. Confined colloidal bilayers under shear: Steady state and relaxation back to equilibrium. *Phys. Rev. E*, 73:011405, 2006.
- [35] D. Wilms, P. Virnau, S. Sengupta, and K. Binder. Langevin dynamics simulations of a two-dimensional colloidal crystal under confinement and shear. *Phys. Rev. E*, 85:061406, 2012.
- [36] J. Petravac. Equivalence of nonequilibrium algorithms for simulations of planar couette flow in confined fluids. *J. Chem. Phys.*, 127(204702), 2007.
- [37] L. Ning, X. Meng, and Y. Xie. Effects of lubricant shear thinning on the mixed lubrication of piston skirt-liner system. *Proc IMechE Part C: J Mechanical Engineering Science*, DOI:10.1177/0954406212460610, 2012.
- [38] B. L. Wong, S. H. C. Kim, J. M. Antonacci, C. W. McIlwraith, and R. L. Sah. Cartilage shear dynamics during tibio-femoral articulation: effect of acute joint injury and tribosupplementation on synovial fluid lubrication. *Osteoarthritis and Cartilage*, 18:464, 2010.
- [39] X. Jin, K. H. Yang, and A. I. King. Mechanical properties of bovine pia-arachnoid complex in shear. *Journal of Biomechanics*, 44:467, 2011.
- [40] K. Tan, S. Cheng, L. Juge, and L. E. Bilston. Characterising soft tissues under large amplitude oscillatory shear and combined loading. *Journal of Biomechanics*, 46:1060, 2013.
- [41] S. Nicolle and J. F. Paliarne. On the efficiency of attachment methods of biological soft tissues in shear experiments. *Journal of the Mechanical behaviour of Biomedical Materials*, 14:158, 2012.

- [42] M. J. Mitchell and M. R. King. Fluid shear stress sensitizes cancer cells to receptor-mediated apoptosis via trimeric death receptors. *New Journal of Physics*, 15:015008, 2013.
- [43] L. J. Leslie, L. J. Marshall, A. Devitt, A. Hilton, and G. D. Tansley. Cell exclusion in couette flow: evaluation through flow visualization and mechanical forces. *Artificial Organs*, 37(3):267, 2013.
- [44] D. Helbing. Traffic and related self-driven many-particle systems. *Rev. Mod. Phys.*, 73:4, 2001.
- [45] N. Champagne, R. Vasseur, A. Montourcy, and D. Bartolo. Traffic jams and intermittent flows in microfluidic networks. *Phys. Rev. Lett.*, 105:044502, 2010.
- [46] M. Ripoll, P. Holmqvist, R. G. Winkler, G. Gompper, J. K. G. Dhont, and M. P. Lettinga. Attractive colloidal rods in shear flow. *Phys. Rev. Lett.*, 101:168302, 2008.
- [47] D. Strohober, H. Engel, and S. H. L. Klapp. Oscillatory motion of sheared nanorods beyond the nematic phase. *Phys. Rev. E*, 88:012505, 2013.
- [48] M. Das, B. Chakrabarti, C. Dasgupta, S. Ramaswamy, and A. Sood. Routes to spatiotemporal chaos in the rheology of nematogenic fluids. *Phys. Rev. E*, 71:021707, 2005.
- [49] R. Moorcroft and S. M. Fielding. Criteria for shear banding in time-dependent flows of complex fluids. *Phys. Rev. Lett*, 110:086001, 2013.
- [50] R. Besseling, L. Isa, P. Ballesta, G. Petekidis, M. E. Cates, and W. C. K. Poon. Shear banding and flow-concentration coupling in colloidal glasses. *Phys. Rev. Lett*, 105:268301, 2010.
- [51] R. L. Moorcroft, M. E. Cates, and S. M. Fielding. Age-dependent transient shear banding in soft glasses. *Phys. Rev. Lett*, 106:055502, 2011.
- [52] C.-Y. David Lu, P. D. Olmsted, and R. C. Ball. Effects of nonlocal stress on the determination of shear banding flow. *Phys. Rev. Lett*, 84:642, 2000.

-
- [53] P. T. Callaghan. Rheo nmr and shear banding. *Rheol. Acta*, 47:243, 2008.
- [54] J. K. G. Dhont and W. J. Briels. Gradient and vorticity banding. *Rheol. Acta*, 47:257, 2008.
- [55] S. Manneville. Recent experimental probes of shear banding. *Rheol. Acta*, 47:301, 2008.
- [56] P. D. Olmsted. Perspectives on shear banding in complex fluids. *Rheol. Acta*, 47:283, 2008.
- [57] S. M. Fielding. Complex dynamics of shear banded flows. *Soft Matter*, 3:1262, 2007.
- [58] A. Aradian and M. E. Cates. Instability and spatiotemporal rheochaos in a shear-thickening fluid model. *Europhys. Lett.*, 70:3, 2005.
- [59] A. Aradian and M. E. Cates. Minimal model for chaotic shear banding in shear thickening fluids. *Phys. Rev. E*, 73:041508, 2006.
- [60] D. Lootens, H. Van Damme, and P. Hebraud. Giant stress fluctuations at the jamming transition. *Phys. Rev. Lett.*, 90:178301, 2003.
- [61] J. Zausch and J. Horbach. The build-up and relaxation of stresses in a glass-forming soft-sphere mixture under shear: A computer simulation study. *Europhys. Lett.*, 88:60001, 2009.
- [62] P. Chaudhuri and J. Horbach. Onset of flow in a confined colloidal glass under an imposed shear stress. *Phys. Rev. E*, 88:040301, 2013.
- [63] M. E. Cates and S. M. Fielding. Rheology of giant micelles. *Adv. Phys.*, 55:799, 2006.
- [64] T. H. Besseling, M. Hermes, A. Fortini, M. Dijkstra, A. Imhof, and A. van Blaaderen. Oscillatory shear-induced 3d crystalline order in colloidal hard-sphere fluids. *Soft Matter*, 8:6931, 2012.
- [65] D. Derks, Y. L. Wu, A. v. Blaaderen, and A. Imhof. Dynamics of colloidal crystals in shear flow. *Soft Matter*, 5:1060, 2009.

- [66] T. A. Vezirov and S. H. L. Klapp. Nonequilibrium dynamics of a confined colloidal bilayer in a planar shear flow. *Phys. Rev. E*, 88:052307, 2013.
- [67] J. S. Raynaud, P. Moucheront, J. C. Baudez, F. Bertrand, J. P. Guilbaud, and P. Coussot. Direct determination by nuclear magnetic resonance of the thixotropic and yielding behavior of suspensions. *J. Rheol.*, 46:709, 2002.
- [68] M. E. Cates, S. M. Fielding, D. Marenduzzo, E. Orlandini, and J. M. Yeomans. Shearing active gels close to the isotropic-nematic transition. *Phys. Rev. Lett.*, 101:068102, 2008.
- [69] G. L. Burrell, N. F. Dunlop, and F. Separovic. Non-newtonian viscous shear thinning in ionic liquids. *Soft Matter*, 6:2080, 2010.
- [70] X. Cheng, J. H. McCoy, J. N. Israelachvili, and I. Cohen. Imaging the microscopic structure of shear thinning and thickening colloidal suspensions. *Science*, 333:6047, 2011.
- [71] A. Fall, A. Lemaître, F. Bertrand, D. Bonn, and G. Ovarlez. Shear thickening and migration in granular suspensions. *Phys. Rev. Lett.*, 105:268303, 2010.
- [72] R. Bandyopadhyay and A. K. Sood. Chaotic dynamics in shear-thickening surfactant solutions. *Europhys. Lett.*, 56:447, 2001.
- [73] K. Kang, M. P. Lettinga, and J. K. G. Dhont. Is vorticity-banding due to an elastic instability? *Rheol. Acta*, 47:499, 2008.
- [74] F. Frahsa, A. K. Bhattacharjee, J. Horbach, M. Fuchs, and T. Voigtmann. On the bauschinger effect in supercooled melts under shear: Results from mode coupling theory and molecular dynamics simulations. *J. Chem. Phys.*, 138:12A513, 2013.
- [75] F. Varnik, L. Bocquet, and J. L. Barrat. A study of the static yield stress in a binary lennard-jones glass. *J. Chem. Phys.*, 120:2788, 2004.
- [76] S. H. L. Klapp and S. Hess. Shear-stress-controlled dynamics of nematic complex fluids. *Phys. Rev. E*, 81:051711, 2010.

- [77] Y. T. Hu, P. Boltenhagen, and D. J. Pine. Rheological characterization of microcrystalline cellulose/sodiumcarboxymethyl cellulose hydrogels using a controlled stress rheometer: part i. *J. Rheol.*, 42:1185, 1998.
- [78] V. S. Rudraraju and C. M. Wyandt. Rheological characterization of microcrystalline cellulose/sodiumcarboxymethyl cellulose hydrogels using a controlled stress rheometer: part i. *International Journal of Pharmaceutics*, 292:53, 2005.
- [79] J. D. Joannopoulos, P. R. Villeneuve, and S. Fan. Photonic crystals: putting a new twist on light. *Nature*, 386:143, 1997.
- [80] G. Pan, R. Kesavamoorthy, and S. A. Asher. Optically nonlinear bragg diffracting nanosecond optical switches. *Phys. Rev. Lett.*, 73:3860, 1997.
- [81] J. H. Holtz and S. A. Asher. Polymerized colloidal crystal hydrogel films as intelligent chemical sensing materials. *Nature*, 389:829, 1997.
- [82] S. Pechenov, B. Shenoy, M. X. Yang, S. K. Basu, and A. L. Margolin. Injectable controlled release formulations incorporating protein crystals. *J. Controlled Release*, 96:149, 2004.
- [83] C. Lawrence, M. E. Fabry, and R. L. Nagel. The unique red cell heterogeneity of sc disease: crystal formation, dense reticulocytes, and unusual morphology. *Blood*, 78:2104, 1991.
- [84] C. R. Berland, G. M. Thurston, and M. Kondo. Solid-liquid phase boundaries of lens protein solutions. *Proc. Natl. Acad. Sci. U.S.A.*, 89:1214, 1992.
- [85] A. Ponce, C. Sorensen, and L. Takemoto. Role of short-range protein interactions in lens opacifications. *Mol. Vis*, 12:879, 2006.
- [86] D. Derks. *Colloidal Suspensions in Shear Flow : a Real Space Study*. Doctoral thesis Utrecht University, 2006.
- [87] W. B. Russel, D. A. Saville, and W. R. Schowalter. *Colloidal Dispersions*. Cambridge University Press, 1989.

- [88] A. van Blaaderen. Quantitative real-space analysis of colloidal structures and dynamics with confocal scanning light microscopy. *Prog. Colloid Polym. Sci.*, 104(59), 1997.
- [89] W. K. Kegel and A. van Blaaderen. Direct observation of dynamical heterogeneities in colloidal hard-sphere suspensions. *Science*, 287(290), 2000.
- [90] U. Dassanayake, S. Fraden, and A. van Blaaderen. Structure of electrorheological fluids. *J. Chem. Phys.*, 112(3851), 2000.
- [91] A. Onuki. Phase transitions of fluids in shear flow. *J. Phys.: Condens. Matter*, 9(6119), 1997.
- [92] T. Bohlein, J. Mikhael, and C. Bechinger. Observation of kinks and antikinks in colloidal monolayers driven across ordered surfaces. *Nat. Mater.*, 11:126, 2012.
- [93] U. Siems, C. Kreuter, A. Erbe, N. Schwierz, S. Sengupta, P. Leiderer, and P. Nielaba. Non-monotonic crossover from single-file to regular diffusion in micro-channels. *Sci. Rep.*, 2:1015, 2012.
- [94] K. P. Travis, P. J. Daivis, and D. J. Evans. Computer simulation algorithms for molecules undergoing planar couette flow: A nonequilibrium molecular dynamics study. *J. Chem. Phys.*, 103:3, 1995.
- [95] J. Delhommelle and D. J. Evans. Comparison of thermostatting mechanisms in nvt and npt simulations of decane under shear. *J. Chem. Phys.*, 115:1, 2001.
- [96] K. F. Gauss. über ein neues allgemeines grundgesetz der mechanik. *J. Reine Angew. Math.*, IV:232, 1829.
- [97] D. J. Evans, W. G. Hoover, B. H. Failor, B. Moran, and A. J. C. Ladd. Nonequilibrium molecular dynamics via gauss's principle of least constraint. *Phys. Rev. A.*, 28:2, 1983.

-
- [98] P. J. Daivis and D. J. Evans. Comparison of constant pressure and constant volume nonequilibrium simulations of sheared model decane. *J. Chem. Phys.*, 100:541, 1994.
- [99] J. Delhommelle, J. Petracic, and D. J. Evans. On the effects of assuming flow profiles in nonequilibrium simulations. *J. Chem. Phys.*, 119:21, 2003.
- [100] J. Delhommelle, J. Petracic, and D. J. Evans. Reexamination of string phase and shear thickening in simple fluids. *Phys. Rev. E*, 68:031201, 2003.
- [101] J. Delhommelle, J. Petracic, and D. J. Evans. Non-newtonian behavior in simple fluids. *J. Chem. Phys.*, 120:6117, 2004.
- [102] K. P. Travis and C. Braga. Configurational temperature and pressure molecular dynamics: review of current methodology and applications to the shear flow of a simple fluid. *J. Chem. Phys.*, 104:22, 2006.
- [103] H. H. Rugh. Dynamical approach to temperature. *Phys. Rev. Lett.*, 78:5, 1997.
- [104] O. G. Jepps, G. Ayton, and D. J. Evans. Microscopic expressions for the thermodynamic temperature. *Phys. Rev. E*, 62:4757, 2000.
- [105] J. Delhommelle and D. J. Evans. Configurational temperature profile in confined fluids. i. atomic fluid. *J. Chem. Phys.*, 114:6229, 2001.
- [106] C. Braga and K. P. Travis. A configurational temperature nosé-hoover thermostat. *J. Chem. Phys.*, 123:134101, 2005.
- [107] K. P. Travis and C. Braga. Configurational temperature control for atomic and molecular systems. *J. Chem. Phys.*, 128:014111, 2008.
- [108] J. M. Brader M. Siebenbürger, M. Ballauff, K. Reinheimer, M. Wilhelm, S. J. Frey, F. Weysser, and M. Fuchs. Nonlinear response of dense colloidal suspensions under oscillatory shear: Mode-coupling theory and fourier transform rheology experiments. *Phys. Rev. E*, 82(061401), 2010.

-
- [109] J. J. Cerdá, T. Sintés, C. Holm, C. M. Sorensen, and A. Chakrabarti. Shear effects on crystal nucleation in colloidal suspensions. *Phys. Rev. E*, 78: 031403, 2008.
- [110] P. B. Warren. Electroviscous transport problems via lattice-boltzmann. *Int. J. Mod. Phys. C*, 8(889), 1997.
- [111] P. B. Warren. Dissipative particle dynamics. *Curr. Opin. Colloid Interface Sci.*, 3(620), 1998.
- [112] O. Theissen and G. Gompper. Lattice-boltzmann study of spontaneous emulsification. *Eur. Phys. J. B*, 11(91), 1999.
- [113] E. S. Boek, P. V. Coveney, H. N. W. Lekkerkerker, and P. van der Schoot. Simulating the rheology of dense colloidal suspensions using dissipative particle dynamics. *Phys. Rev. E*, 55(3124), 1997.
- [114] R. Pesché and G. Nägele. Dynamical properties of wall-confined colloids. *Europhys. Lett.*, 51(584), 2000.
- [115] R. Evans. The nature of the liquid-vapour interface and other topics in the statistical mechanics of non-uniform, classical fluids. *Adv. Phys.*, 28:143, 1979.
- [116] U. M. B. Marconi and P. Tarazona. Dynamic density functional theory of fluids. *J Phys: Condens. Matter*, 12:A413, 2000.
- [117] G. Szamel and H. Löwen. Mode-coupling theory of the glass transition in colloidal systems. *Phys. Rev. A*, 44(8215), 1991.
- [118] J. Bławdziewicz and G. Szamel. Structure and rheology of semidilute suspension under shear. *Phys. Rev. E*, 48(4632), 1993.
- [119] A. V. Indrani and S. Ramaswamy. Shear-induced enhancement of self-diffusion in interacting colloidal suspensions. *Phys. Rev. E*, 52(6492), 1995.
- [120] P. Hébraud and F. Lequeux. Mode-coupling theory for the pasty rheology of soft glassy materials. *Phys. Rev. Lett.*, 81(2934), 1998.

-
- [121] A. J. Banchio, G. Nägele, and J. Bergenholtz. Viscoelasticity and generalized stokes-einstein relations of colloidal dispersions. *J. Chem. Phys.*, 111(8721), 1999.
- [122] J. M. Brader, T. Voigtmann, M. E. Cates, and M. Fuchs. Dense colloidal suspensions under time-dependent shear. *Phys. Rev. Lett.*, 98:058301, 2007.
- [123] R. Lahiri and S. Ramaswamy. Shear-induced melting and reentrance: A model. *Phys. Rev. Lett.*, 73(1043), 1994.
- [124] S. Grandner and S. H. L. Klapp. Freezing of charged colloids in slit pores. *J. Chem. Phys.*, 129(244703), 2008.
- [125] S. Grandner, Y. Zeng, R. von Klitzing, and S. H. L. Klapp. Impact of surface charges on the solvation forces in confined colloidal solutions. *J. Chem. Phys.*, 131(154702), 2009.
- [126] S. Grandner and S. H. L. Klapp. Surface-charge-induced freezing of colloidal suspensions. *Europhys. Lett.*, 90(68004), 2010.
- [127] S. H. L. Klapp, S. Grandner, Y. Zeng, and R. von Klitzing. Asymptotic structure of charged colloids between two and three dimensions: the influence of salt. *J. Phys.: Condens. Matter*, 20(494232), 2008.
- [128] M. J. Stevens, M. O. Robbins, and J. F. Belak. Shear melting of colloids: A nonequilibrium phase diagram. *Phys. Rev. Lett.*, 66(23), 1991.
- [129] H.-J. Butt, K. Graf, and M. Kappl. *Physics and Chemistry of Interfaces*. Wiley-VCH, 2 edition, 2006.
- [130] D. L. Chapman. A contribution to the theory of electrocapillarity. *Phil. Mag.*, 25(475), 1913.
- [131] G. Gouy. Constitution of the electric charge at the surface of an electrolyte. *Journ. de Phys.*, 9(457), 1910.
- [132] E. Allahyarov, I. D'Amico, and H. Löwen. Attraction between like-charged macroions by coulomb depletion. *Phys. Rev. Lett.*, 81(1334), 1998.

-
- [133] I. Rouzina and V. A. Bloomfield. Macroion attraction due to electrostatic correlation between screening counterions. 1. mobile surface-adsorbed ions and diffuse ion cloud. *J. Phys. Chem.*, 100(9977), 1996.
- [134] B. I. Shklovskii. Screening of a macroion by multivalent ions: Correlation-induced inversion of charge. *Phys. Rev. E*, 60(5802), 1999.
- [135] S. Grandner. *Structure formation of charged colloidal particles in confined geometry*. PhD thesis, Von der Fakultät II - Mathematik und Naturwissenschaften der Technischen Universität Berlin, 2011.
- [136] P. Debye and E. Hückel. De la théorie des électrolytes. i. abaissement du point de congélation et phénomènes associés. *Physikalische Zeitschrift*, 24(185), 1923.
- [137] H. Löwen, J. P. Hansen, and P. A. Madden. Nonlinear counterion screening in colloidal suspensions. *J. Chem. Phys.*, 98(3275), 1993.
- [138] S. H. L. Klapp, D. Qu, and R. von Klitzing. Long-range interactions between soft colloidal particles in slit-pore geometries. *J. Phys. Chem. B*, 111(1296), 2007.
- [139] Y. Rosenfeld. Free energy model for inhomogeneous fluid mixtures: Yukawa-charged hard spheres, general interactions, and plasmas. *J. Chem. Phys.*, 98(8126), 1993.
- [140] A.-P. Hynninen and M. Dijkstra. Phase diagrams of hard-core repulsive yukawa particles. *Phys. Rev. E*, 68(021407), 2003.
- [141] S. H. L. Klapp, Y. Zeng, D. Qu, and R. von Klitzing. Surviving structure in colloidal suspensions squeezed from 3d to 2d. *Phys. Rev. Lett.*, 100(118303), 2008.
- [142] D. F. Evans and H. Wennerström. *The colloidal domain where physics, chemistry, biology, and technology meet*. Wiley, 2 edition, 1999.

- [143] T. N. Thiele. *Om Anvendelse af mindste Kvadraters Methode i nogle Tilfælde, hvor en Komplikation af visse Slags uensartede tilfældige Fejlkilder giver Fejlene en 'systematisk' Karakter.* Det Kongelige Danske Videnskaberne Selskabs Skrifter - Naturvidenskabelig og Matematisk Afdeling, 1880.
- [144] L. Bachelier. Théorie de la spéculation. *Annales scientifiques de l'École Normale Supérieure*, 17(21), 1900.
- [145] A. Einstein. Über die von der molekularkinetischen theorie der wärme geforderte bewegung von in ruhenden flüssigkeiten suspendierten teilchen. *Annalen der Physik*, 322(8), 1905.
- [146] M. von Smoluchowski. Zur kinetischen theorie der brownschen molekularbewegung und der suspensionen. *Annalen der Physik*, 326(14), 1906.
- [147] J. B. Perrin. Mouvement brownien et réalité moléculaire. *Ann. de Chimie et de Physique (VIII)*, 18(5), 1909.
- [148] J. T. Padding and A. A. Louis. Hydrodynamic interactions and brownian forces in colloidal suspensions: Coarse-graining over time and length scales. *Phys. Rev. E*, 74(031402), 2006.
- [149] K. Dill and S. Bromberg. *Molecular Driving Forces: Statistical Thermodynamics in Biology, Chemistry, Physics, and Nanoscience.* Garland Science, 2 edition, 2010.
- [150] M. P. Allen and D. J. Tildesley. *Computer Simulation Of Liquids.* Oxford University Press, reprint edition, 2006.
- [151] D. L. Ermak. A computer simulation of charged particles in solution. i. technique and equilibrium properties. *J. Chem. Phys*, 62(4189), 1975.
- [152] B. Smit and D. Frenkel. Vapor-liquid equilibria of the two-dimensional lennard-jones fluid(s). *J. Chem. Phys*, 94(5663), 1991.
- [153] J. J. Nicolas, K. E. Gubbins, W. B. Streett, and D. J. Tildesley. Equation of state for the lennard-jones fluid. *Molecular Physics*, 37(5), 1979.

-
- [154] J. Hasnain, S. Jungblut, and C. Dellago. Dynamic phases of colloidal monolayers sliding on commensurate substrates. *Soft Matter*, 9(5867), 2013.
- [155] L. Holzer, J. Bammert, R. Rzehak, and W. Zimmermann. Dynamics of a trapped brownian particle in shear flows. *Phys. Rev. E*, 81(041124), 2010.
- [156] H. Kählert and H. Löwen. Resonant behavior of trapped brownian particles in an oscillatory shear flow. *Phys. Rev. E*, 86(041119), 2012.
- [157] M. Krüger, F. Weysser, and M. Fuchs. Tagged-particle motion in glassy systems under shear: Comparison of mode coupling theory and brownian dynamics simulations. *Eur. Phys. J. E*, 34(88), 2011.
- [158] J. Dzubiella, G. P. Hoffmann, and H. Löwen. Lane formation in colloidal mixtures driven by an external field. *Phys. Rev. E*, 65(021402), 2002.
- [159] J. H. Irving and J. G. Kirkwood. The statistical mechanical theory of transport processes. iv. the equations of hydrodynamics. *J. Chem. Phys.*, 18(817), 1950.
- [160] B. D. Todd, D. J. Evans, and R. J. Daivis. Pressure tensor for inhomogeneous fluids. *Phys. Rev. E*, 52(1627), 1995.
- [161] R. I. Tanner. *Engineering Rheology*. Oxford Engineering Science Series, 2002.
- [162] S. M. Fielding and P. D. Olmsted. Kinetics of the shear banding instability in startup flows. *Phys. Rev. E*, 68(036313), 2003.
- [163] P. Harrowell. Mechanical instability of colloidal crystals under shear flow. *Phys. Rev. A*, 42(3427), 1990.
- [164] J. T. Padding, E. S. Boek, and W. J. Briels. Rheology of wormlike micellar fluids from brownian and molecular dynamics simulations. *J. Phys.: Condens. Matter*, 17(S3347), 2005.
- [165] J. M. Delay and R. G. Larson. *Structure and Rheology of Molten Polymers*. Hanser, 2006.

-
- [166] M. J. Stevens and M. O. Robbins. Simulations of shear-induced melting and ordering. *Phys. Rev. E*, 48(3778), 1993.
- [167] P. Hövel and E. Schöll. Control of unstable steady states by time-delayed feedback methods. *Phys. Rev. E*, 72(046203), 2005.
- [168] T. Jüngling, A. Gjurchinovski, and V. Urumov. Experimental time-delayed feedback control with variable and distributed delays. *Phys. Rev. E*, 86(046213), 2012.
- [169] Y. Song, Y. Han, and Y. Peng. Stability and hopf bifurcation in an unidirectional ring of n neurons with distributed delays. *Neurocomputing*, 121(442), 2013.
- [170] Y. N. Kyrychko, K. B. Blyuss, and E. Schöll. Amplitude death in systems of coupled oscillators with distributed-delay coupling. *Eur. Phys. J. B*, 84(307), 2011.
- [171] A. Vanossi, N. Manini, and E. Tosatti. Static and dynamic friction in sliding colloidal monolayers. *PNAS*, 109(16429), 2012.
- [172] T. A. Vezirov S. Gerloff and S. H. L. Klapp. Manipulating shear-induced non-equilibrium transitions in colloidal films by feedback control. *Soft Matter*, 11:406, 2015.
- [173] K. Pyragas. Continuous control of chaos by self-controlling feedback. *Phys. Lett. A*, 170(421), 1992.
- [174] A. Guderian, A. F. Münster, M. Kraus, and F. W. Schneider. Electrochemical chaos control in a chemical reaction: Experiment and simulation. *J. Phys. Chem. A*, 102(5059), 1998.
- [175] W. Lu, D. Yu, and R. G. Harrison. Instabilities and tracking of travelling wave patterns in a three-level laser. *Int. J. Bifurcation Chaos*, 08(1769), 1998.

- [176] A. Kittel, J. Parisi, K. Pyragas, and R. Richter. Delayed feedback control of chaos in an electronic double-scroll oscillator. *Z. Naturforsch.*, 49A(843), 1994.
- [177] C. Simmendinger and O. Hess. Controlling delay-induced chaotic behavior of a semiconductor laser with optical feedback. *Phys. Rev. A*, 216(97), 1996.
- [178] M. Münkkel, F. Kaiser, and O. Hess. Stabilization of spatiotemporally chaotic semiconductor laser arrays by means of delayed optical feedback. *Phys. Rev. E*, 56(3868), 1997.
- [179] K. Pyragas. Delayed feedback control of chaos. *Phil. Trans. R. Soc. A*, 364(2309), 2006.
- [180] N. Y. C. Lin, S. Goyal, X. Cheng, R. N. Zia, F. A. Escobedo, and I. Cohen. Far-from-equilibrium sheared colloidal liquids: Disentangling relaxation, advection, and shear-induced diffusion. *Phys. Rev E*, 88(062309), 2013.
- [181] R. H. Ewoldt, A. E. Hosoi, and G. H. McKinley. New measures of characterizing nonlinear viscoelasticity in large amplitude oscillatory shear. *J. Rheol.*, 52(1427), 2008.
- [182] D. L. Ermak and J. A. McCammon. Brownian dynamics with hydrodynamic interactions. *J. Chem. Phys.*, 69(1352), 1978.
- [183] J. K. G. Dhont. *An Introduction to Dynamics of Colloids*. Elsevier, 1996.
- [184] M. Ripoll, K. Mussawisade, R. G. Winkler, and G. Gompper. Low-reynolds-number hydrodynamics of complex fluids by multi-particle-collision dynamics. *Europhys. Lett.*, 68(106), 2004.
- [185] C. Prohm, M. Gierlak, and H. Stark. Inertial microfluidics with multi-particle collision dynamics. *Eur. Phys. J. E*, 35(80), 2012.

Danksagung

Wie die Dynamik eines jeden Kolloiden von seinen Nachbarn beeinflusst wird, so wird auch das Leben eines Menschen von seinem Umfeld geprägt. Aus diesem Grund, wenn es darum geht ein ganzes Lebenskapitel abzuschließen, so soll man selbstverständlich nicht vergessen, dass all das was ich erreicht habe von den Menschen ermöglicht wurde, welche mich in dieser Phase meines Lebens begleiteten und geleitet haben. Somit möchte ich die Gelegenheit nutzen allen Menschen zu danken, die während des Studiums und der Doktorarbeit mir zur Seite standen, mich moralisch als auch fachlich unterstützten und letztlich das Schreiben dieser Zeilen ermöglichten.

Ich muss zugeben, dass es mir am Anfang der Promotion nicht klar war, warum die Betreuer dieser Arbeit Doktormutter bzw. Doktorvater genannt werden. Diese Erkenntnis kommt offensichtlich immer im nachhinein.

Mit Prof. Dr. Sabine H. L. Klapp habe ich beruflich all die Phasen durchlebt, welche man mit seinen Eltern erlebt. Anfangs ist alles toll, die Betreuer freuen sich über die kleinsten Erfolge der Doktoranden und loben einen für die trivialen Spielereien. Man genießt den Welpenschutz. Doch irgendwann kommt die berufliche Pubertät, in welcher es zu Spannungen kommt, da die Betreuer von eigenen Schützlingen ein angemessenes Verhalten und entsprechende Leistungen erwarten. Die Doktoranden wiederum sich wundern, warum ihre Betreuer plötzlich viel strenger geworden sind. Als ausgebildeter Akademiker nach der rebellischen Studienzeit wird man nicht so gern bevormundet. Wie ein pubertäres Kind reagiert man (zumindest ich) äußerst empfindlich, fast allergisch, auf jede Kritik. Doch mit der Zeit ebbt die Spannungen ab, der Doktorand lernt zuzuhören, sich professionell (zumindest teilweise) zu benehmen, und erst dann offenbart sich das, was gute Betreuer für ihre Doktoranden während der Promotionszeit getan haben. Man beginnt zu verstehen, dass gute Betreuer, denen das Schicksal des Schützlings nicht gleichgültig ist, nahmen die Konfrontation, wenn nötig, in Kauf, um zu garantieren, dass die Doktoranden am Ende nicht mit leeren Händen dastehen und für das weitere Berufsleben mental gewappnet sind. So wie unsere Eltern uns

in der Pubertät auf das Leben vorbereiten, so bereiten die Doktormutter bzw. der Doktorvater ihre Doktoranden auf das Berufsleben vor. Leider realisieren wir, welche Arbeit und welche Energie in uns reingesteckt wurde, erst dann, wenn die Zeit kommt Abschied zu nehmen.

Wenn man die Parallelen zwischen den Eltern bzw. den Doktoreltern weiter zieht, so kann man sagen, dass das größte Lob für beide ist, wenn ihre Kinder bzw. Schützlinge in ihnen ein Vorbild sehen. Ich bin ein glücklicher Mensch, weil in meinen Augen, sowohl meine Eltern, wie auch meine Doktormutter Prof. Dr. Sabine H. L. Klapp sich bestens für diese Vorbildfunktion eignen. Ich habe Prof. Dr. Sabine H. L. Klapp zu verdanken, dass ich am Ende meiner Arbeit nicht mit leeren Händen dastehe. Doch das ist nicht alles. Sie hat mich für mein zukünftiges Berufsleben vorbereitet, sie hat mir beigebracht, auf die konstruktive Kritik (zumindest etwas) entspannter zu reagieren, professionell zu arbeiten, Projekte zu leiten, Betreuung von Kollegen und somit auch die Verantwortung, nicht nur für sich, sondern auch für andere Menschen, zu übernehmen und vieles, vieles mehr. Ich bin ihr sehr dankbar dafür, dass ich zu keinem Zeitpunkt das Gefühl hatte im Stich gelassen worden zu sein. Meine Betreuerin Prof. Dr. Sabine H. L. Klapp hat die Bezeichnung Doktormutter wirklich verdient. Ich denke, dass so wie man sich bei den Eltern niemals revanchieren kann, so werde ich leider nie die Möglichkeit haben für Prof. Dr. Sabine H. L. Klapp all das zu tun, was sie für mich gemacht hat, doch ich hoffe, dass wenn ich selber irgendwann, irgendwo Chef werden sollte, ihr Erbe an Menschen, welche von mir abhängen werden, weiter zu geben.

Des Weiteren danke ich Dr. Michael A. Zaks dafür, dass er sich bereit erklärt meine Dissertation zu begutachten. Doch das ist natürlich nicht alles. Dr. Michael A. Zaks ist für mich viel mehr als einfach mein Zweitgutachter, er war auch mein Betreuer während meiner Masterarbeit. Zusätzlich zu seiner fachlichen Unterstützung hatte er schon damals wie auch jetzt immer ein offenes Ohr für meine Probleme, Ängste und Sorgen. Er hat es immer geschafft mich zu motivieren. Dr. Michael A. Zaks hat mir vor etwa einem Jahr gesagt, dass ich während der Studienzeit wie ein großes Kind war. Das mag sein. Doch Kinder haben ein großes

Herz und in meinem Herzen nahm und nimmt Dr. Michael A. Zaks einen besonderen Platz ein.

Ich bedanke mich bei Prof. Dr. Michael Lehmann dafür, dass er trotz eines vollen Terminkalenders und vielen Verpflichtungen sich die Zeit genommen hat als Vorsitzender des Promotionsausschusses zu fungieren.

Bei Dr. Ken Lichtner, Alexander Kraft, Rodrigo Lugo Frias, Dr. Christopher Prohm und Sascha Gerloff bedanke ich mich für das Korrekturlesen einiger Kapitel meiner Doktorarbeit und anschließende fachliche Diskussionen.

Ich bedanke mich bei Sascha Gerloff für unsere fruchtbare Zusammenarbeit. Ich bin sicher, dass er eine tolle Zukunft in der Physik haben wird, wobei ich ihm viel Glück wünsche.

Insbesondere möchte ich Robert Gernert erwähnen, welcher mir mit Rat und Tat zur Seite stand, wenn es mal schleppender lief.

Ich freue mich sehr Thomas Heinemann und Helge Neitsch kennengelernt zu haben, mit denen ich von Anfang an auf der gleichen Wellenlänge lag.

Ich bedanke mich auch bei allen anderen Kollegen für die Unterstützung und tolles Arbeitsklima während meiner Zeit in der Arbeitsgruppe.

Obwohl der Betreuer meiner Bachelorarbeit Alexander Kuhlicke das nicht erfährt, so möchte ich mich auch bei ihm für seine tolle Betreuung bedanken.

Ich bin Prof. Dr. Lutz Schimansky-Geier, den ich lieb gewonnen habe, sehr dankbar, dass ich in seiner Gruppe meine Masterarbeit schreiben durfte.

Ich bedanke mich bei Prof. Dr. Dietmar Ebert und Prof. Dr. Helmut Winter, welche mich in den ersten, für mich sehr schwierigen, Semestern immer wieder inspirieren konnten.

Mein Dank gilt auch meinen ehemaligen Kommilitonen Alexander Stark und Christian Weber, welche mich während des Studiums unterstützt und motiviert haben.

Zu guter Letzt möchte ich mich bei meiner Familie bedanken. Ich könnte sehr viel darüber schreiben, was meine Familie für mich bedeutet und wie ich alle lieb habe, doch ich denke egal was ich auch schreibe, so werde ich nie das ausdrücken können, wie wichtig für mich meine Familie ist. Somit will ich nur sagen bzw.

schreiben, dass ohne Sie es nicht nur keine Doktorarbeit oder keinen Doktoranden, sondern schlicht und einfach keinen Tarlan gäbe, was zumindest für mich, sehr traurig gewesen wäre. Ich denke, abgesehen von allen anderen Gründen, das allein ist schon ein ausreichend wichtiger Grund super dankbar zu sein ☺.